Novel Nanocomposites Synthesis and Modelling for Hexavalent Chromium Reduction

Zeyu Kang

Submitted in accordance with the requirements for the degree of

Doctor of Philosophy

The University of Leeds

School of Chemical and Process Engineering

August, 2022

The candidate confirms that the work submitted is his/her own, except where work which has formed part of jointly-authored publications has been included. The contribution of the candidate and the other authors to this work has been explicitly indicated below. The candidate confirms that appropriate credit has been given within the thesis where reference has been made to the work of others.

Parts of this thesis are based on work as follows which has been either published in academic journals or submitted in reviewing:

Kang, Z., Gao, H., Hu, Z., Jia, X., & Wen, D. (2022). Ni–Fe/Reduced Graphene Oxide Nanocomposites for Hexavalent Chromium Reduction in an Aqueous Environment. ACS omega, 7(5), 4041-4051.

Acknowledgements

First and foremost, I would like to extend my deepest gratitude to my supervisor, Prof. Dongsheng Wen, for allowing me to join his research group. For his kindness, encouragement, endless guidance and support in his very busy schedule. Professor Wen does me a lot favour especially when I was in difficulties. His rich experiences and knowledge always inspire me and guide me out of traps from the issues or difficulties. Stepping close to him can always let me feel a kind of positive energy. I cannot have finished this PhD research without his support. The support and mentoring I received from him is something I will never forget in the future life.

I particularly like to express my great thanks to my co-supervisor, Dr Xiaodong Jia. For his support in modelling guidance, paper correction and helpful suggestion in this PhD study. He is highly professional and with great patience. His kindness and patience are always the ones that touch me and motivate me to keep moving.

I also would like to thank Dr Hui Gao. She helped me a lot with essay writing. Under her near hand to hand guidance, I published my work in academic journals. I also cannot forget my colleague, Dr Zhongliang Hu, who help me to become familiar with University of Leeds and many experiment devices. Also, special thanks to all the colleagues staying in the same office with me, Dr Guice Yao, Dr Jin Zhao, Dr Shahid Pervaiz, Mr Xiaolong Ma et. al.

Finally, I would also appreciate my beloved family: my parents and my fiancée. Their ceaseless courage and support throughout my PhD study really give me power and confidence.

Abstract

Chromium (Cr) is a heavy metal pollutant prevalent in freshwater resources. It enters the human circulatory system through drinking water or food chain enrichment and have harmful effects. Existing materials (e.g., bimetallic materials, adsorbent materials, etc.) for Cr (VI) removal lack sufficient adsorption capacity.

In this work, a new Cr (VI) removal material was designed and produced: comprising reduced graphene oxide (RGO) as a support with a high specific surface area, and a combination of Fe and Ni nanoparticles (NPs) as catalytic reducing agents. Such a design permits the composite particle with three integrated functions: adsorption, catalysis, and reduction, with RGO enhancing Cr (VI) adsorption and Fe/Ni NPs enhancing catalytic reducing efficiency. The use of a microchip mixer enhanced the mixing of GO and subsequent decorating of RGO with Fe and Ni NPs. Ni-Fe/RGO exhibited an adsorption capacity of 150.45 mg/g at pH=7 for Cr (VI), which is about 2 times those reported for other materials under similar conditions. The capacity is even higher at lower pH, e.g., 197.43 mg/g at pH 5

Taking into account the cost and reusability of RGO, a ternary system consisting of iron, nickel and multi-walled carbon nanotubes (MWCNTs) were synthesised; Fe and Ni perform the same function as Fe-Ni/RGO. Due to the unusual one-dimensional structure of MWCNTs, the Cr (VI) adsorption capacity is about 20% greater than Fe-Ni/RGO, and the reaction rate is much faster. Fe-Ni/MWCNTs have a degree of reusability, with 91% of adsorption capacity retained for reuse, and MWCNT is an inexpensive material for industrial applications.

The ratio of constituents has a significant impact on its absorption capability. The amount of work required to determine the optimal ratio rises exponentially as additional components are added. Based on the reaction mechanism analysis, a model has been developed in this thesis, and shown to accurately predict the reaction curve and adsorption capacity for various Fe/MWCNTs ratios. This (modelling) approach can significantly reduce the effort for future study and has the potential to be applied to other comparable substances.

Keywords: Environment Remediation; Heavy Metal; Hexavalent chromium; Catalytic reduction; Graphene Oxide; carbo nanotube; kinetics modelling.

Table of Contents

List of Abbreviations

Full name	Short name
Graphene Oxide	GO
Reduced Graphene Oxide	RGO
Chromium	Cr
Hexavalent Chromium	Cr (VI)
Trivalent Chromium	Cr (III)
Zero Valent Iron	Fe (0)
Zero Valent Nickel	Ni (0)
Multi-walled Carbon Nanotubes	MWCNTs
Polyvinyl Pyrrolidone	PVP
1,5-Diphenylcarbazide	DPC
Nano Particles	NPs
Energy-dispersive X-ray spectroscopy	EDS
deionized water	DI water
specific surface area	BET
Scanning Electron Microscope	SEM
Ultraviolet-visible spectroscopy	UV-vis
Fourier Transform Infrared Spectroscopy	FTIR
Transmission Electron Microscope	TEM
Dynamic light scattering	DLS
X-ray photoelectron spectroscopy	XPS
point of zero charge	pHPZC

List of Tables

List of Figures

Chapter 1 Introduction

1.1 Research background: high demand of Cr (VI) removal material

The freshwater supply is a valuable natural resource; it is essential for human life and progress. With the fast rise of industry, waste gas, water, and solid pollution become more severe. When garbage is dumped into the environment, it may compromise water quality, soil quality, and human health [1]. Today, the ecosystem around water resources has been continually degraded. This pollution posed a grave danger to human existence and development. The pollutants include many material kinds with distinct characteristics. For instance, non-biodegradable plastics, heavy metals, and synthetic chemicals [2]. These contaminants will build over time and render water resources unusable if they reach a particular concentration. Heavy metal contamination is one of the leading contributors of pollution [3]. Due to its bioaccumulation and degradability, it has garnered significant interest. Elevated heavy metal concentrations in the environment pose a grave hazard to human health and other forms of life. Therefore, it is vital to remove heavy metals from surface water and wastewater to safeguard human health and the environment [4, 5].

In the subject of environmental contamination, the term heavy metal refers to any metal or metalloid that is visibly hazardous to living creatures, such as mercury, cadmium, lead, chromium, and cobalt [6]. Chromium (Cr) is a typical heavy metal pollutant that is pervasive in the environment due to its broad

usage in metallurgical, chemical, refractory, and cast iron processes [7]. The predominant stable forms of chromium in the environment are trivalent chromium (Cr (III)) and hexavalent chromium (Cr (VI)). Cr (III) is a necessary element for the human body, and its toxicity is moderate [8]. The toxicity of Cr (VI) is about one hundred times that of Cr (III) [9], posing far greater environmental and health hazards. It can enter the human circulatory system through drinking water or food chain enrichment and have harmful effects on people [10].

1.2 Motivation

The previous section has shown the great danger to humans of Cr (VI) in the water environment. The removal of Cr (VI) from the aquatic environment is a matter of great urgency. In recent years, many researchers have developed various materials for the removal of Cr (VI) and some progress has been made. However, Cr (VI) contamination has not been eliminated and still poses a serious threat to human health [11]. This is due to the fact that current materials have a number of disadvantages:

1. Low Cr (VI) removal capacity, resulting in the inability to reduce Cr (VI) concentrations in water to below safety standards.

2. High production or application costs for some materials, e.g. requiring inert gas protection for synthesis, not reusable, etc.

3. Some materials rely solely on physical adsorption or electrostatic action to remove Cr (VI), without reducing it to the less toxic Cr (III). There is a risk that the adsorbed Cr (VI) will be re-released into the environment and cause secondary contamination.

4. The research effort is high, especially when searching for the best material ratio.

The project aims to develop materials with high Cr (VI) removal capacity, at low cost, to avoid potential secondary contamination, and to develop a model that can predict the Cr (VI) removal capacity of new materials to reduce workload.

1.3 Aim and objectives

This thesis aims to develop novel nano-composites that can efficiently reduce hexavalent chromium for environmental remediation, and to develop predictive models for further optimisation. Project objectives are:

1. Design and synthesis a novel three-in-one using iron nanoparticles, nickel and reduced graphene oxide. The material shall overcome the disadvantages of previous bimetallic materials such as difficult collection, low removal capacity of adsorbent-loaded monometallic materials, and exhibit great Cr (VI) adsorption capacity.

2. Achieve further increase in Cr (VI) adsorption capacity by analysing the adsorption principles of the triad of iron nanoparticles, nickel and reduced graphene oxide materials, to develop low-cost multi-walled carbon nanotube-based composites, by replacing reduced graphene oxide.

3. Develop a model by analysing the chromium adsorption process, to predict the Cr (VI) adsorption capacity and adsorption profile of the Fe - multi-walled carbon nanotube binary system, with appropriate experimental validation, which could significantly reduce the effort required to find the optimal components in the synthesis of the target material.

1.4 Thesis layout

The thesis is structured in 7 Chapters.

In Chapter 1, the current status of Cr (VI) pollution is introduced. Meanwhile, the motivation and objectives of this study is stated.

In Chapter 2, existing methods for Cr (VI) removal are described and a range of new materials for Cr (VI) removal that have recently been developed are analysed. Current research advances in modelling for the removal of Cr (VI) are analysed.

The three main components of the thesis are presented in Chapter 4-6. In Chapter 4, the combination of iron and nickel nano bimetals with reduced graphene oxide to form a new three-in-one material. The mixing process was continued using microchip mixing technology in comparison to conventional stirred mixing. The new three-in-one material achieved over 50% Cr (VI) removal capacity improvement compared to literature reports.

In Chapter 5, a triple combination of iron nanoparticles, nickel bimetals and multi-walled carbon nanotubes was synthesised to achieve reusability and 20 percent higher Cr (VI) removal capacity of the material compared to the material in Chapter 4.

In Chapter 6, a model that can predict the Cr (VI) removal capacity and curve of carbon nanotube-loaded iron nanomaterials was developed and validated experimentally.

Conclusion and future work are presented in Chapter 7.

Chapter 2 Literature review

2.1 Cr (VI) reduction methods

To solve the above mentioned problem, a lot of advanced treatment technologies have been applied for efficiently Cr (VI) adsorption, such as chemical precipitation [12], ion exchange [13], adsorption, membrane filtration, and electrochemical treatment [14]. Every single method to remove heavy metal have its advantages and disadvantages. Combining serval reduction methods is an excellent way to increase removal efficiency. The two most widely used methods are introduced below:

2.1.1 Chemical precipitation

Because of its simple process and inexpensive capital cost, the chemical precipitation method is a method that uses chemical reaction to convert a dissolved heavy metal in waste water into a water-insoluble heavy metal compound. Chemical precipitation is the most widely used process in the industry [15]. However, chemical precipitation is usually adapted to treat high concentration wastewater containing heavy metal ions, and it is ineffective when the metal ion concentration is low. Moreover, chemical precipitation is not economical and can produce a large amount of sludge to be treated with great difficulties [16]. Chemical precipitation is distinguished by the type of precipitate. It consists mainly of hydroxide precipitation method and sulphide precipitation method.

Hydroxide precipitation

Hydroxide precipitation is a method of adding sulphides such as sodium sulphide or hydrogen sulphide to waste water. The reaction between heavy metal ions and sulphur ions produces insoluble metal sulphide precipitates. It is the most widely used chemical precipitation technique due to its relative simplicity, low cost and ease of pH control [17]. The hydroxide precipitation process was evaluated using $Ca(OH)_2$ and NaOH to remove Cr (VI) ions from wastewater [18].

Sulphide precipitation

Sulphide precipitation is a method of adding sulphides such as sodium sulphide or hydrogen sulphide to waste water. The reaction of heavy metal ions between sulphur ions to produce insoluble metal sulphide precipitates. Compared to hydroxide precipitation, the solubilities of the metal sulphide precipitates are dramatically lower than hydroxide precipitates, and sulphide precipitates are not amphoteric. Hence, the sulphide precipitation process can achieve a higher metal removal over a broad pH range [16].

2.1.2 Adsorption

Adsorption is a method of physical and chemical adsorption of Cr(VI) in water by means of porous solid adsorbents with special functional groups and large specific surface area. The commonly used adsorbents are activated carbon, zeolite, bentonite, humic substances, etc. According to the adsorption mechanism, adsorption is generally classified into two types: physical adsorption and chemical adsorption.

For physical adsorption, adsorption between the adsorbent and the adsorbate is through the intermolecular attraction, which is called the van der Waals force [19].

Chemical adsorption refers to the chemical reaction between adsorbent and adsorbed substances [19]. It needs a certain amount of activation energy to form a chemical bond to cause adsorption. The affinity of the formed chemical bond can vary difference, but it is significantly more potent than the van der Waals force of physical adsorption.

The commonly used adsorbent types are activated carbon [20], multi-walled carbon nanotubes [21], inorganic materials [22], and resins [23]. At present, there are already some applications to practical industrial production. More details about the applications of adsorbent materials is presented in 2.2.

2.1.3 Ion exchange

The core of the ion exchange method is an ion exchanger. Free-moving ions in an ion exchanger are exchanged with heavy metal ions in solution. Commonly used ion exchangers are insoluble polymer compounds such as dextran, resins and cellulose, all of which contain groups that can be dissociated in water and which can exchange with contaminant ions in aqueous solutions. Anion exchange resins can exchange with chromate or dichromate in water, thus effectively removing Cr(VI) from water; Ion exchange has high treatment capacity, high removal efficiency and fast kinetics [13]. The removal of heavy metal ions by ion exchange resins is influenced by certain variables such as pH, temperature, initial metal concentration and contact time [24]. The driving force for ion exchange is the difference in concentration between the ions and the affinity of the functional

groups on the ion exchanger. In most cases, ions are adsorbed before they are exchanged and have an adsorptive exchange effect. However, ion exchange resins must be regenerated with chemicals after use, and regeneration can cause serious secondary contamination. It is also expensive and cannot be used on a large scale, especially when treating large quantities of wastewater containing low concentrations of heavy metals.

2.1.4 Electrochemical treatment

Electrochemical treatment is mainly under the action of an external electric field, by controlling the voltage or current through the electrons and ions in the wastewater to remove the pollutants.

The principle of electrochemical chromium removal is mainly electrolytic reduction and precipitation. Cr (VI) containing water into the electrolytic tank with iron as the anode for electrolysis, under the action of direct current iron loss of electrons in the anode area to generate Fe^{2+}, Cr (VI) and Fe^{2+} reaction to generate Cr^{3+} and Fe^{3+}; at the same time the cathode area water electrolysis to generate OH^- and H_2, Cr^{3+} and Fe^{3+} and OH- reaction to generate $Fe(OH)_3$ and $Cr(OH)_3$ precipitation, the Cr (III) and Cr (VI) are removed simultaneously.

The method will not produce secondary pollution. Compared with other traditional treatment methods, electrochemical methods are used in industrial waste because of their good treatment effect, low operating cost, low sludge generation, high degree of automation, ease of operation and management, and the ability to remove multiple pollutants at the same time. However, electrochemical technologies involving high initial capital investment and the expensive electricity supply Meanwhile, electrochemical treatment often

requires the addition of a large amount of salts as electrolytes to increase the conductivity, resulting in high salt content in the treated water, which cannot be directly recycled. These disadvantages restricted its development.

2.1.5 Membrane filtration

Membrane separation takes advantage of the differences in the properties of different components in a given environment. Membranes are porous layers that allow a certain type of fluid to flow through them but can confine specific contaminants or particles based on their physicochemical properties and molecular sites. A driving force such as a certain pressure difference, concentration difference or potential difference is applied to both sides of the membrane to allow Cr (III) and Cr (VI) to selectively pass through the membrane, thus achieving removal from the water.

Membrane filtration processes offer higher removal efficiency, no contamination load and simple separation methods compared to conventional techniques [25].

Yao et. al.[26] prepared magnetite films based on the oxidation of 316L stainless steel and achieved 100% chromium removal at pH = 4.

However, in practice, it is easily contaminated by other materials in the environment, has poor mechanical stability, high investment and poor selectivity, and is generally not used for the treatment of large quantities of wastewater, but mainly for the recovery of substances with high added value[27].

2.2 Cr (VI) reduction material

Although a large number of methods have been applied for the removal of Cr (VI), methods such as electrochemical treatment, membrane filtration, ion exchange etc. have too many limitations. Currently the most widely used methods are chemical reduction and adsorption. Several types of materials that have been widely investigated for chemical reduction and adsorption are presented below.

2.2.1 Micro and nano iron particles

Iron is the most abundant transition metal and the fourth most abundant element in the earth's crust [28]. The valence electron layer structure of Fe is 3d6 4s2, and the standard electrode potential of Fe^{2+}/Fe ($\varphi 0\ Fe^{2+}/Fe = -0.440V$) is negative at 298.15K and 101.325KPa [29]. Therefore, the Fe (0) reaction activity is intense. As an electronic donor, Electrons on its surface are passed through electron transfer to metal ions with a standard electrode potential higher than -0.440 V [30]. Hence zero-valent iron (ZVI) has been proposed as a chemical precipitation agent to remove chromium contaminants [31-34]. For example, Cr (VI) could be reduced by ZVI and form insoluble precipitates $Cr(OH)_3$ with much lower toxicity in a neutral or alkaline environment. Notably, ZVI is non-toxic, inexpensive and easy to produce, which is good for large-scale applications in industry. Hence different types of ZVI materials have been used for the removal of chromium contaminants, including conventional micrometre-sized ZVI and nanometre-sized zero-valent iron.

For evaluation of the chromium removal ability of different ZVI materials, Cr (VI) adsorption capacity (mg/g) is used to assess their performance. Previous

studies demonstrated that the environmental pH matters the ZVI's adsorption capacity of Cr (VI) [35-37]. Because the primary Cr (VI) species in water are $Cr_2O_7^2$ and $HCrO_4^-$ at low pH and CrO_4^{2-} at high pH [38], respectively. The electrostatic force and competition between OH^- and precipitation agents will lend to lower Cr (VI) adsorption capacity at higher pH [39]. Hence, pH value must be considered when comparing Cr (VI) adsorption capacity. Conventional micrometre-sized ZVI presents the ability of Cr (VI) removal, but a relatively low adsorption capacity limits its application [40].

Nano zero-valent iron particles have a smaller particle size and a larger specific surface area than ordinary iron powders. If the specific surface area of ordinary iron powder with a particle size of less than 10μm is only $0.9m^2/g$ [41], for Nano zero-valent iron, it is from 10 to 450 m2/g [42]. Therefore, with a much higher specific surface area, nanometre-sized zero-valent iron shows a better Cr (VI) removal potential [35-37]. Nahuel *et al.*[43] used bare iron nanoparticles to remove Cr (VI) and obtained an adsorption capacity of 47.2 ± 0.1 mg/g at pH =5 and 411 ± 24 mg/g at pH=3, respectively. The adsorption capacity of 60.03 mg/g at pH=6.8 was found by Chen *et al.*[44] and 10.06 mg/g at pH=6.36 by Ali *et al.*[45].

These studies demonstrated iron nanoparticles has great potential as a Cr removal agent; however, iron nanoparticles do not work well in practical applications, mainly the main reasons for this are as follows:

Ageing: nZVI is extremely reactive and therefore the structure and chemical properties of nZVI change over time during preparation, storage and application [46].

Lack of directionality: iron nanoparticles is a strong reducing agent with poor electron selectivity. iron nanoparticles is able to react not only with the target pollutant, but also with other aqueous components (e.g. nitrate and organic matter), depleting its reducing properties and reducing its reaction with the target pollutant [47].

agglomeration: the agglomeration between nZVI particles is exacerbated by the high surface energy and strong magnetic effects, causing nZVI particles to attract each other and aggregate into larger particles, reducing their mobility in water and their effective surface area [48].

These reasons will decrease the adsorption capacity and may produce secondary pollution [49]. Besides, the separation of iron nanoparticles from the treated solution also presents a big challenge. In order to overcome these disadvantages, over the years researchers have tried to modify iron nanoparticles using a variety of different methods [50]. The current modification methods for iron nanoparticles are mainly bimetallic [51], surfactant modification [52], and sorbent support [53] methods.

2.2.2 Bimetallic nanoparticles

To counteract the agglomeration effect of pure iron and to increase the adsorption quantity and rate, iron-based bimetallic compounds have been studied. Bimetallic particles were first used with micro-scale iron [54]. Normally, bimetallic particles are constituted with a corrosive metal such as iron or zinc along with a noble metal such as palladium (Pd) [55], copper (Cu) [56], nickel (Ni) [57] or cerium (Ce) [58]. The iron in bimetallic nanoparticles acts as the reductant to generate hydrogen from water, while the second metal acts as a catalyst [59]. As reported, the reaction rates of iron nanoparticles particles

enhanced with Pd (FePd) and Ni (FeNi) are much higher than those of monometallic nZVI [60, 61]. For example, the reaction rate of FeNi particles is almost two orders of magnitude higher than monometallic nZVI for the degradation of trichloroethylene [62]. Similar results are obtained for FePd nanoparticles [63].

Especially for Cr (VI) removal, Chen et al [64] composited Fe-Ce bimetal oxide and obtained a maximum adsorption capacity of 75.36 mg/g at pH=4. Wen et al.[65] reported a Fe-Ce bimetal oxide with an adsorption capacity of 125.28 mg/g at pH=3. Fe-Ni bimetal synthesized in an ultrasound-assisted system was proposed by Zhou et al.[66], this system enhanced the dispersion of bimetals and demonstrated an adsorption capacity of 67.6 mg/g at pH=5. Such bimetal material systems show better effects than the pure iron nanoparticles system at similar pH conditions [67].

Despite bimetal material having significant advantages compared to the pure iron nanoparticles system, there are some limitations to bimetal materials [61, 68]. (I) It trends to aggregate as powdered material, which hugely affects the adsorption capacity. (II) The bimetal metal material can only reduce heavy metal to a lower valence state, such as Cr (VI) to Cr (III). The Cr (III) is not immobilized, and it can continue to diffuse in the environment to generate secondary pollution. (III) The nanoparticles are hard to collect back in practical application, which will increase the operating costs.

2.2.3 Sorbent-supported materials

Although iron-based bimetallic particles substantially mitigate the disadvantage of pure iron agglomeration and increase the adsorption capacity to some degree, they do not completely eliminate it. However, it is difficult to

recycle and reuse nanoparticles, and the trivalent chromium formed by their reduction is also difficult to recover, and there is a risk of reversion to hexavalent chromium. A number of materials based on adsorbents have been researched in order to overcome the recycling issue.

Materials having a high specific surface area and a porous structure are excellent adsorbent candidates. Including clay minerals, bio sorbent materials and carbon-based compounds (graphene, carbon nanotubes).

On the adsorbent, some researchers added nanoparticles of iron. The sorbent-supported materials combine the functions of iron nanoparticles reduction and adsorption enhancement by sorbents. A variety of adsorbent materials were used to support iron nanoparticles and were thoroughly explored.

Clay minerals

Clay mineral is largely available in the environment, and it is also very cheap material. Typically, a natural mineral consists of silica, alumina, and water [69]. As an adsorbent, clay mineral has non-hazardous, high specific surface area, moreover, it contains interchangeable cations and anions [70]. Clay mineral has gain high interests from researchers.

Zhao *et al.*[71] natural akadama clay for Cr (VI) removal from aqueous solution at pH=2 and got an adsorption capacity of 4.29 mg/g. Most natural clays have a low capacity for Cr (VI) adsorption and need to be modified to increase their capacity. David *et al.*[72] use hexadecyltrimethylammonium bromide to modify the bentonite and test adsorption capacity at pH=3, got results for 10.04 mg/g.

The limited specific surface area of some of the natural clay materials limits the further increase in Cr (VI) adsorption capacity. and Wang *et al.*[73] chose natural halloysite nanotubes, a silica-aluminate clay with a hollow nanotube structure, which has a higher specific surface area. It has also been modified by hexadecyltrimethylammonium bromide and got adsorption capacity of 17.6 mg/g at pH=3.

Pure clays minerals and modified clays have enough absorption surface points for Cr (VI) immobilization. However, the Cr is still in Cr (VI) and can be released back to environment. To solve the problem, some researchers loaded iron nanoparticles on its surface act as reductant. Li *et al.*[74] synthesized bentonite-supported iron nanoparticles and obtained an adsorption capacity of 7.3 mg/g at pH=6. Fu *et al.* [75] prepared sepiolite supported iron nanoparticles and got a better adsorption capacity of 43.86 mg/g at pH=6. Lu et al.[76] combined bimetal and sorbent-supported material together, by using Fe-Ni bimetal decorated on montmorillonite, obtained the adsorption capacity about 65 mg/g at pH=3. About 50 precents better than the results obtained with monometallic iron loading on clay materials

After iron nanoparticles added, the adsorption capacity got enhanced but it is still can be increased by change higher specific surface area adsorbent, such as bio sorbent materials, RGO and MWCNTs.

Bio sorbent materials

The majority of bio sorbent materials are sourced from agricultural and forestry raw materials. With low cost, little environmental pollution, due to its relative high surface area, and surface reactivity, it has been investigated by researchers [77].

The researchers first used unprocessed bio sorbent material for Cr (VI) removal experiments. Uysal and Ar [78] prepared adsorbent based on pine sawdust and got adsorption capacity of 30.48 mg/g without pH control, the Cr (VI) is . Altun et al.[79] tested rye husk and got adsorption capacity for 22.62 mg/g at pH=3. Gao et al.[80] collected particles between 150 and 380 um from air-dried rice straw and obtained an adsorption capacity of 3.15 mg/g at pH=2. Gonzalez et al.[81] tested grinded coconut husks at pH=2 and got adsorption capacity for 6.3 mg/g.

Unprocessed bio sorbent materials are unable to reach higher Cr (VI) adsorption capabilities due to restrictions such as their specific surface area and charge. Researchers have attempted to improve the performance of bio sorbent materials by modifying or processing them.

Activated carbon is also a kind of bio sorbent material, it has abundant microporous structure, it is normally produced from organic raw material and in a powder or particle form [82]. Khezami et al.[82] tested activated carbons produced from wood, demonstrated an adsorption capacity of 95.1 mg/g at pH=6. Wang et al.[83] researched on activated carbon prepared from coconut shell, obtained an adsorption capacity of 45.2 mg/g at pH=3.5. These results are significantly better than unprocessed bio sorbent materials.

Biomass sorbent materials remove Cr (VI) primarily by electrostatic attraction and physical surface adsorption. The mechanism restricts the higher adsorption capacity that may be reached, and the adsorbed Cr remains in the Cr (VI) form, with the possibility of re-entering the environment. In order to overcome these concerns, researchers loaded iron nanoparticles on bio sorbent materials as reductant.

Qian et al.[84] composited carboxymethyl cellulose supported iron nanoparticles and demonstrated its adsorption capacity of 33 mg/g at pH=5.5. Sharma et al.[85] studied cellulose supported iron nanoparticles at pH=3, showing an adsorption capacity of 106.4 mg/g.

The adsorption capacity improved once iron nanoparticles was introduced as a reductant, although it is still insufficient. This is because the specific surface area of bio sorbent materials is lower than that of artificial synthetic materials: such as RGO and MWCNTs. In the meanwhile, it is impossible to eliminate all impurities from bio sorbent materials, which has a negative impact on their adsorption ability.

Carbon-based compounds

By far the most widely used carbon-based nanomaterials for heavy metal removal are graphene and carbon nanotube-related materials

Reduced graphene oxide (RGO) is a recently developed adsorbent with a two-dimensional single atomic layer structure, which possesses an exceptionally high specific surface area [86].

It has been reported that higher Cr (VI) adsorption capacity can be obtained when using graphene related material as a base supporting material, such as RGO and graphene oxide (GO). Humera et al.[87] synthesized graphene-iron nanoparticles and got an adsorption capacity of 162 mg/g at pH=4.25. Jie et al.[88] found that graphene-iron nanoparticles's adsorption capacity can reach 180.16 mg/g at pH=5. Li et al.[89] confirmed an adsorption capacity of 21.72 mg/g at pH=7 for graphene supported iron nanoparticles. Lv et al.[90] decorated iron nanoparticles on magnetic Fe_3O_4/graphene and observed an adsorption capacity of 66.22 mg/g at pH=8. Wang et al.[91] loaded Fe_3O_4 on

PEI modified GO and obtained its adsorption capacity can change from around 250 to 50 mg/g when tuning pH from 2 to 7.

Carbon nano tubes (CNTs) and multi-walled carbon nanotubes (MWCNTs) are recently developed adsorbents with a one-dimensional tube structure, they have attracted much attention because of their exceptionally high specific surface area and strength [92]. Numerous different materials based on MWCNTs are synthesized and tested for Cr (VI) adsorption capacity.

Carbon nanotubes without treatment have a relatively low Cr (VI) adsorption capacity. Ali Atieh et al.[93] found carbon nanotubes supported by activated carbon and got an adsorption capacity of 9.0 mg/g at pH=2.

Researchers intend to boost the Cr (VI) adsorption capacity of carbon nanotubes by modification.

Some researchers modified carbon nanotubes with organic solvent. Kumar et al.[94] modified MWCNTs by tetra n-heptyl ammonium bromide and obtained 85.83 mg/g adsorption capacity at pH=2.8. Sun et al.[95] immobilized HSO_4 on MWCNTs-COOH and obtain 31.29 mg/g adsorption capacity at pH=2.0. This organic solvent modified carbon nanotubes removal Cr (VI) by electrostatic attraction, physical sorption, surface complexation. They lack reducibility to reduce Cr (VI) to Cr (III). The constant presence of Cr in the form of Cr (VI) and the possibility of its re-release into the environment is a major concern.

In order to reduce Cr (VI) to Cr (III), reducing metals, such as iron, are introduced into the system. Lee et al.[96] synthesized Magnetic iron oxide MWCNTs and got adsorption capacity of 12.61 mg/g at pH= 3.0. Ma et. al.et al.[97] decorated $FeMnO_x$ on MWCNTs and observed an adsorption capacity

of 47.25 mg/g at pH=2.0. Verdugo et al.[98] synthesized α- Fe2O3/MWCNTs and confirmed adsorption capacity for 75mg/g at pH=6.0. Murali et al.[99] synthesized ZnO-Functionalized MWCNTs and the adsorption capacity reach upto140 mg/g at pH=2.

As artificial synthetic materials, RGO and MWCNTs has much higher degree of purity than clay minerals and bio sorbent materials. This facilitates the achievement of higher adsorption capacities. At the same time, ROGs and MWCNTs have several times the specific surface area of clay minerals and bio sorbent materials, can provide more adsorption sites. The reported literatures also show that materials based on ROGs and MWCNTs have a higher adsorption capacity than other materials under similar conditions. Although relatively high adsorption capacities have been obtained for iron nanoparticles loaded with RGO and MWCNTs. The analysis of the reduction mechanism and atomic conversion of Cr (VI) shows that there is still a large amount of iron not involved in the reaction and there is still room for improvement in the adsorption capacity. Considering the improved adsorption capacity of bimetallic particles compared to iron nanoparticles, replacing the loaded iron nanoparticles with bimetallic particles could be one of the ways to solve this problem.

2.3 Simulation for Cr (VI) adsorption

Most of the Cr (VI) adsorption research is based on experiments. Researchers fit their experiment data with either Langmuir and Freundlich isotherms or Pseudo-First-Order and Pseudo-Second-Order equation. These fits can only be used to help researchers analyse the mechanism of Cr (VI) removal.; they

cannot be used to anticipate experimental outcomes or minimise workload through simulation. Until now, only a few researchers made simulation for predicting Cr (VI) adsorption capacity.

Mosai et al.[100] used PHREEQC (which stands for, pH, redox, equilibrium written in the C language) geochemical modelling code coupled to parameter estimation. Meanwhile used the observed results of pH (2–9) on the adsorption of heavy metal onto generalized weak, medium and strong sites of the agricultural soil to calibrate the model. They successfully predicted the adsorption capacity of natural and man-made adsorbents in different pH value. Because the natural clay was chosen as the adsorbent for this experiment, the removal of Cr (VI) was limited to physical adsorption and did not involve a chemical reduction reaction. The parameters related to the chemical reduction reaction were not added to the model either. So, the model cannot be applied to adsorbents with nanoparticles loaded on, which normally has higher adsorption capacity.

Based on data obtained from Cr (VI) removal experiment by surfactant-modified bentonite. Castro et al.[72] used response surface methodology to developed a model. Response surface methodology is essentially a combination of mathematical and statistical tools useful for planning experiments, constructing models by examining parameter interactions, and optimising processes [101] . The model successfully predicted the adsorption capacity of Cr (VI) at different additions and pH values for this material.

However, as the response surface methodology is based on fitting the mathematical models to existing experimental results and validation of the models obtained through statistical techniques [102]. The model can only be

applied to materials that provide the source of the model data and cannot be used to predict a new material that has not been experimentally tested.

2.4 Summary of state-of-art work

From the previous literature review, chemical precipitation and physical adsorption are the most widely used techniques for Cr (VI) removal due to their excellent environmental suitability and low cost. Materials based on chemical precipitation and physical adsorption are currently divided into three categories.

1. Nano-iron based modifications or the addition of other metals to form bimetallic materials. These materials lack directionality in their ability to reduce Cr (VI). They also have a high degree of agglomeration due to van der Waals forces and electrostatic gravitational forces. These limited their ability to achieve higher Cr (VI) removal capacities. Also, due to its nano size, it is difficult to be re-collected for use. The addition of adsorbents to these materials that can adsorb the surrounding Cr (VI) can improve their directivity, while some of the adsorbents may help to reduce agglomeration.

2. Natural clay or biomass based materials with some simple processing or modification. This type of materials are relatively inexpensive, but due to its natural properties, they are usually not very pure with relatively low specific surface area compared to other materials. The expected high Cr (VI) removal capacity cannot be achieved. It is worth noting that in some cases, very high Cr (VI) removal capacities have been reported for these materials, but the experimental conditions are mostly in strongly acidic solutions, which are not

suitable for practical applications. Given the large effect of pH on Cr (VI) removal capacity, it cannot be considered that practically high Cr (VI) removal capacities have been achieved.

3. High surface area based materials (e.g. graphene, carbon nanotubes) with nanometals (e.g. iron) attached to their surfaces. These materials have a higher Cr (VI) removal capacity than the first two. Nanometals in these materials tend to have smaller particle sizes due to the spatial site resistance of the adsorbent. However, the smaller particle size means that they are more susceptible to oxidation by the environment and thus lose their reducing properties. The formation of bimetallic particles by adding a metal with a higher reduction potential will help to maintain their reduction capacity.

Chapter 3 Methodology

3.1 Materials and Instruments

Materials

Graphene oxide (GO) is synthesized by a modified Hummer's method using graphite powder as a raw material [103]. MWCNTs and Nickel (II) chloride hexahydrate are bought from Sigma-Aldrich (Dorset/UK). $FeCl_3 \cdot 6H_2O$ and potassium dichromate ($K_2Cr_4O_7$) are bought from SLS (Scientific Laboratory Supplies), nickel powder (average particle diameter 2.2-3.0 um), polyvinyl pyrrolidone (PVP) and chromium (III) chloride hexahydrate ($CrCl_3$) are purchased from Alfa Aesar. Sodium borohydride ($NaBH_4$) is bought from Fisher Scientific Ltd. 1,5-Diphenylcarbazide (DPC) is purchased from Sigma-Aldrich. The chemicals are used as received without further purification.

Scanning Electron Microscope and Energy-dispersive X-ray spectroscopy

Scanning Electron Microscope (SEM, SU8230, Hitachi) equipped with Energy-dispersive X-ray spectroscopy (EDS) is used to characterizese the bonding patterns and elemental distribution of the various components in a multi-component material. It is used to confirm that the prepared sample meets expectations.

In SEM testing, the electron beam is used as the illumination source, and the focused electron beam is irradiated onto the sample in the form of a raster-like scan to produce secondary electrons and backscattered electrons through

the interaction between the electrons and the sample, which are then collected and processed to obtain a magnified image of the microscopic morphology.

The principle of EDS is that each element has its own characteristic wavelength of X-rays. The size of the characteristic wavelength depends on the characteristic energy ΔE released during the energy leap, and the energy spectrometer takes advantage of the different characteristic X-ray photon energies of different elements to carry out compositional analysis.

Before SEM and EDX test, the sample was ground into powder form with a mortar and pestle, then the sample was glued to the conductive adhesive on the measuring table, after that gold was sprayed evenly on the surface of the sample to enhance its conductivity.

Transmission electron microscope

Transmission electron microscope (TEM, FEI Tecnai TF20) is used to observe the morphological changes in the components of the material before and after Cr (VI) removal tests to help analyse the reaction mechanism.

TEM characterisation involves the projection of an accelerated and concentrated electron beam onto a very thin sample, where the electrons collide with the atoms in the sample and change direction, resulting in stereo angular scattering. The magnitude of the scattering angle is related to the density and thickness of the sample, so that different images of light and dark can be formed, which will be displayed on the imaging device after magnification and focusing. Due to the very short de Broglie wavelength of electrons, the resolution of transmission electron microscopy is much higher than that of optical microscopy.

Before doing the TEM test, the ground sample was taken and dispersed in ethanol solution, sonicated for more than 30 min, and a small amount of the mixture was dropped onto an ultra-thin carbon grid and placed on a sample bench for testing.

Fourier-transform infrared spectroscopy

Fourier-transform infrared spectroscopy (FTIR) experiments are performed with Thermo Scientific Nicolet iS10 FTIR Spectrometer (Thermo Scientific) to characterise the type and content of residual oxygen-containing groups on RGO and MWCNTs.

The sample to be tested is irradiated with infrared light of continuously varying frequency, and the molecular groups absorb the radiation of characteristic frequencies, and their vibrational or rotational motion causes a change in dipole moment, resulting in a jump in the vibrational and rotational energy levels of the molecule from the ground state to the excited state, and obtain a molecular absorption spectrum.

The FTIR instrument is equipped with Attenuated total reflection (ATR), which allows direct measurement of the powder after grinding, without the need to disperse the powder in solution. The sample powder was ground for 5 min and then measured. The detection wavelengths ranged from 650 to 4000 cm^{-1} with a resolution of 2 cm^{-1}.

BET surface area

BET surface areas are tested on Tristar 3000 (Micromeritics) to analyze the effect of different components on the specific surface area of the material and the pore size distribution within the material.

Nitrogen is used as the adsorbent and helium or hydrogen as the carrier gas. The two gases are mixed in a certain ratio to reach a specified relative pressure and then flow through the solids. When the sample tube is held in liquid nitrogen, the nitrogen in the gas mixture is physically adsorbed onto the surface of the sample, while the carrier gas is not. At this point an adsorption peak appears on the screen. When the liquid nitrogen is removed and the sample tube is brought back to room temperature, the adsorbed nitrogen gas is desorbed, and a desorption peak appears on the screen. Finally, a known volume of pure nitrogen is injected into the mixture and a calibration peak is obtained. From the peak areas of the correction and desorption peaks, the amount of sample adsorbed at that relative pressure can be calculated.

Before the BET test, the sample is ground to a powder and vacuum dried overnight. The sample is placed in a sample tube and an appropriate amount of liquid nitrogen is added to the liquid nitrogen tank so that the sample tube is immersed in liquid nitrogen. It is necessary to ensure that the sample tube is airtight when connected to the characterisation equipment.

Ultraviolet-visible spectroscopy

Ultraviolet-visible spectroscopy (UV-vis) spectra of samples are performed with UV spectrophotometer UV-1800 (Shimadzu) to quantify the concentration of Cr (VI) in solutions.

In the UV test, a continuous spectrum of electromagnetic waves in the ultraviolet-visible region is used as a light source to irradiate the sample. By measuring the absorption of light at a specific wavelength or within a certain wavelength range of the substance, qualitative and quantitative analysis of the substance is carried out.

Before the UV test, The UV spectrophotometer needs to be preheated. Then, after “auto zero” without sample and “baseline” with DI water, samples are carried out to be tested. The detection wavelengths ranged from 200 to 800 nm with a resolution of 1 nm.

Dynamic light scattering

Sample size characterization is investigated by dynamic light scattering (DLS) measurements using the Zetasizer Nano ZS (Malvern). This is used to analyse the loading and agglomeration of metal particles.

Dynamic light scattering (DLS) is based on the Brownian motion of dispersed particles. When particles are dispersed in a liquid, they move randomly in all directions. The principle of Brownian motion is that particles in solution continuously collide with solvent molecules, which causes particle motion. Smaller diameter particles move at a higher velocity than larger particles [104].

During the measurement, a monochromatic light source is directed into the sample through a polarizer. The scattered light then passes through a second polarizer, after which it is collected. Due to the Brownian motion, the scattered light fluctuates with time and the rate of fluctuation is related to the hydrodynamic diameter of the particles in solution, from which the size of the particles in solution can be calculated. Zetasizer Nano ZS ensures confidence in the particle size by scattering and collecting at multiple angles.

Based on the measurement principle of DLS, the measurement target has certain limitations:

Samples can be dispersed relatively consistently in water. The solution concentration must be low enough so as to reduce multiple scattering of light between different particles.

The size of the particles to be measured is usually strictly limited by the wavelength of the light emitted by the instrument, and for the instrument used in this experiment, the test range is 0.3 nm to 10 μm.

The sample particles should not have more than three concentrated areas of particle size distribution, otherwise the accuracy and validity of the data will be affected.

For the measurement progress, firstly switch the measurement mode to "size", then set the temperature, absorbance and other parameters of the solution in "manual" of "measure". Then disperse a small amount of sample in DI water and shake for 1 minute. Control the concentration of the sample so that the solution remains translucent. Add the rated volume of solution to the tube. Place the tube into the instrument in the correct orientation and start the test.

X-ray photoelectron spectroscopy

X-ray photoelectron spectroscopy (XPS) is used to confirm the existence and the valence states of elements before and after the Cr (VI) removal experiment.

In the XPS test, the sample is irradiated with X-rays, by measuring the kinetic energy and the number of electrons escaping from 1 nm to 10 nm below the surface of material in the range. The X-ray photoelectron spectrum is obtained.

In this experiment, the milled sample powder is glued to the test bench by means of conductive double-sided tape. The measured scan resolution is 1.0 e V, with high resolution scans of 0.1 e V in the Fe2p and Cr2p regions

X-ray diffraction

X-ray diffraction (XRD, Bruker D8) is used to characterize the crystalline structure of the sample. In this experiment, the scan range is set to 10-70 °2θ. Step size is 0.05°. And 1 seconds per step.

The wavelength of the X-rays is similar to the spacing between the atomic planes inside the crystal, and the crystal can act as a spatial diffraction grating for the X-rays. A beam of X-rays striking an object is scattered by the atoms in the object, each of which produces scattered waves which interfere with each other and as a result produce diffraction. The superposition of the diffraction waves results in the intensity of the rays strengthening in some directions and weakening in others. Analysis of the diffraction results leads to the crystal structure.

Micromixer chip

Micromixer chip purchased from Dolomite is used to replace traditional mechanical stirring in the synthesis of some samples to improve the dispersion of the sample.

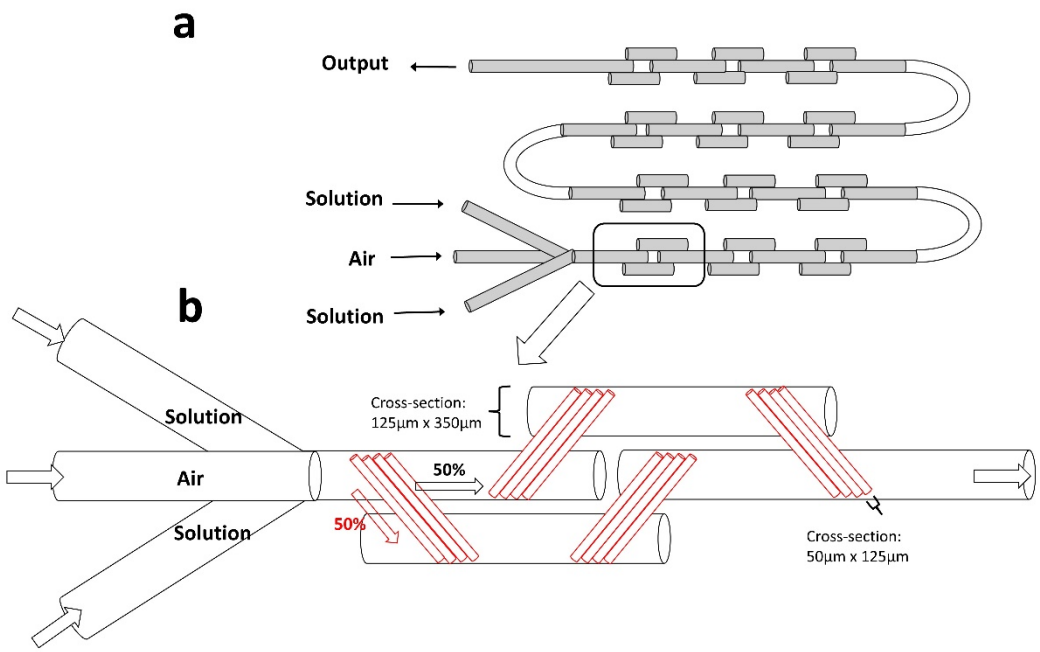

Figure 3-1 Micromixer chip: the whole chip (a) and the mixing stage (b).

The chip depicted in Figure 3-1 is a static mixer and has three entrances and one exit. Two entrances were connected to 2 syringes with two feeding solutions, and one entrance was connected to an air bottle to produce small solution drops in the chip. The primary means for enhanced mixing property in this chip is to disrupt the laminar flow into controlled mixing stages by physical forcing liquids to mix. There is 12 mixing stage for one whole mixing process. At the beginning of each mixing stage, part of solution successively goes through the 4 small conduits to another main tube, while the rest continues to go through in the original main tube. The internal channel cross-section size of the microchip is 125 um × 350 um (depth × width) and 50 um × 125 um for the conduit. Similar processes occur 4 times in every mixing stage. Meanwhile, it's a sinuous microchannel that could generate convection at every turn to help the mixing. A pump was used to control the injection speed. The injection speed was set to 10 uL/min for each syringe. At this

speed, the back pressure is around 0.08 bar. Due to the speed limitation, the production rate of the composite material is limited to 2.46 mg per hour. The production rate is only limited to sample 4 and 5 in chapter 4. Not applied to other samples in chapter 4 and all samples in chapter 5 and 6.

After the mixing stage, GO is well dispersed. More detailed description of the micromixer chip is included in the Appendix A.

3.2 Methodology

Based on the literature reported above, a target material should have both a high physical adsorption and chemical reduction capacity for Cr (VI).

The physical adsorption capacity increases the concentration of Cr (VI) in the vicinity of the material and increases the directionality of the chemical reduction capacity of the material. It also provides part of the Cr (VI) adsorption capacity based on its own physical adsorption.

The chemical reduction capacity reduces Cr (VI) to Cr (III), which is less susceptible to re-oxidation in nature, preventing secondary contamination. The chemical reduction method will provide the majority of the Cr (VI) adsorption capacity.

With this requirement, multi-component materials are a potential development direction. Some components provide physical adsorption capacity and some components provide chemical reduction capacity.

From previous reports, new materials based on carbon, such as graphene and carbon nanotubes, which have extremely high specific surface area, are good materials for providing physical adsorption capacity. Nano iron particles, on

the other hand, are an excellent choice for providing reduction capability. At the same time, the loading of another metal with a higher reduction potential (e.g. nickel) on the surface of iron nanoparticles to form bimetallic nanoparticles can enhance its reactivity. Combining FeNi bimetals with graphene to form a triple material is where high Cr (VI) removal capacities can be expected.

In order to achieve the loading of FeNi bimetallic particles onto the RGO. The FeNi bimetal is planned to be prepared by reducing Fe (III) chloride hexahydrate and Ni (II) chloride hexahydrate with an excess of sodium borohydride (NaBH4). Graphene oxide (GO) is also reduced by sodium borohydride (NaBH4) to remove the oxygen-containing groups from the surface. The reduction process is carried out in the presence of the dispersant polyvinyl pyrrolidone (PVP) and is ensured by mechanical stirring or shaking. Magnetic stirring should be avoided during the reduction of iron (III) to prevent the effect of magnetism on the zero-valent iron. The three-in-one material is reached by the co-precipitation of the FeNi metal particles with RGO so that the FeNi metal particles are physically adsorbed by the RGO.

In the new material, the RGO predicted acts as a carrier for the FeNi bimetal, and the presence of the RGO will reduces the agglomeration of the FeNi bimetal to a certain extent. Meanwhile, FeNi bimetal and Fe loaded RGO will be synthesised as a comparison.

In order to verify the adsorption capacity of the new material for Cr (VI), Cr (VI) removal experiments need to be carried out. As literature reported [105], in an acidic or neutral environment, 1,5-Diphenylcarbazide (DPC) couples with Cr (VI) to form a purple solution with a significant absorption peak at λmax = 545

nm. By measuring the absorption peaks at λmax = 545 nm by DPC with different concentrations of Cr (VI) in the UV-Vis spectrum, a mathematical relationship between the absorption peaks and Cr (VI) can be determined over a range. This mathematical relationship can be used to determine the concentration of Cr (VI) in solution.

In theory, in the Cr (VI) removal experiments, the RGO will adsorbs Cr (VI) from the solution to the surrounding area, increasing the concentration of Cr (VI) in the surrounding area and speeding up the reaction rate between Fe and Cr (VI). At the same time, the RGO itself will provides a small amount of Cr (VI) removal capacity through physical adsorption.

Fe will act as a reducing agent to convert Cr (VI) to Cr (III). Nickel will be a catalyst to accelerate the reaction between Fe and Cr. Cr (VI) reacts with Fe (0) is expected form precipitates. These precipitates may encapsulate Fe (0), preventing the rest iron from participating in the reaction. RGO will compete with Fe in the attachment of precipitates and, relying on its ultra-high specific surface area, may reduce the coverage of Fe by precipitates.

After the Cr (VI) removal experiment, the solids in solution will be collected. After reduction and filtration, it will be used again for the Cr (VI) removal experiment.

The results show that the material has almost lost its Cr (VI) adsorption capacity, indicating that the material is not reusable. This is due to the fact that a large amount of Fe was encapsulated by the RGO during the second reduction, preventing it from participating in the Cr (VI) removal experiments.

Due to the unique tubular structure of MWCNTs and their extraordinarily high specific surface area, it is tough to encapsulate FeNi bimetallic particles by

MWCNTs. MWCNTs will be used to replace RGO to achieve reusability and expect a higher Cr (VI) adsorption capacity.

Most of the Cr (VI) removal materials currently being investigated are multi-phase materials. Determining the optimal material ratios for Cr (VI) absorption capability requires a substantial amount of effort. One of the potential avenues of research is the partial substitution of conventional experiments with computer simulations. Fe/MWCNTs, a high-purity and relatively easy-to-simulate component material, was chosen for modelling in this investigation as there are no relevant literature reports.

Cr (VI) removal experiments need to be carried out with pure Fe (0) and pure MWCNTs. The relevant fixed parameters for Fe (0) and MWCNTs can be determined by fitting them to the equations based on the deformation of classical reaction rate equation 3-1.

$$\frac{d[Cr(VI)]}{dt} = -k[SC][Cr(VI)] \tag{3-1}$$

Where [Cr (VI)] is the hexavalent chromium concentration (mmol/L) at time *t* and *k* its rate coefficient (L mmol^{-1} min^{-1}), [SC] represents the equivalent sample concentration at time t capable of reducing Cr (VI) (mmol L^{-1}).

For Fe/MWCNTs, the limiting factor for the Cr (VI) removal capacity is that some of the iron is encapsulated in the precipitate and cannot continue to participate in the reaction. Analysis of the products of the reaction of Fe/MWCNTs with Cr (VI) by TEM and XPS may allow a quantitative calculation of the encapsulation of Fe by the precipitates during the reaction.

By introducing the quantitative analytical data of Fe encapsulation by precipitates into Equation 2-1 and bringing in the relevant fixed parameters obtained for the reaction of Fe and MWCNTs with Cr (VI), it may be possible to quantify the reaction state of Fe/MWCNTs with Cr (VI) at any given moment. The component parameters can be adjusted to simulate different ratios of Fe/MWCNTs.

At last, the accuracy of the model will be verified by conducting Cr (VI) removal experiments with different fractions of Fe/MWCNTs.

3.3 Chapter summary

The Chapter present the materials and methodology to achieve design the targeted nanomaterial that have both high physical adsorption and chemical reduction capacity for Cr (VI).

As shown in Figure 3-2, the RGO with its very high specific surface area provides a strong physical adsorption capacity and the FeNi bimetal provides high chemical reduction capacity. By combining them together, lower agglomeration of metal particles and higher Cr (VI) adsorption capacities can be expected.

RGO in the form of flakes will encapsulate the iron nanoparticles, reducing the Cr (VI) adsorption capacity and losing reusability. This can be avoided by using MWCNTs due to their special tubular two-dimensional structures.

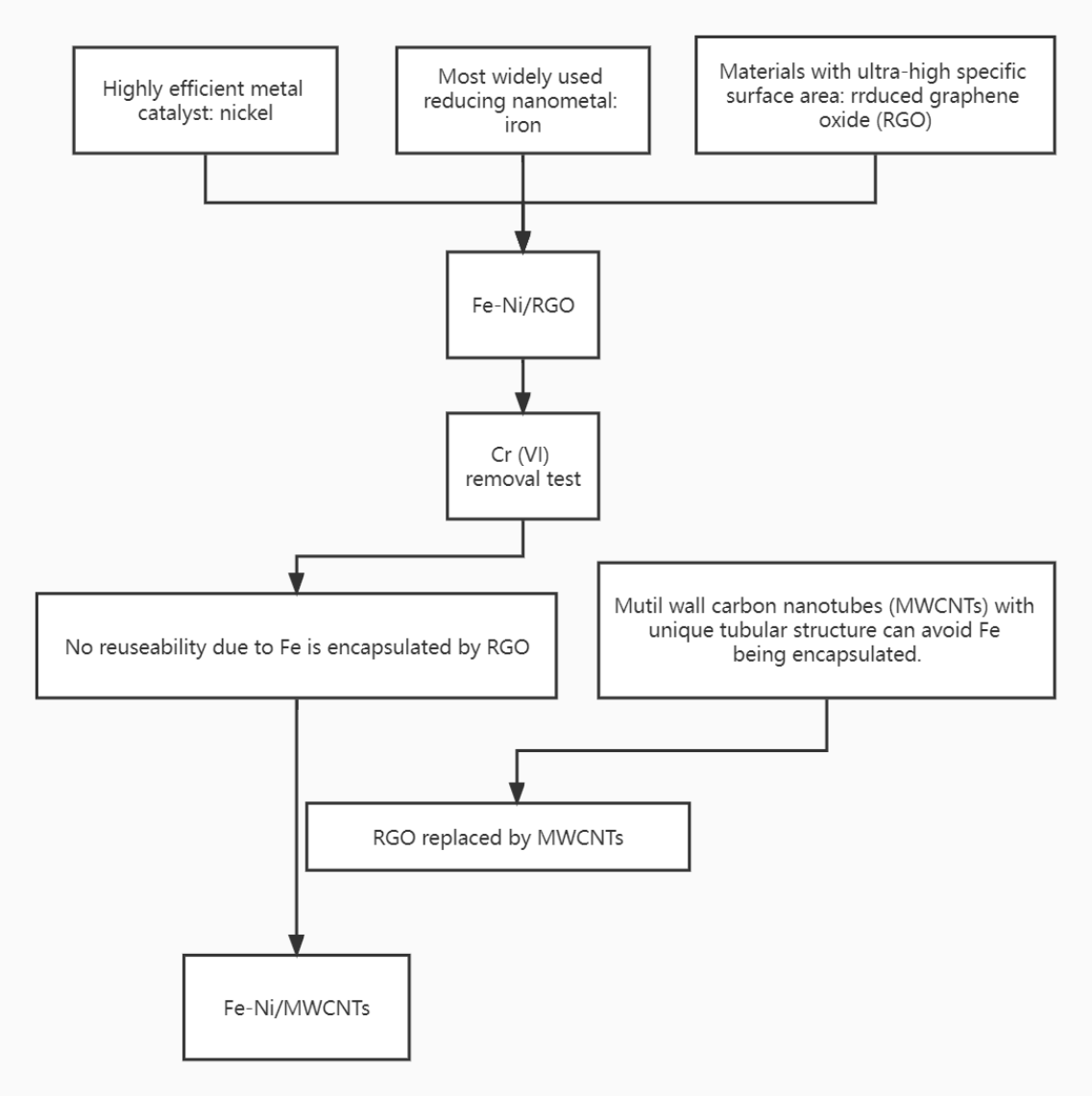

Figure 3-2 Methodology for experiment part

For the simulation part, as shown in Figure 3-3, the experimental data for the removal of Cr (VI) from pure iron and pure MWCNTs will be obtained, and will be fitted with to the reaction rate equation to obtain relevant parameters. The structure of the reaction products of Fe/MWCNTs with Cr (VI) will also be analysed to determine the mechanisms limiting the removal capacity of Cr (VI). The mechanisms affecting the Cr (VI) removal capacity will be quantified and then brought into the reaction rate equation, combing with the collected

parameters to develop a model for predicting the Cr (VI) removal capacity. After that, parameters in model will be adjusted to simulate different Fe/MWCNTs material ratios, and the reliability of the model will be verified experimentally.

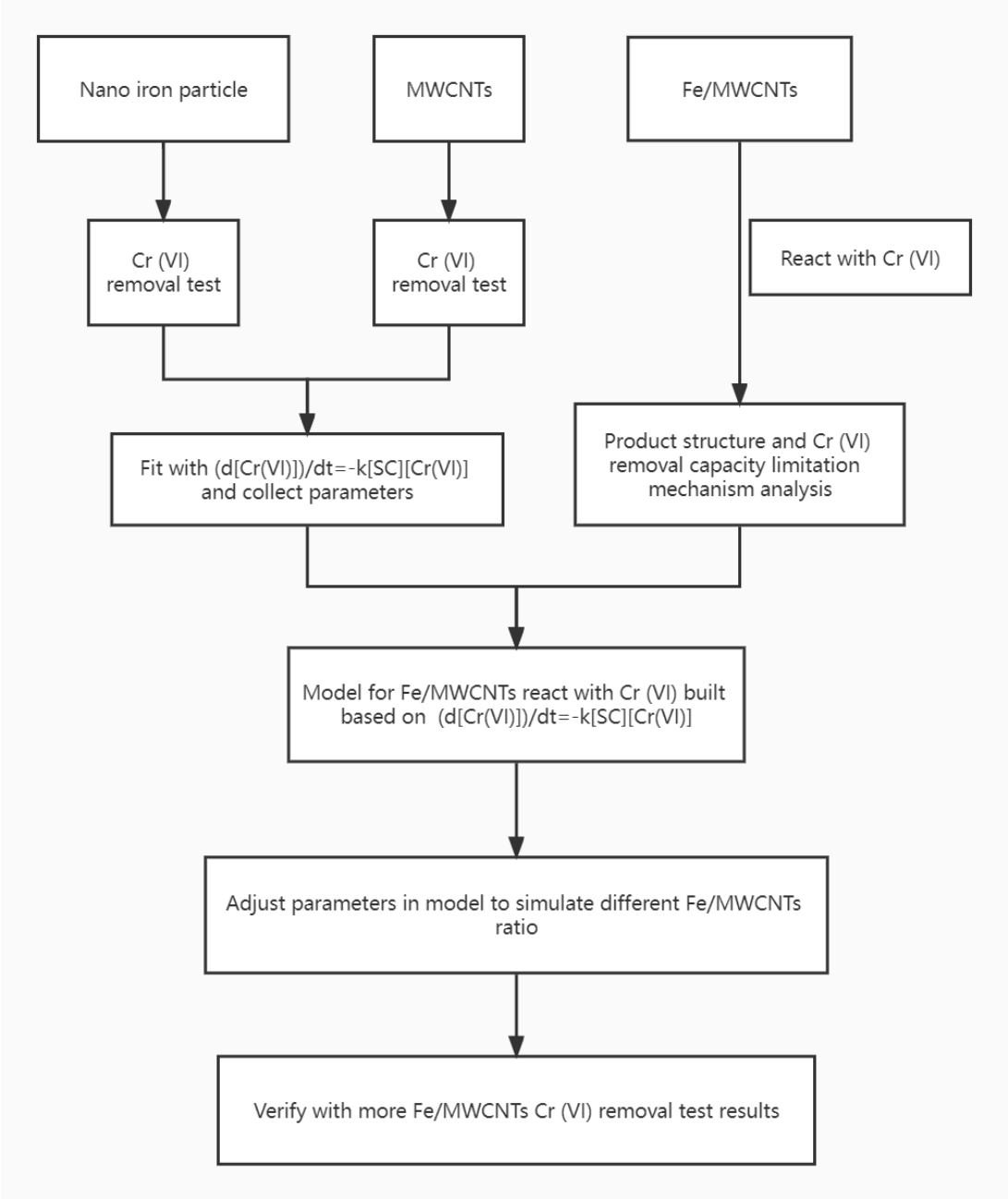

Figure 3-3 Methodology for simulation part

Chapter 4

Ni-Fe/RGO Nanocomposites for Hexavalent Chromium Reduction in Aqueous Environment

In order to further increase the Cr adsorption capacity, this work attempts to combine the advantages of bimetallic particles and adsorbent loading materials onto the adsorbent. Since iron is the most often employed reducing agent in the field of Cr adsorption and nickel is an excellent catalyst, iron-nickel was selected to make the bimetal. As one of the substances with the greatest specific surface area, RGO was selected as the sorbent.

4.1 Preparation of ZVI-NPS, Fe/RGO, and Fe-Ni/RGO Composites

0.66 g 30 wt% $FeCl_3 \cdot 6H_2O$ solution is added into 50 mL of deionized water under magnetic stirring, forming $FeCl_3$ solution. 0.04 g GO and 1.0 g PVP are added into the obtained $FeCl_3$ solution and stirred for 30 minutes. Then 21.58 mg nano-nickel powder is added and stirred overnight. The nickel powder shall be surface oxidised by the oxygen in the water. After that, 40 mL of 18.75 mg/mL $NaBH_4$ is added dropwise into the system and stirred overnight. $NaBH_4$ worked as a reducing agent and is expected to reduce Fe (III), GO and nickel oxide to Fe (0) NPs, RGO and Ni (0) NPs, respectively. The RGO is served as the base material to support Fe/Ni bimetal. As H_2 is produced during this step, careful control is needed. The reaction equation is listed below:

$$Fe(H_2O)_6{}^{3+} + 3BH_4{}^{-} + 3H_2O = Fe^0 \downarrow + 3B(OH)_3 + 10.5H_2 \uparrow$$

For some samples, a micromixer chip (part number 3200401, Dolomite Centre Ltd) is used to replace the magnetic stirring to enhance the mixing and dispersion of GO, Fe (0) and Ni. The final product is collected by vacuum filtration, washed with ethanol three times, dried in a vacuum oven overnight, then collected and stored with nitrogen protection. A total of five samples are prepared for the purpose of comparison, as given in Table 4-1.

Table 4-1 Detailed reaction conditions of different samples

Sample No.	30 wt% $FeCl_3 \cdot 6H_2O$	GO	Ni	PVP	$NaBH_4$	Micromixer (Yes/No)
Sample 1	0.66 g	0.04 g	\	\	0.75 g	No
Sample 2	0.66 g	0.04 g	\	1.00 g	0.75 g	No
Sample 3	0.66 g	0.04 g	21.58 mg	1.00 g	0.75 g	No
Sample 4	0.66 g	0.04 g	\	1.00 g	0.75 g	Yes
Sample 5	0.66 g	0.04 g	21.58 mg	1.00 g	0.75 g	Yes

4.2 Results and Discussion

4.2.1 Particle Stability, Size, Morphology and Elemental Analyses

Influence of mixing approach on composite particle stability

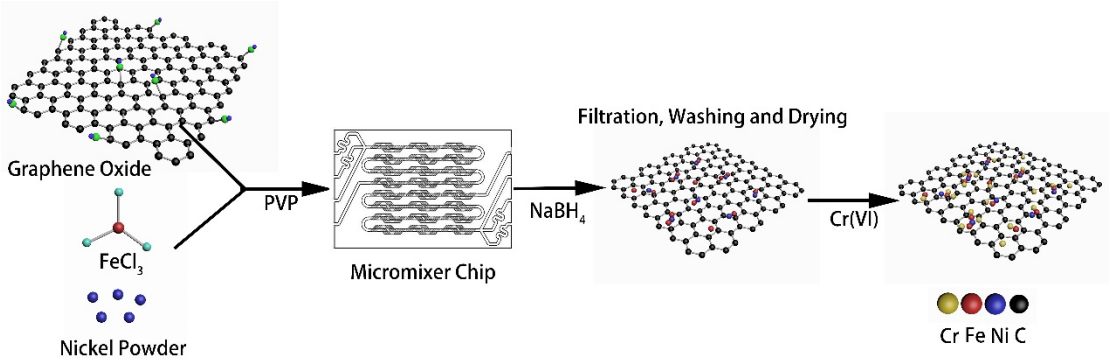

Figure 4-1 Schematic illustration of the preparation process of Fe-Ni/RGO composite and its adsorption/reduction of Cr (VI)

Fe-Ni/RGO composites with the ability to absorb/reduce Cr (VI) are synthesized as shown in Figure 4-1. Different mixing methods are utilized in this study to prepare samples, *i.e.*, magnetic stirring and micromixer chip. The sample solutions obtained by different approaches show different colour and diaphaneity, as shown in Figure 4-2

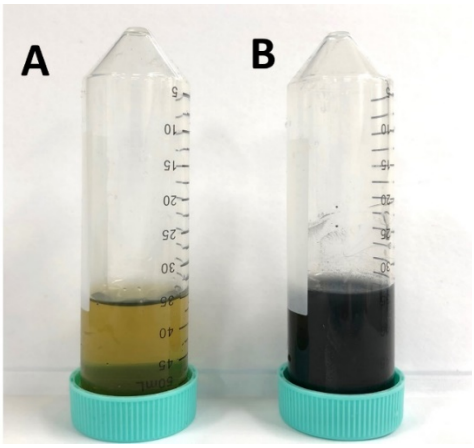

Figure 4-2 Image of solutions mixed by different approaches: microchip (A) and magnetic stirring method (B).

The solution mixed by microchip shows high diaphaneity with yellow colour, which means that the GO is dispersed very well. In contrast, the solution processed by magnetic stirring presents an opaque colour, indicating the instability and the presence of large GO agglomeration.

Particle size analysis

To determine particle size distribution, 15 mg of the sample solution is added into 50 mL deionized water under sufficiently stirring, and a centrifuge is used to separate the sediments and liquid. The upper liquid is tested by Zetasizer, Malvern. As a comparison, Fe-Ni bimetal is also tested under the same condition. Results are shown in Figure 4-3 and Table 4-2. Sample 1-3 show two peaks. It is due to the magnetic stirring process, which could not disperse GO sheets well and some of them became agglomerated. Some Ni (0) or Fe (0) NPs are not fixed onto the RGO surface, resulting in the presence of the second peak around 150 nm. For Fe-Ni bimetal material without RGO, the aggregation results in the presence of the peak around 400 nm.

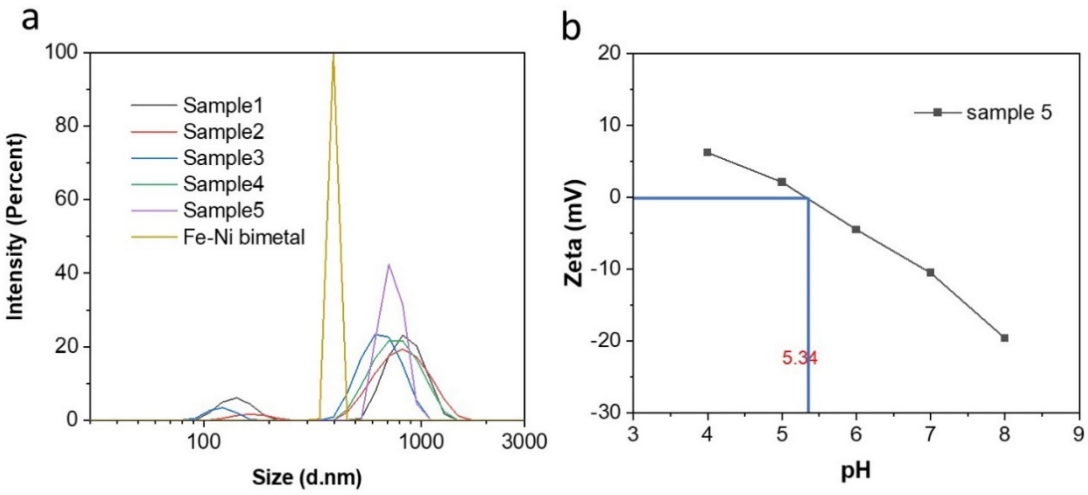

Figure 4-3 (a) Particle size distribution measured by DLS and (b) Zeta potentials of sample 5

Table 4-2 Size distribution determined by the intensity

	Peak 1		Peak 2	
	Size (d.nm)	% intensity	Size (d.nm)	% intensity
Sample 1	858.0	81.3	141.7	18.7
Sample 2	840.7	94.7	166.9	5.3
Sample 3	663.2	91.4	120.9	8.6
Sample 4	783.4	100	/	/
Sample 5	737.0	100	/	/
Fe-Ni bimetal	395.9	100	/	/

As a comparison, sample 4 and 5 produced by the microchannel mixing show only one distribution peak, which means a non-presence of loose and free Ni

(0) and Fe (0) NPs in the system. Because GO is well dispersed in solution and may provide enough points for Ni (0) and Fe (0) NPs to fix on, promoting the formation of an integral three-in-one composite. The results demonstrated that the microchip has a much better mixing and dispersing effect, so as to enable the prepared samples with better properties. For sample 5, the zeta potential decreases from 6.24 mv to -19.60 mv, and the pHZPC value is 5.34 mv.

Morphology and Elemental Analyses

The morphology and structure of the iron nanoparticles/RGO are observed by SEM and TEM, respectively. Figure 4-4 (a) shows that sample 5 is unordered stacking with a two-dimensional sheet structure; the size of the sheet is about 1 μm, which is in good consistent with the DLS result. The thickness of the sheet is less than 50 nm. The TEM images in Figure 4-4 (d) show the RGO sheet has a length of the side of about 1 μm, which is well consistent with the SEM results. It also revealed that Fe-Ni nanoparticles are well loaded on or connected to the sheet surface with a size of about 20-50 nm. In Figure 4-4 (e), there are no obviously lattice fringes in the HRTEM image. It indicates that the Fe-Ni particles are amorphous. Because the sample being synthesized by the liquid phase usually lends to a low degree of crystallinity or amorphous.

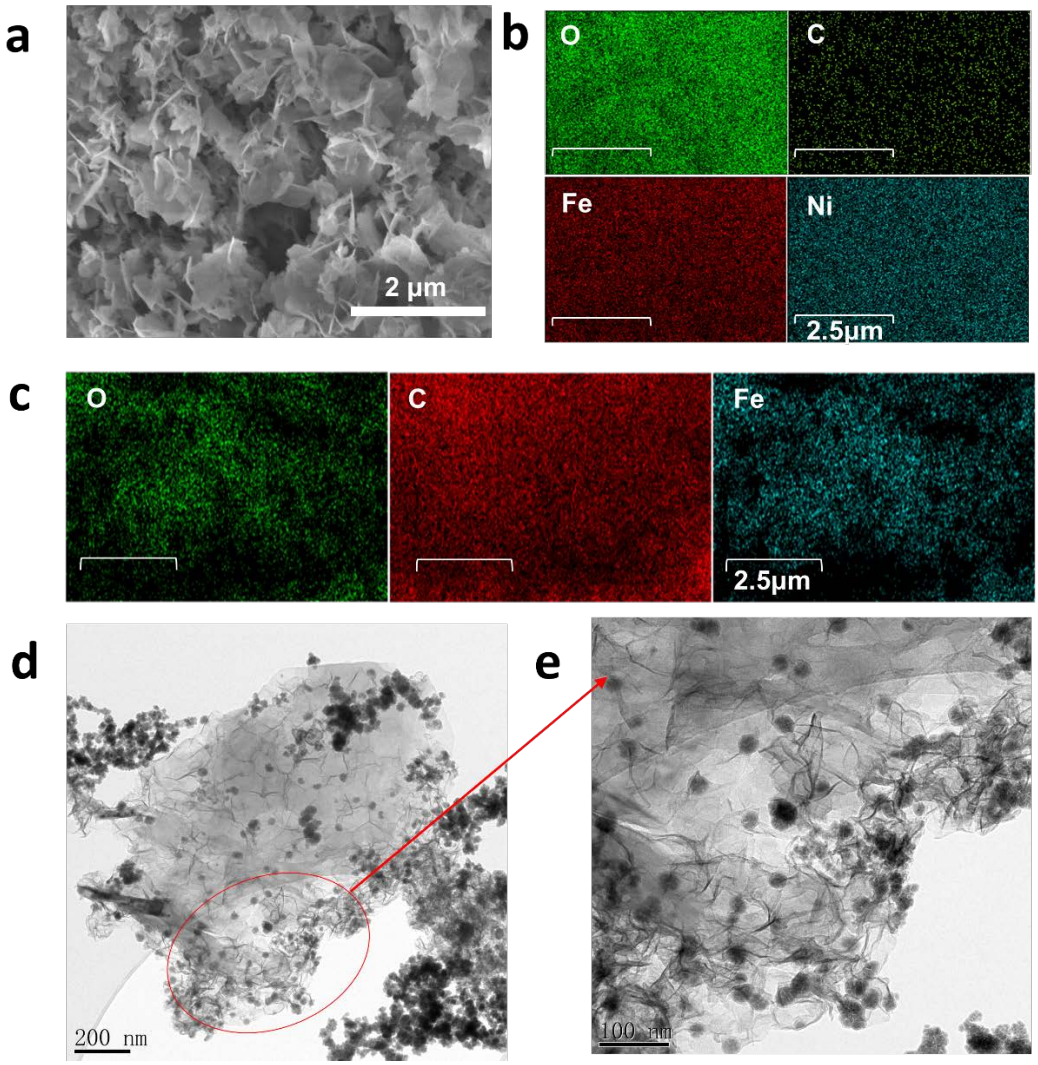

Figure 4-4 (a) SEM, (b) EDS images of sample 5, (c) EDS images of Sample 2 (d) TEM and (e) HRTEM of Sample 5

Energy-dispersive X-ray spectroscopy (EDS) is used to analyse the elemental information of the sample. The data for sample 2 and 5 are given in Figure 4-4 (c) and Figure 4-4 (b) for comparison. Because nitrogen protection is not used in the whole synthesis process, metallic particles can be inevitable partially oxidised, leading to the presence of O in the EDS map. For sample 2 (Figure 4-4 (c)), Fe and O element shows a similar distribution, which is different from that of C, suggesting that most of the oxidation is associated with Fe. However, a much uniform distribution of Fe (0) and Ni (0) is observed

for sample 5, Figure 4-4 (b). The use of a microchip, which has a better mixing effect than traditional stirring, leads to a more uniform distribution of metallic particles on RGO.

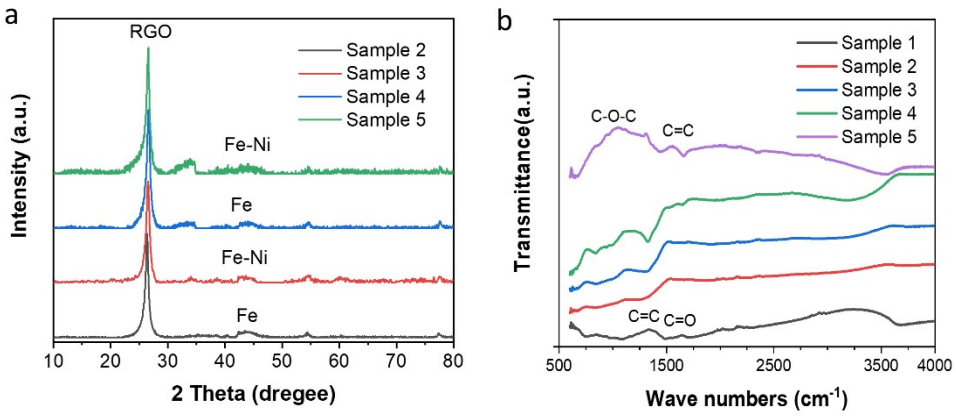

Figure 4-5 (a) XRD patterns of sample 2-5 and (b) FTIR spectra of sample 1-5

Figure 4-5 (a) shows XRD patterns of sample 2-5. A noteworthy diffraction peak is found at 26.7° for all the samples, which belongs to the (002) diffraction of RGO. [106] The Fe-Ni-B, and Fe (0) particles consist of a broad peak in the 2θ range of 40°~50° and no crystalline peak is observed, revealing an amorphous structure.[107] The result is consistent with the HRTEM image result. The amorphous structure is expected to enable samples with a higher BET surface area.

FTIR spectra are also tested for all the samples to characterize the RGO, as shown in Figure 4-5 (b). For sample 1, the peak at 1495 cm^{-1} shows that the C=C skeletal vibration of the unoxidised graphitic [108], of which the C=C has not been reduced to C-H. Absorption bands related to the oxygenated functional groups dominate the FTIR spectrum. At 1081 cm^{-1}, the alkoxy C-O-

C stretching vibration is observed [109]. Peaks at 1705 cm^{-1} belong to the C=O stretching vibration in carbonyl and carboxyl moieties [110]. The O-H stretching vibration in water is at 3673 cm^{-1} [111]. The spectrum shows there are some oxygenated functional groups on it. As there is no surfactant added for sample 1, it may be because that the aggregation of iron and GO prevented the $NaBH_4$ from reducing GO. For sample 2, 3 and 4, there is only a tiny peak, which suggests that nearly all the oxygenated functional groups on GO are reduced. Sample 3 and 4 displays a similar result. For sample 5, the O-H stretching vibration in water is at 3538 cm^{-1}. C=C skeletal vibration of the unoxidised graphitic (1654 cm^{-1}) is observed. It means that sample 5 is not entirely reduced, which is due to the reoxidation in the air during the drying or storage process. Compared with sample 1, the disappearance or significant decrease in the intensity of C-O-C, C=C and C=O band in the spectra of sample 2-5 is observed, indicating that the oxygen-containing functional groups in the GO are effectively reduced. However, for all the samples, there are still some oxygen-containing groups on the RGO surface, making the reduced GO be slightly negatively charged. As the major Cr (VI) status is $HCrO_4^-$ and $Cr_2O_7^{2-}$ [112], this shall slightly decrease the adsorption capacity due to the electrostatic force.

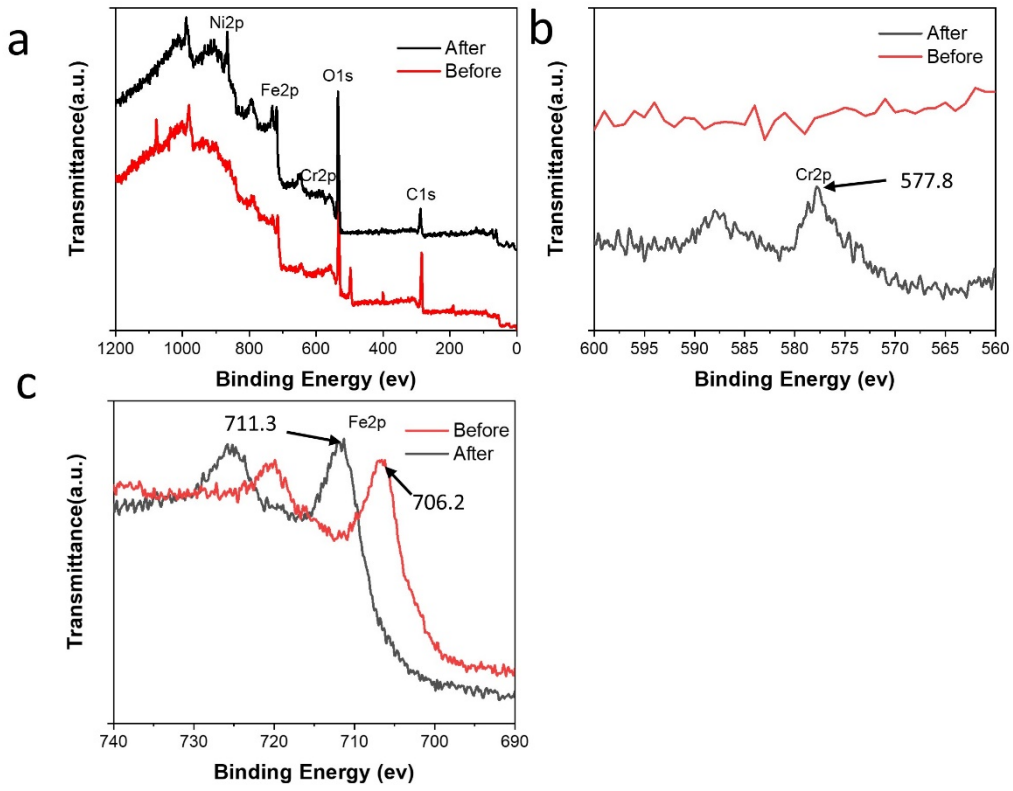

Figure 4-6 XPS spectra of sample 5 before and after Cr (VI) adsorption experiment: (a) wide scan, (b) high resolution spectra of Cr and (c) high resolution spectra of Fe

Figure 4-6 (a) shows the XPS spectra of sample 5 before and after Cr (VI) adsorption experiment. The main elements in sample 5 are C, O, Fe and Ni. After Cr (VI) adsorption experiment, a new peak appeared around 577.8 eV along with the peaks for Cr, as shown in Figure 4-6 (b). This pick represents the Cr which is exist with Cr (III) hydroxide. [113] This confirmed Cr (VI) is reduced to Cr (III) and adsorbed by the sample. In Figure 4-6 (c), before Cr (VI) adsorption experiment, the peak for Fe is around 706.2 eV, which represents that Fe exists as Fe metal for zero-valent [114]. After Cr (VI) adsorption experiment, the pick left moved, to around 711.3 eV which belongs to Fe $(OH)_3$ [115]. This confirmed that the Cr (VI) is reduced by iron nanoparticles.

4.2.2 BET Surface Area Study

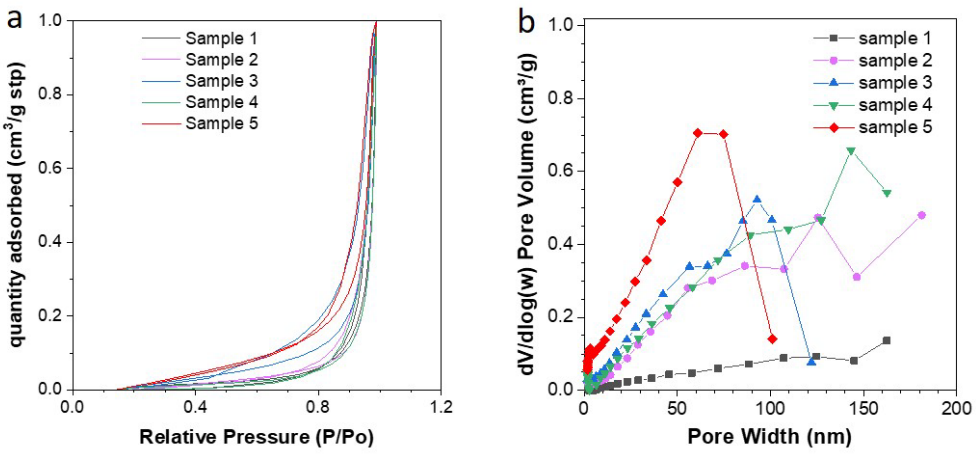

Figure 4-7 BET results of samples (a) N2 adsorption isotherms; (b) pore size distribution data.

The specific surface area of all samples is examined by Micromeritics Tristar 3000. Results are given in Figure 4-7. The adsorption-desorption isotherm shows that all samples present multilayer adsorption characteristics [116]. The interaction between the adsorbate molecules is stronger than that between the adsorbate and the adsorbent. As the adsorption process progresses, the adsorption appears self-accelerating [117]. The BET specific surface areas of sample 1-5 are calculated as 10.5805 m²/g, 36.8913 m²/g, 45.4295 m²/g, 47.4177 m²/g and 119.0778 m²/g, respectively. Sample 1 is made without any surfactant and showed the lowest BET surface area, which thereby confirmed its low dispersion. With polyvinyl pyrrolidone (PVP) as a surfactant, the BET surface area of sample 2 and 3 are increased significantly. Though the surfactant can considerably reduce the interfacial tension and improve the separation of particles, there is still some agglomeration of RGO, Fe (0) and Ni, as confirmed by the Zeta sizer results. Such agglomeration may hinder the further increase of the surface area. Comparing sample 2 and 4 with sample

3 and 5, the key factor affects their surface area is the presence of nickel powder. Nickel powder increases the composite's BET surface area originating from its own high BET surface area and combines with Fe (0) to reduce the possible aggregation of Fe (0). Meanwhile, samples with nickel powder added have smaller pore width distribution. Sample 5 is dispersed by the microchip, where GO is dispersed in solution very well and thus provides enough points for Fe (0) and Ni to decorate on. It has the highest BET surface area, up to nearly three times compared to that produced by magnetic stirring. Combining the FTIR results, Sample 5 is much easier to be reoxidised with a very high specific surface area compared to sample 1-4.

4.2.3 Cr (VI) Adsorption Capacity Analyses

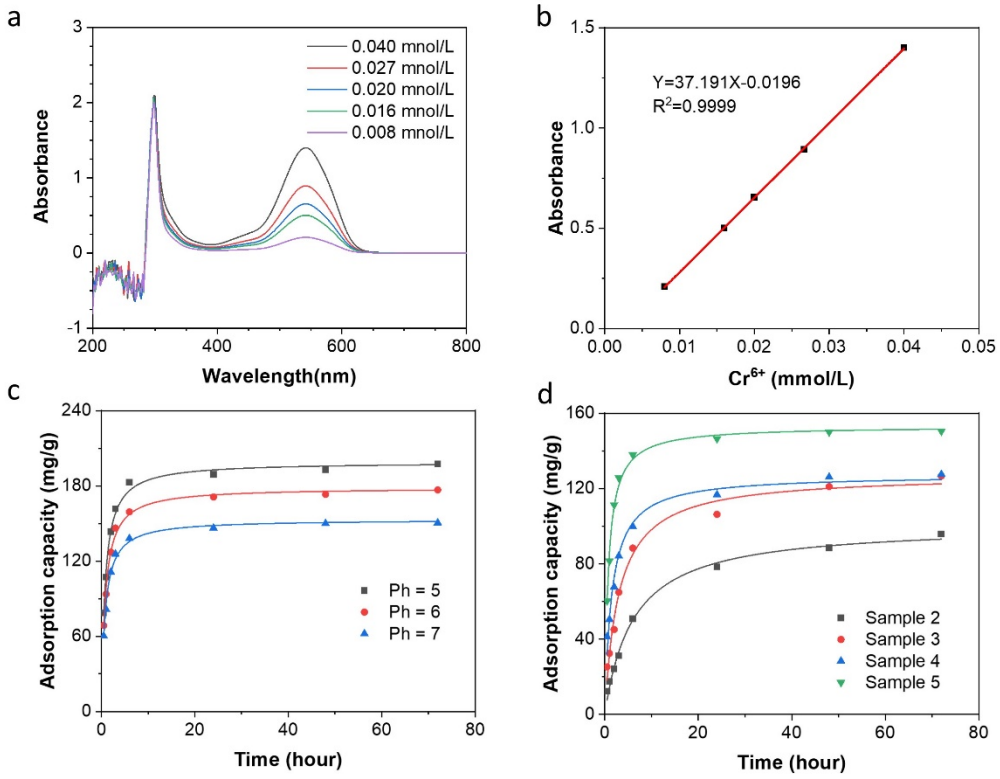

Figure 4-8 (a) UV-vis spectra of solutions of Cr (VI) reaction with DPC; (b) calibration curve line of Cr (VI) concentration (λ=545 nm); (c) Cr (VI) adsorption capacity for sample 5 at different pH; (d) Cr (VI) adsorption capacity with time and pseudo-second-order kinetic model

UV-vis spectroscopy is used to determine the Cr (VI) concentration in a solution based on a validated calibration curve. 1,5-Diphenylcarbazide (DPC) method is used to measure the Cr (VI) concentration. DPC reacts in an acid medium with Cr (VI) ions to give a violet solution, at λ_{max} =545 nm, the violet solution obtains a characteristic peak, shown in Figure 4-8 (a). DPC solution is prepared in advance: 0.2 g DPC is dissolved in 100ml acetone which contains 1ml 95% H_2SO_4 (1+1).

The calibration curve is obtained by measuring a series of concentrations of Cr (VI) solutions react with DPC solution. In detail, 23ml 0.008 mmol/L, 0.016 mmol/L, 0.020 mmol/L, 0.027 mmol/L and 0.040 mmol/L Cr (VI) solutions are prepared and respectively react with 2ml DPC solution. Then the UV-vis absorption is examined after 5 minutes at λ_{max} =545 nm. A linear relationship is shown in Figure 4-8 (b) for Cr (VI) concentration. i.e., y = 37.191x - 0.0916 with R^2 = 0.9999, where y stands for absorption and x is Cr (VI) concentration.

20 mg of each sample is added into 40 mL of 2 mmol/L Cr (VI) solution with mechanical oscillation. 0.5ml solution is drawn every time at the scheduled time and added into a bottle which includes 2 ml DPC solution and adds water to 25 ml. After 5 minutes, The UV absorption spectra of the solution are measured to determine the remaining Cr (VI) concentration. In most of the cases, the absorption became stable after 72 hours (Table 4-3). In the beginning, all Cr species are in hexavalent form, the adsorption capacity can be calculated by analysing the remaining Cr (VI) concentration. After 9 months, the Cr (VI) concentration still kept stable as Table 4-3.

Table 4-3 The Cr (VI) concentration of samples deduced for 72 hours.

	pH	Adsorption percentage	Adsorption capacity (mg/g)
Pure iron	7.0	7.99%	16.62
Sample 1	7.0	10.67%	22.19
Sample 2	7.0	46.07%	95.83
Sample 3	7.0	60.89%	126.65
Sample 4	7.0	61.33%	127.56
Sample 5	7.0	72.33%	150.45
Sample 5	6.0	84.97%	176.74
Sample 5	5.0	94.92%	197.43

It is evident that Fe (0) decorated on RGO has a much higher adsorption capacity than pure iron nanoparticles. That is due to the great adsorption ability of RGO. Cr (VI) is adsorbed to the RGO surface, where Cr (VI) can be more efficiently reduced locally by the decorated nano iron. By comparing the results of sample 2 and 4 with sample 3 and 5, it is clear that the addition of a small amount of Ni can naturally increase the adsorption capacity for Cr (VI). This is attributed to the high catalytic performance of Ni particles, which reduces the activation energy needed for the Cr (VI) reduction. The use of the micromixer chip also increases the reduction efficiency greatly as such a device can uniformly mix GO, Fe (0) and Ni. Sample 5 shows the highest

adsorption capacity, due to the combined effects of catalytic reaction and good mixing ability of the micromixer chip.

The pH is a key factor affecting Cr (VI) adsorption. In practice, wastewater has a pH ranging from 5 to 8. To reveal the pH affection on Cr (VI) adsorption, Cr (VI) adsorption experiment for sample 5 is tested at pH=5, 6 and 7. Results are shown in Figure 4-8 (c). Consisted with previous studies, lower pH is a benefit for Cr (VI) adsorption. A higher reaction rate and adsorption capacity are realized in lower pH.

The reusability and stability of samples are also investigated. The used samples are collected from the solution by filtration, dispersed in water and added excess $NaBH_4$ to reduce the Fe_2O_3 to zero-valent iron. Then, after filtration and drying, the Cr (VI) adsorption capacity for used samples under the same condition as new samples is analysed. Results are shown in Table 4-4. The low adsorption percentage and adsorption capacity indicated that the reused samples nearly totally lost Cr (VI) reduction ability. Because the Cr (III) hydroxide is absorbed by Fe-Ni/RGO after the first-time adsorption, and all possible reduction points have been occupied by Cr (III) hydroxide. After the second time reduced by $NaBH_4$, some Cr (III) hydroxide can still left and occupy the reaction points for Fe-Ni/RGO. On the other hand, during the second time reduction, RGO has possible to completely cover some Fe-Ni bimetal particles and prevent it react with Cr (VI), this will lead to the decrease of Cr (VI) adsorption capacity. Hence the samples cannot be reused easily but keep the possibility. Future research will carry out to improve the property of reusability.

Table 4-4 Sample reusability and stability for Cr (VI) adsorption

	Sample 2	Sample 3	Sample 4	Sample 5
Adsorption percentage for pH = 7.0				
New sample	46.07%	60.89%	61.33%	72.33%
Reused sample	2.78%	3.86%	3.32%	4.31%
After 9 months	45.85%	60.54%	61.25%	72.10%
Adsorption capacity (mg/g) for pH = 7.0				
New sample	95.83	126.65	127.56	150.45
Reused sample	5.79	8.02	6.91	8.96
After 9 months	95.36	125.92	127.39	149.97

To verification the stability of samples, let samples stand in the reaction solution for 9 months after the Cr (VI) adsorption experiment and then characterised the Cr (VI) concentration in solution. Results are shown in Table 4-4. The Cr (VI) adsorption percentage and adsorption capacity keeps stable after 9 months. This is due to that the generated Cr (III) hydroxide being absorbed by Fe-Ni/RGO is stable and difficult to disperse back to the solution.

Table 4-5 Cr (VI) adsorption capacity reported by literature

Raw material	pH	Adsorption capacity(mg/g)	References
Iron nanoparticles	5.0	47.2	[43]
Iron nanoparticles	6.0	62.4	[118]
Iron nanoparticles	5.5	66.7	[119]
Iron nanoparticles/RGO	4.25	162	[87]
Iron nanoparticles/RGO	5.0	180.64	[88]
Iron nanoparticles/RGO	7.0	21.72	[89]
Fe_2O_3/graphene	8	66.2	[90]
Fe-Ni/RGO	7.0	150.45	This work
Fe-Ni/RGO	6.0	176.74	This work
Fe-Ni/RGO	5.0	197.43	This work

Table 4-5 shows a comparison of the Cr (VI) adsorption capacity with iron nanoparticles based materials reported in the literature. As the initial concentration of Cr (VI), the ratio between Cr (VI) and reductant can vary in the literature. The best way to evaluate the material is adsorption capacity (mg/g) under similar pH. In practice, wastewater has a pH ranging from 5 to 8. Considering this fact, the proposed particles (sample 5) in our study present the highest adsorption capacity, benefiting from their extremely high BET surface area and uniform distribution of Ni and Fe (0) NPs on the RGO surface.

To reveal the Cr (VI) adsorption kinetics of sample 2-5, adsorption capacity is characterized with different times, shown in Figure 4-8 (d). The adsorption is initially fast because of lots of sites available at first, then the adsorption speed slows down with prolonging the time and reaches equilibrium after 72 hours.

The results are researched by pseudo-first-order kinetic model and pseudo-second-order kinetic model [120].

A linear form of the pseudo-first-order kinetic model is given as:

$$\log(q_e - q_t) = \log q_e - K_1 t \quad (4\text{-}1)$$

A linear form of the pseudo-second-order kinetic model is given as:

$$\frac{t}{q_t} = \frac{1}{K_2 q_e^2} + \frac{t}{q_e} \quad (4\text{-}2)$$

where q_e and q_t (mg/g) are the adsorption capacity of Cr (VI) at equilibrium and t time (hour). K_1 (g/mg/hour) and K_2 (g/mg/hour) are pseudo-first-order kinetic model and pseudo-second-order kinetic model rate constant respectively.

Table 4-6 Pseudo-first-order kinetic model and pseudo-second-order kinetic model results

	Sample 2	Sample 3	Sample 4	Sample 5
Pseudo-first-order kinetic model				
q_e (mg/g)	88.6785	117.3945	119.8971	144.8995
K_1 (g/mg/hour)	0.0640	0.1143	0.1956	0.3555
R^2-adjusted	0.9731	0.9591	0.9086	0.9559
Pseudo-second-order kinetic model				
q_e (mg/g)	100.9509	127.56231	127.30039	153.17131
K_2 (g/mg/hour)	0.0016	0.0026	0.0052	0.0084
R^2-adjusted	0.9923	0.9828	0.9790	0.9926

Table 4-6 shows the analysis results for the pseudo-first-order kinetic model and pseudo-second-order kinetic model. Compared with the pseudo-first-order kinetic model, the pseudo-second-order kinetic model got adjusted R^2 closer to 1, which means that the pseudo-second-order kinetic model is more suitable for the samples. This confirmed that the adsorption process is more rely on chemical adsorption.

4.2.4 Cr (VI) Reduce Reaction Mechanism and kinetic model

The large capacity of the new materials can be attributed to several reasons. First, the RGO is synthesized by GO reduction method, and it is unavoidable that there is a small amount of oxygen-containing functional group left on RGO. The oxygen-containing functional group can provide anchor points for Fe (0) and Ni NPs and limit the excessive growth of the NPs [121], which thereby increase the dispersion and stability of Fe (0) and Ni. Secondly, the located Fe (0) and Ni NPs can prevent the aggregation of RGO via the increase of the surface spacing of RGO. Thirdly, RGO has an extremely high specific surface area and a strong adsorption capacity for Cr (VI). Once Cr (VI) is adsorbed on the RGO surface, the nanoscale zero-valent iron will transport electrons to Cr (VI) to reduce it to Cr (III). For Ni-Fe bimetal, nickel powder acts as a catalyzer for the redox reaction between ZVI and Cr (VI).

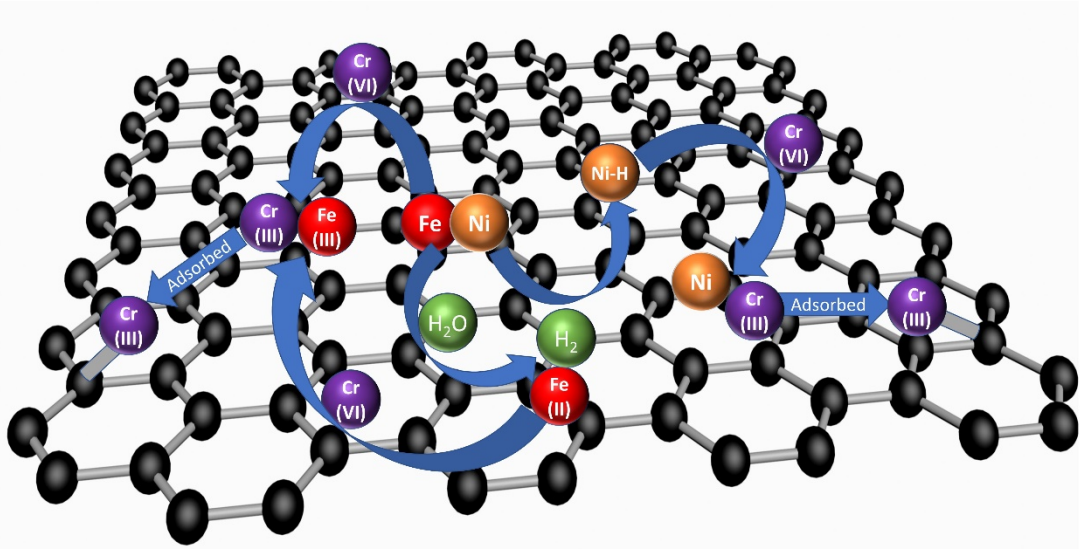

Figure 4-9 Cr (VI) adsorption and reduction mechanism of samples with RGO.

Schematically, the process is illustrated in Figure 4-9. The main reaction route for iron nanoparticles reducing Cr (VI) is the electron transfer from Fe^0($E^0_{Fe^{2+}/Fe^0} = -0.44\ V$) to Cr (VI)($E^0_{HCrO_4^-/Cr^{3+}} = 1.36\ V$) [122]:

$$2HCrO_4^- + 14H^+ + 3Fe^0(s) \rightarrow 2Cr^{3+} + 8H_2O + 3Fe^{2+} \qquad (4\text{-}3)$$

As $E^0_{Fe^{3+}/Fe^{2+}} = 0.77\ V < E^0_{HCrO_4^-/Cr^{3+}}$, the generated Fe^{2+} will also react with Cr (VI) [123]:

$$HCrO_4^- + 7H^+ + 3Fe^{2+} \rightarrow Cr(III) + 4H_2O + 3Fe^{3+} \qquad (4\text{-}4)$$

The electrons also transfer from Fe^0 to Fe^{3+}:

$$Fe^0 + 2Fe^{3+} \rightarrow 3Fe^{2+} \qquad (4\text{-}5)$$

After adding Ni, due to the catalytic action, the reaction activity of Fe^0 will be much higher than that without Ni [62, 124]. The reaction mechanism is shown below:

$$Fe^0 + 2H_2O \rightarrow Fe^{2+} + H_2 + 2OH^- \quad (4\text{-}6)$$

$$2Ni^0 + H_2 \rightarrow 2Ni^0 - H \cdot \quad (4\text{-}7)$$

$$HCrO_4^- + 3Ni^0 - H \cdot + 4H^+ \rightarrow Cr(III) + 4H_2O + 3Ni^0 \quad (4\text{-}8)$$

At this stage, XPS results indicate that the Cr (III) will form insoluble Cr (III) hydroxide and be absorbed by Fe-Ni/RGO. The absorption is stable and Cr (III) will not be dissolved back in the solution for a long time. The absorbed Cr (III) hydroxide will occupy some surface area of Fe-Ni/RGO and lead a decrease of reaction rate. Meanwhile, the Cr (III) hydroxide could cover up some unreacted zero-valent iron to reduce the final adsorption capacity.

At low pH, the major Cr (VI) status is $HCrO_4^-$ and $Cr_2O_7^{2-}$.[38] The higher removal efficiency at low pH is attributed to that the surface of the adsorbent becomes highly protonated and positively charged. The adsorbent can attract $HCrO_4^-$ and $Cr_2O_7^{2-}$ via electrostatic force. With the increase of pH, less H^+ and more OH^- hugely effected the reaction rate and equilibrium. Also, the adsorbent's surface will be negatively charged, which then highly decreases the adsorption capacity.

As the Cr (VI) adsorption is not pure chemical or physical reaction, traditional pseudo-first-order kinetic model and pseudo-second-order kinetic can not fit it well enough, a new equation is needed for Cr (VI) adsorption.

The following results are considered:

All electrons are moved initially from Fe species and finally got by Cr species; it can be considered as Fe is the only element capable of reducing Cr (VI)

The equation rate for the Cr (VI) reduction is based on the concentration of Cr (VI) and samples.

The conversion ratio between Cr (VI) and Cr (III) is 1:1.

Considering the reaction mechanism mentioned above, a kinetic model is proposed to describe the Cr (VI) removal, When the pH and temperature are constant the rate of Cr (VI) reduction by samples can be found as:

$$\frac{d[Cr(VI)]}{dt} = -k[SC]_t[Cr(VI)] \quad (4\text{-}9)$$

Where [Cr (VI)] is the hexavalent chromium concentration (mmol/L) at time *t* and *k* its rate coefficient (L mmol^{-1} h^{-1}), [SC] represents the equivalent sample concentration at time t capable of reducing Cr (VI) (mmol L^{-1}).

Considering that Fe^0 is oxidised during Cr (VI) reduction, the equivalent sample concentration on the surface of the samples decreases during the reaction and can be calculated as:

$$[SC]_t = C_{SC}^*[S](1 - \frac{[Cr(VI)]_0 - [Cr(VI)]_t}{C_{SC}^*[S]}) \quad (4\text{-}10)$$

where C_{SC}^* is the removal compacity of Cr (VI) per unit gram of sample (mmol/g), which is obtained by the adsorption capacity analysis experiment. [*S*] is the sample concentration (g/L), $C_{SC}^*[S]$, represents the initial concentration of [SC]. $[Cr(VI)]_0$ is the initial hexavalent chromium concentration (mmol/L). $\frac{[Cr(VI)]_0 - [Cr(VI)]_t}{C_{SC}^*[S]}$ represents the fraction of [SC] oxidised.

Integrate the above equations, results in:

$$[Cr(VI)]_t = \frac{[Cr(VI)]_0\{C_{SC}^*[S] - [Cr(VI)]_0\}}{C_{SC}^*[S]exp\{k(C_{SC}^*[S] - [Cr(VI)]_0 t)\} - [Cr(VI)]_0} \quad (4\text{-}11)$$

where *k* and C_{SC}^{*} are the model constant parameters and *t* is the reaction time (hour). The fitting result of the kinetic model is shown below:

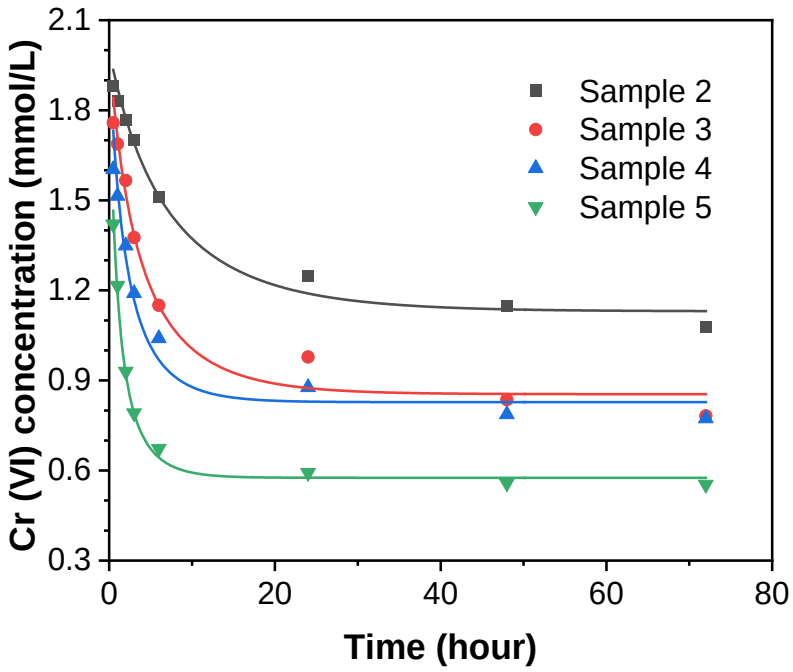

Figure 4-10 The kinetic model curve for sample 2-5

Table 4-7 The kinetic model results

	Sample 2	Sample 3	Sample 4	Sample 5
K (L mmol^{-1} h^{-1})	0.0798	0.1563	0.2807	0.5549
C_{SC}^{*} (mmol/g)	1.7392	2.2914	2.3445	2.8483
R^2-adjusted	0.9822	0.9710	0.9507	0.9928

The results show the kinetic model has high adjusted R^2, which confirmed the reaction mechanism and model are reasonable for the reduction reaction. By comparing the rate coefficient k between sample 2,4 and sample 3,5, it indicated the added Ni nearly doubled the rate coefficient for both with and without microchip samples, that is due to the catalyst effect of Ni. Also, from

the model results, it indicated after microchip mixture and dispersion, the rate coefficient k can get hugely increase. Combine with the above morphology analyses, that is because microchip gives the sample more contact area among Fe, Ni and Cr (VI).

4.3 Chapter summary

In this Chapter, a series of novel Ni-Fe/RGO composites were constructed for effective removal of Cr (VI) in aqueous solution, where RGO acts as adsorbent, Ni as the catalysis and Fe (0) as the reducing agent. They are brought together by co-precipitation and physical adsorption. Intensifying the mixing through a microchip leads to an improved dispersion and further enhanced Cr (VI) adsorption capacity.

The added Ni nearly doubled the BET surface area compared with samples without Ni. This is due to the high BET surface area of nano Ni and its combination with Fe (0) NPs reduces the possible aggregation of Fe (0) NPs. The Cr (VI) adsorption capacity and rate coefficient are enhanced with the catalyzation of Ni and higher BET surface area.

The Ni-Fe/RGO composite exhibits the highest Cr (VI) adsorption capacity of 150.45 mg/g at pH=7 and 197.43 mg/g at pH=5.

The added nickel has a higher reduction potential than Fe, through anode through electrochemical coupling, it enhanced the reduction activity of iron nanoparticles, and reduced the loss of iron nanoparticles due to oxidation by the surrounding environmental medium. Dispersants added during the synthesis process and the spatial site resistance effect of RGO promotes the dispersion of Fe (0) and Ni (0) NPs and prevents their aggregation.

Meanwhile, the loaded Fe (0) and Ni NPs also prevent the aggregation of RGO due to the increased surface spacing of RGO. The synergistic effects enable the sample with a high BET surface area and Cr (VI) adsorption capacity. The adsorption process fits the Pseudo-second-order kinetic model.

The microchip presents a better dispersal ability of GO in solution than traditional magnetic stirring and thereby could avoid the agglomeration of GO. Samples are demonstrated with enough points to load Fe-Ni bimetal, resulting in much higher Cr (VI) adsorption capacity and rate coefficient.

Meanwhile, the materials are synthesized by a convenient and cheap method without nitrogen protection compared with other reports

Chapter 5

Ni-Fe/MWCNTs composites for Hexavalent Chromium Reduction in Aqueous Environment

While Fe-Ni/RGO has a high Cr (VI) adsorption capacity, its cost makes it unsuitable for industrial applications. In the meantime, it cannot be reused. A study is currently being conducted on Fe-Ni/MWCNTs in order to address these issues. A MWCNT has a much higher surface area than RGO and is significantly less expensive. As a result of RGO's second time reduction, a large number of Fe-Ni particles are encased, which prevents their reuse. As MWCNTs possess a distinctive tube shape, Fe-Ni bimetal particles are difficult to wrap around MWCNTs, allowing Fe-Ni/MWCNTs to be sufficiently reusable.

5.1 Preparation of Fe/MWCNTs, and Fe-Ni/MWCNTs Composites

60 wt% $FeCl_3$ solution is prepared by add a certain amount of $FeCl_3$ into deionized water and stir well. Firstly 0.32 g MWCNTs and 2.0 g PVP were added into 50ml deionized water. After 30 minutes magnetic stirring, a certain amount of 60 wt% FeCl3 solution and $NiCl_2 \cdot 6H_2O$ were added and magnetic stirred overnight. In different samples, Fe-Ni ratios are adjusted, but the total mass of Fe (0) and Ni remains the same at 0.2 grams.

Afterwards, 40 mL of 50 mg/mL $NaBH_4$ is added dropwise to the system and stirred overnight. As a reducing agent, $NaBH_4$ reduced Fe (III) and nickel (II) to Fe (0) NPs and Ni (0) NPs, respectively. It is during this period that mechanical oscillation replaces magnetic stirring in order to prevent Fe (0)

NPs from being affected by the magnetic field. The production of H_2 during this step requires careful control. Here are the reaction equations:

$$Fe(H_2O)_6^{3+} + 3BH_4^- + 3H_2O = Fe^0 \downarrow + 3B(OH)_3 + 10.5H_2 \uparrow$$

$$Ni(H_2O)_6^{3+} + 3BH_4^- + 3H_2O = Ni^0 \downarrow + 3B(OH)_3 + 10.5H_2 \uparrow$$

Following vacuum filtration, the final product is washed three times with ethanol, dried overnight in a vacuum oven, and then collected and stored with nitrogen protection. The whole preparation process is shown in Figure 5-1.

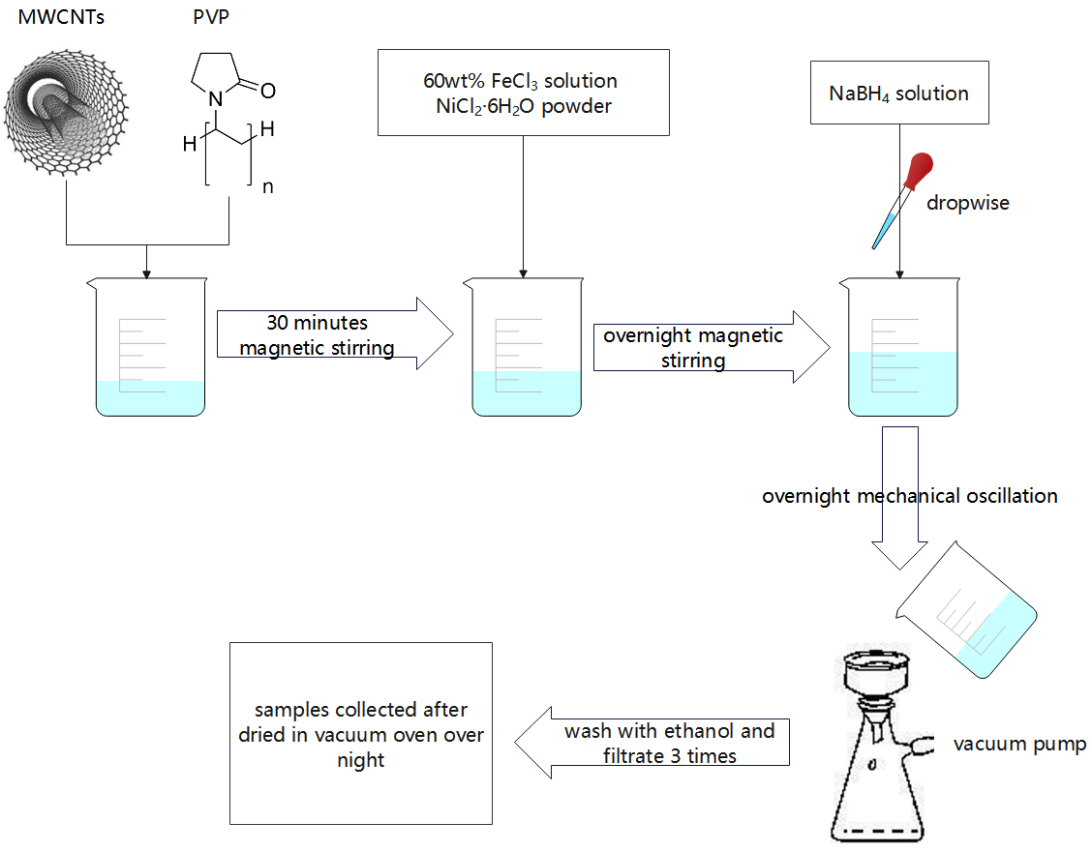

Figure 5-1 Schematic illustration of the preparation process of Fe-Ni/MWCNTs composite

After the Cr (VI) adsorption capacity experiment, the sediment should be collected by vacuum filtration. The collected sediment is named as M3A. In order to obtain M3R, disperse half of the M3A in 25 ml DI water containing 1.0

g PVP and under mechanical oscillation overnight. Then dropwise exceed $NaBH_4$ solution with mechanical oscillation. The sediment was collected by vacuum filtration, washed with ethanol three times, and dried in vacuum oven overnight. The collected sediment is named as M3R.

For the purpose of comparison, seven samples are prepared as shown in Table 5-1.

Table 5-1 Detailed reaction conditions of different samples

Sample	60 wt% $FeCl_3$ solution	MWCNTs	NiCl2·6H2O	PVP	$NaBH_4$	Fe: Ni (weight)
M1	1.033ml	0.32 g	\	2 g	2 g	\
M2	1.278ml	0.32 g	0.534 g	2 g	2 g	2:1
M3	1.606ml	0.32 g	0.268 g	2 g	2 g	5:1
M4	1.760ml	0.32 g	0.156 g	2 g	2 g	10:1
M5	0.968ml	0.32 g	0.808 g	2 g	2 g	1:1
M6	1.839ml	0.32 g	0.078 g	2 g	2 g	20:1
M7	1.452ml	0.32 g	0.404 g	2 g	2 g	3:1

5.2 Results and Discussion

5.2.1 Particle Size, Morphology and Elemental Analyses

Particle size analysis

A centrifuge is used to separate the sediments from the liquid after adding 15 mg of the sample solution to 50 mL deionized water under ultrasonic dispersion. It is tested by Zetasizer, Malvern, for the upper liquid. Figure 5-2 and Table 5-2 illustrate the results. There are two peaks in all samples. A larger size range indicates that MWCNTs have been stacked in an unordered manner. As can be seen from the purchase company data, it is clearly shorter than the length of MWCNTs (2500 nm). MWCNTs are curved rather than straight, which explains this phenomenon. According to the TEM results, Ni and Fe (0) NPs about 50-80 nm in diameter are present in the smaller size range.

Peak 2 has a smaller diameter than M3 for M3A. This is due to Fe (0) being consumed by Cr (VI) during the reduction process of Cr (VI). In addition, peak 2 intensity for M3A increased from 6.9% for M3 to 20.9%. This is indicative of Fe-Ni bimetal falling off the surface of MWCNTs following Cr (VI) reduction. As can be seen from Table 5-2, peak 2 for M3R is larger than peak 2 for M3 and M3A. As a result, Fe-Ni nanoparticles agglomerate during the second reduction of Fe-Ni/MWCNTs. It is anticipated that the agglomeration of Fe-Ni nano will negatively affect the adsorption capacity of Cr (VI). The intensity of peak 2 for M3R decreased from 20.9% to 16.9%, indicating that part of the Fe-Ni bimetal that was lost in M3A decorated back on the surface of MWCNTs

during the second reduction of Fe-Ni/MWCNTs. The reusability of samples can be enhanced by this method.

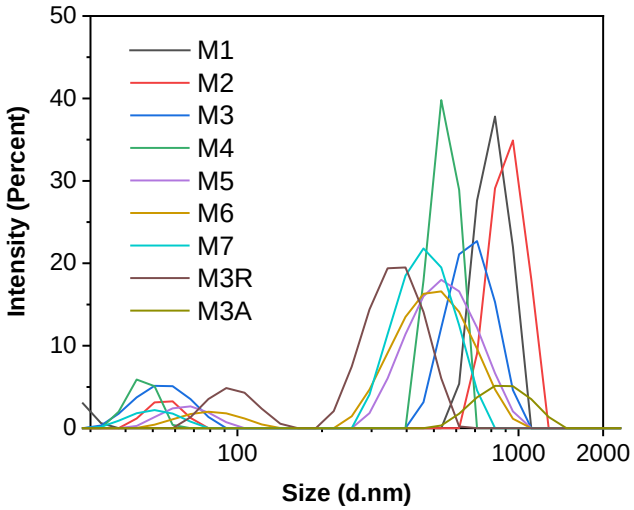

Figure 5-2 Particle size distribution measured by DLS

Table 5-2 Size distribution determined by the intensity

	Peak 1		Peak 2	
	Size (d.nm)	% intensity	Size (d.nm)	% intensity
M1	515.5	91.3	81.30	8.7
M2	555.0	90.7	66.46	9.3
M3	461.5	93.1	64.91	6.9
M4	544.2	86.6	46.01	13.4
M5	261.5	92.6	51.31	7.4
M6	919.7	91.2	55.24	8.8
M7	473.6	92.3	50.96	7.7
M3R	370.0	83.1	96.46	16.9

M3A	684.3	79.1	54.85	20.9

In Table 5-2, M2-7 has a relatively smaller peak 2 compared to M1. This means that the FeNi bimetallic particles have a lower degree of aggregation compared to the monometallic iron nanoparticles. This has a positive effect on the final Cr (VI) removal capacity.

Morphology and Elemental Analyses

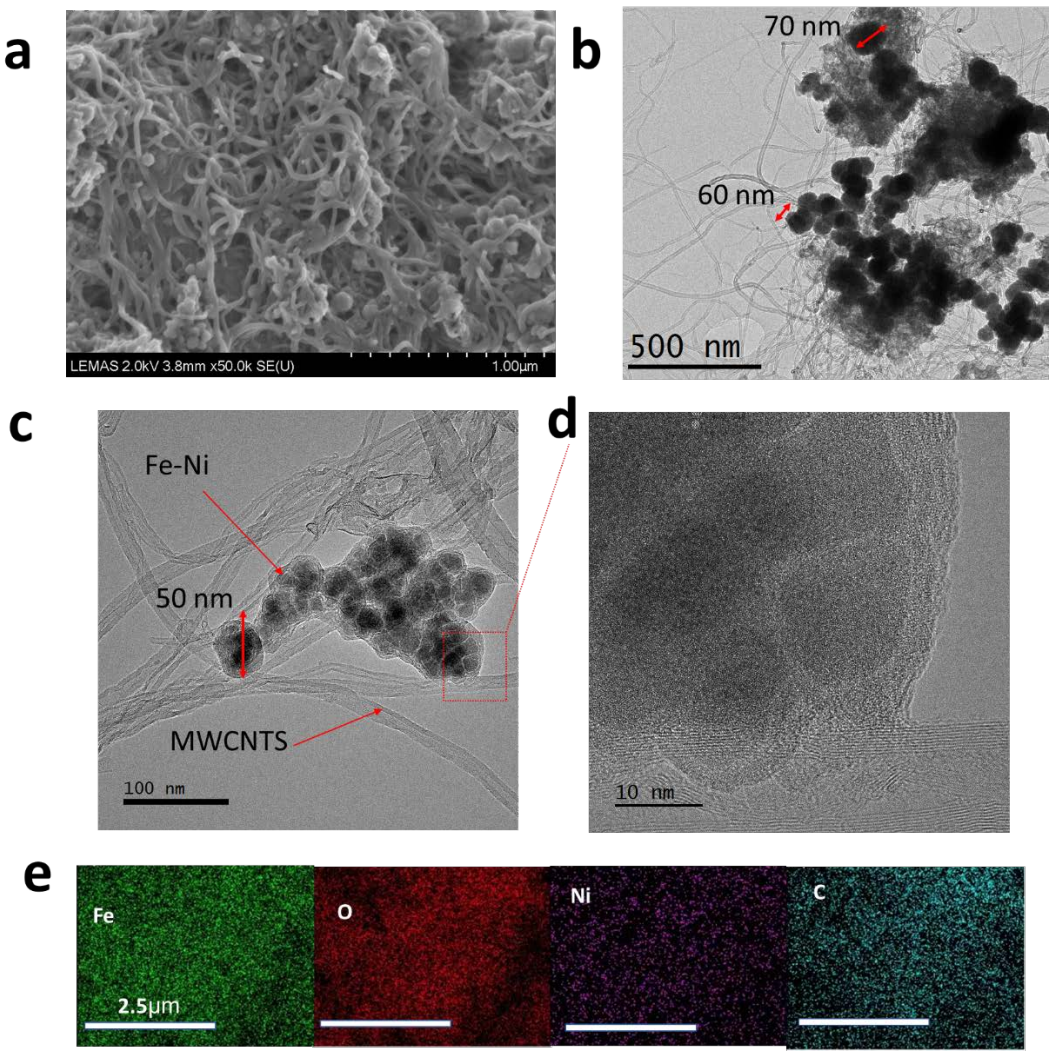

Figure 5-3 (a) SEM image and (b) TEM image for M3, (c) TEM image and (d) HRTEM image for M3A. (e) EDS image for M3.

TEM and SEM were used to examine the morphology and structure of the Fe/MWCNTs. Figure 5-3 (a) illustrates M3 as an unordered stacking of MWCNTs and Fe-Ni particles. The diameter of Fe-Ni particles is approximately 50-80 nm, which is consistent with the DLS result. MWCNTs have a length greater than 1μm.

In Figure 5-3 (b), most of the diameter of Fe-Ni bimetal is between 60 nm and 70 nm, which is in good agreement with the results for DLS in Table 5-2.

Compared to Figure 5-3 (b) and (c), the diameter of Fe-Ni particles decreased from 60-70 nm to around 50 nm after the Cr (VI) adsorption test. This is because part of the Fe (0) is consumed by Cr (VI) during the reduction process. This is also confirmed by the results of DLS. Figure 5-3 (d) illustrates how Fe-Ni bimetal is decorated on the surface of MWCNTs in the HRTEM image for M3A.

Figure 5-3 (e) illustrates the use of energy-dispersive X-ray spectroscopy (EDS) to analyse the elemental composition of the sample. It is observed that Fe, Ni, and C are distributed uniformly. It is inevitable that metallic particles can be partially oxidised because nitrogen protection is not used throughout the whole synthesis process.

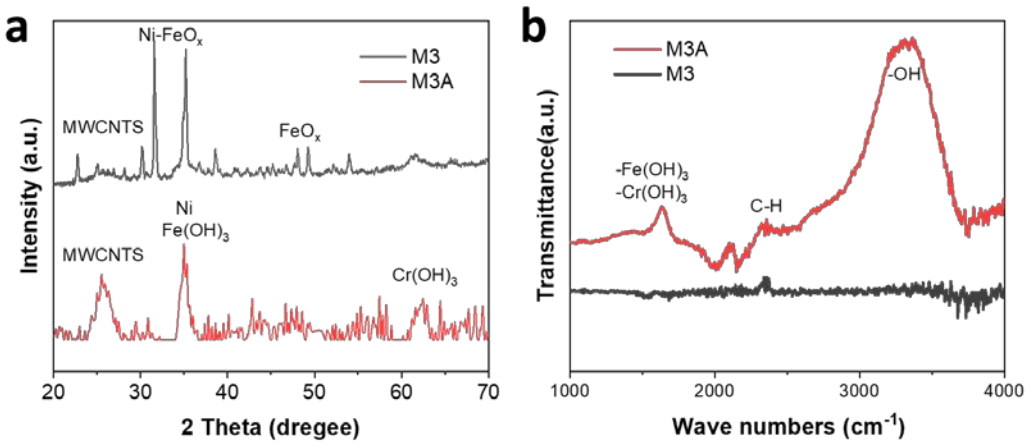

Figure 5-4 (a) XRD patterns of M3 and M3A and (b) FTIR spectra of sample M1, M3 and M3A

Figure 5-4 (a) illustrates the XRD patterns of M3 and M3A. M3 and M3A exhibit a diffraction peak at 25.1°, which corresponds to the typical (002) diffraction of MWCNTs [125]. M3 exhibits a double peak at 31.6°, 35.2° and 48.1°, 49.2° caused by the inevitable oxidation of Fe (0) [126]. The peak at 35.1° for M3A

indicates the presence of $Fe(OH)_3$ [127]. The peak at 62.9° indicates the presence of Cr $(OH)_3$ [128].

The FTIR spectra of samples M3 and M3A are shown in Figure 5-4 (b). A distinct peak at around 1623 cm^{-1} belongs to the coprecipitated sediment of Cr $(OH)_3$ and Fe $(OH)_3$, which corresponds to coordinated or adsorbed H_2O in M3A [129]. This confirmed the sediment contains Cr (III) and Fe (III) in the form of Cr $(OH)_3$ and Fe $(OH)_3$. The distinct peak at around 3363 cm^{-1} represents the stretching and bending vibration of the -OH on MWCNTs in M3A [130]. The -OH should be generated through the Cr (VI) adsorption. Due to the adsorption of Cr (VI), -OH should be generated as a result of Cr (VI)'s strong oxidizing ability. Furthermore, the minor peak at around 2350 cm^{-1} for all samples is attributed to the C-H stretching in carbon nanotubes [131]. As a result of the synthesis of MWCNTs, there should be residual C–H. The fact that there is no other obvious peak for M3 indicates that most of the oxygen-containing groups are reduced by $NaBH_4$ during sample synthesis.

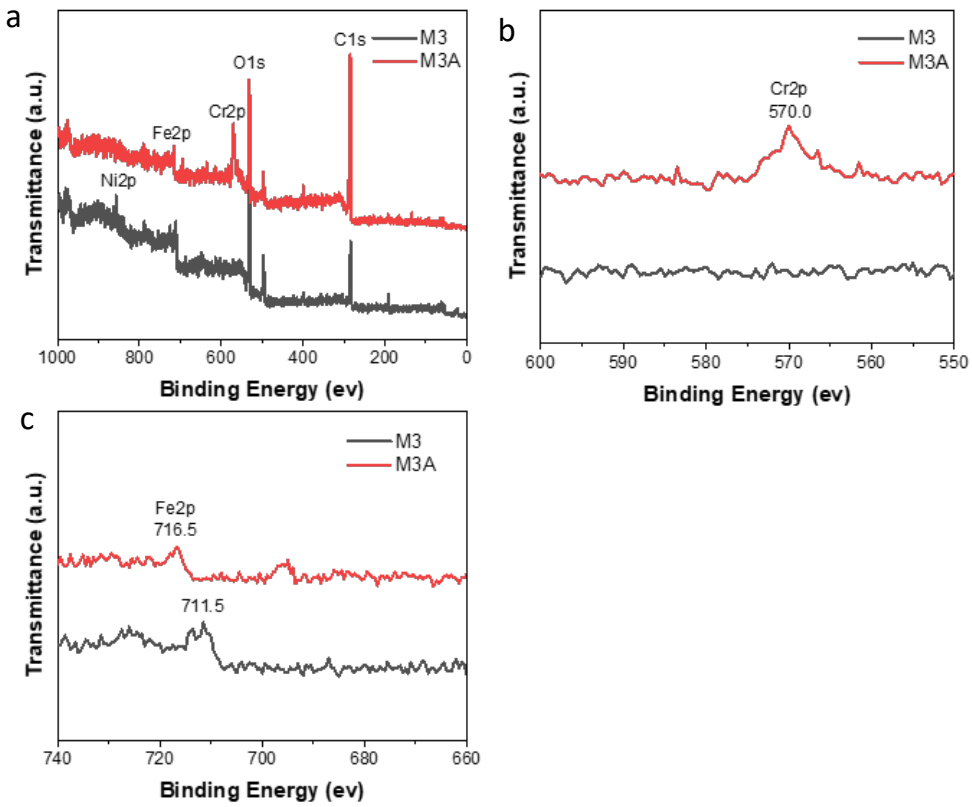

Figure 5-5 XPS spectra of M3 and M3A: (a) wide scan, (b) high resolution spectra of Cr and (c) high resolution spectra of Fe

Figure 5-5 (a) shows the XPS spectra of M3 and M3A. Samples are primarily composed of C, O, Fe, and Ni. As shown in Figure 5-5 (b), after Cr (VI) adsorption experiment, a new peak appears around 570.0 eV along with those for Cr. The pick represents Cr that is present with Cr (III) hydroxide [132]. XRD results confirmed that Cr (VI) is reduced to Cr (III) and adsorbed by the sample. Before Cr (VI) adsorption, on Figure 5-5 (c), Fe's peak is around 716.5 eV, which indicates that Fe exists as a zero-valent metal [133]. Following Cr (VI) adsorption, the pick left moved to around 711.5 eV, which belongs to Fe (III) [134]. Results from XPS are consistent with those obtained from XRD.

5.2.2 BET Surface Area Study

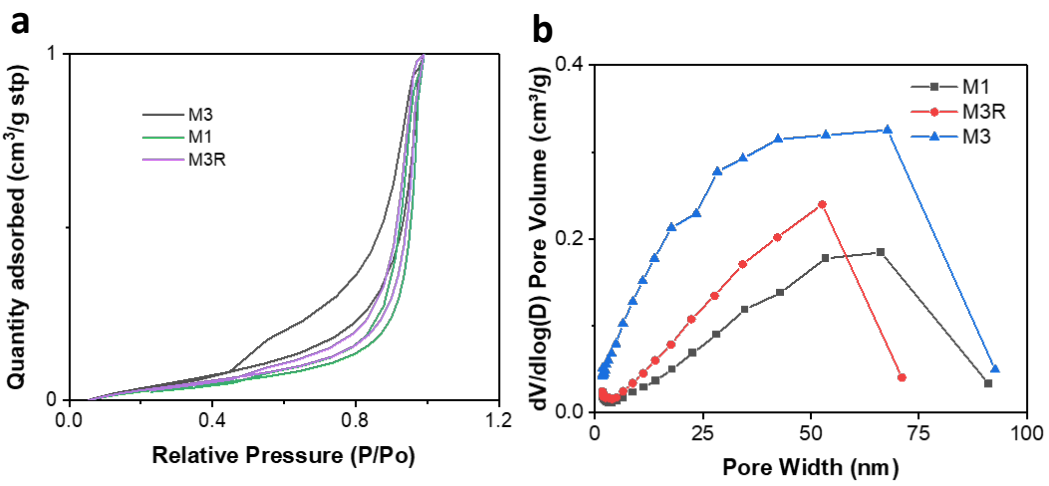

Figure 5-6 BET results of samples (a) N2 adsorption isotherms; (b) pore size distribution data.

Micromeritics Tristar 3000 is used to determine the specific surface area of all samples. The results are shown in Figure 5-6. According to the adsorption-desorption isotherm, all samples exhibit multilayer adsorption characteristics [135]. There is a stronger interaction between the molecules of the adsorbate than between the molecules of the adsorbent and the adsorbate. The adsorption process appears to self-accelerate as it proceeds [136]. M1, M3 and M3R have specific surface areas calculated as 23.6197 m^2/g, 82.2434 m^2/g and 30.7797 m^2/g, respectively.

When comparing M1 and M3, the presence of nickel powder has a significant impact on their surface area. The nickel powder increases the composite's BET surface area due to its own high surface area and combines with Fe(0) to reduce the likelihood of Fe aggregation. In contrast, samples that contain nickel powder have a smaller distribution of pore widths. A comparison of M3

and M3R. As a result of the aggregation of Ni (0) and Fe (0) during the Cr (VI) adsorption experiment and the second time reduction process for Fe (III), the BET surface area decreased distinctly. The result is consistent with DLS results. It should be noted, however, that the BET specific surface areas of all samples are considerably lower than those of pure MWCNTs (more than 200 m^2/g). This is due to the disordered stacking of MWCNT, which is consistent with the SEM results. After these samples were ultrasonically dispersed in water, a different situation occurred, as the unordered stacked MWCNTs will be dispersed in some degree in order to provide a greater amount of surface area for absorption of Cr (VI).

5.2.3 Cr (VI) Adsorption Capacity Analyses

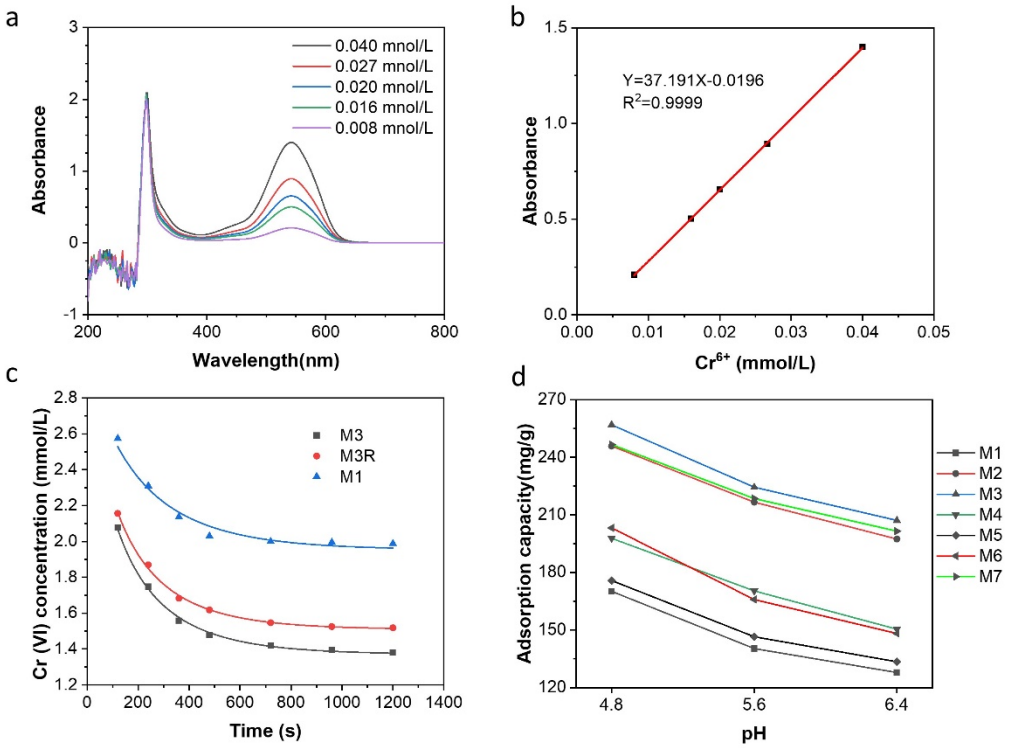

Figure 5-7 (a) UV-vis spectra of solutions of Cr (VI) reaction with DPC; (b) calibration curve line of Cr (VI) concentration (λ=545 nm); (c) Cr (VI) adsorption capacity at different pH; (c) Cr (VI) adsorption capacity with time and pseudo-second-order kinetic model; (d) Cr (VI) adsorption capacity at different pH;

The Figure 5-7 (a) and (b) illustrate the DPC method used to measure Cr (VI) concentration in 2.3.3. When DPC reacts with Cr (VI) ions in an acid medium, a violet solution is formed, at λ_{max} =545 nm, which exhibits a characteristic peak. For Cr (VI) concentration, Figure 5-7 (b) illustrates a linear relationship. In other words, y = 37.191x - 0.0916 with R^2 = 0.9999, where y represents absorption and x represents Cr (VI) concentration.

Using phosphoric acid (H_3PO_4) solution, pH buffers for pH values 4.8, 5.6, and 6.2 are prepared and pH is adjusted by dropwise addition of sodium hydroxide solution (NaOH). An amount of 15 mg of each sample is added to 34 mL of

pH buffer (pH=5.6), followed by ultrasonic dispersion to ensure that the sample is fully dispersed. Afterwards, 6 mL of 20 mmol/L Cr (VI) solution was added to the solution in order to make the total solution 3 mmol/L Cr (VI). The solution should be oscillated mechanically. Each time at the scheduled time, 0.5 ml of solution is drawn and added to a bottle containing 2 ml of DPC solution and 22.5 ml of water. A UV absorption spectrum is measured after 5 minutes in order to determine the amount of Cr (VI) remaining in the solution. The absorption became stable after 20 minutes in most cases (Table 5-3). Initially, all Cr species are in hexavalent form, and the adsorption capacity can be calculated by analysing the remaining concentration of Cr (VI).

Table 5-3 The Cr (VI) concentration of samples deduced for 20 minutes.

	pH	Adsorption percentage	Adsorption capacity (mg/g)	Fe: Ni (weight)
Iron nanoparticles	5.6	5.42%	22.56	\
MWCNTs	5.6	4.80%	19.95	\
M1	5.6	32.35%	134.57	\
M2	5.6	52.07%	216.60	2:1
M3	5.6	53.95%	224.43	5:1
M4	5.6	40.95%	170.37	10:1
M5	5.6	35.22%	146.50	1:1
M6	5.6	39.88%	165.89	20:1
M7	5.6	52.52%	218.46	3:1
M3R	5.6	49.38%	205.41	5:1

Likewise, pure MWCNTs and iron nanoparticles are also tested under the same conditions for Cr (VI) adsorption capacity analyses. As shown in Table 5-3, pure MWCNTs and iron have very low Cr (VI) adsorption capacities.

Fe (0) decorated on MWCNTs has a significantly higher adsorption capacity than pure MWCNTs and iron nanoparticles. The combined action of MWCNTs and iron nanoparticles is responsible for this result. As a result of the high specific surface area of MWCNTs, as Cr (VI) is adsorbed to the surface of MWCNTs, it can be more effectively reduced by the decorated nano iron

located close to the surface. Comparing M1 with other samples, it is clear that the addition of a certain amount of Ni can naturally increase Cr (VI) adsorption capacity. Due to the high catalytic performance of Ni particles, the activation energy required for the reduction of Cr (VI) is reduced. The adsorption capacity of M4,5,6 is lower than that of M2,3,7. This is due to an unsuitable Fe-Ni ratio. As a result of Ni occupying too much of M5, Fe (0) is unable to reduce Cr (VI) to Cr (III). In the case of M4,6. Ni is insufficient to serve as an effective catalyst. According to Table 5-3, the ideal ratio for Fe-Ni is approximately 5:1. Because of the best Fe-Ni ratio in the catalytic reaction, M5 exhibits the highest adsorption capacity.

The reusability of samples is also examined. To reduce Fe_2O_3 to zero-valent iron, the used samples are filtered from the solution, dispersed in water, and added excess NaBH4. Following filtration and drying, the adsorption capacity of Cr (VI) for used samples is determined under the same conditions as for new samples. The results are presented in Table 5-3. After one reuse of M3R, the adsorption capacity decreased to 205.41 mg/g, as opposed to 91% the first time. Due to the agglomeration of Fe-Ni nanoparticles during the second reduction of Fe-Ni/MWCNTs, the adsorption capacity is reduced. As a result of the agglomeration, the BET surface of Fe-Ni bimetal will decrease, as well as the reaction point for Fe(0) and Cr (VI). As a result of the experiment, it appears that these samples can be reused to a certain extent.

The pH of the solution plays an important role in Cr (VI) adsorption. In practice, wastewater has a pH range of 5 to 8. In order to determine how pH affects Cr (VI) adsorption, Cr (VI) adsorption experiments were conducted at pH = 4.8, 5.6, and 6.4. The results are presented in Table 5-4, which are in consistent

with previous research [137], As pH increases, the Cr (VI) adsorption capacity decreases. The highest adsorption capacity is observed for M3 at pH = 4.8 for 256.87 mg/g.

Table 5-4 pH Affection on Cr (VI) adsorption

	Adsorption percentage			Adsorption capacity (mg/g)		
	pH = 5.6	pH = 4.8	pH = 6.4	pH = 5.6	pH = 4.8	pH = 6.4
M1	32.35%	38.00%	29.38%	134.57	158.06	122.24
M2	52.07%	59.10%	47.45%	216.60	245.87	197.40
M3	53.95%	61.75%	49.78%	224.43	256.87	207.09
M4	40.95%	47.54%	36.16%	170.37	197.77	150.42
M5	35.22%	42.25%	32.08%	146.50	175.77	133.45
M6	39.88%	48.84%	35.62%	165.89	203.18	148.18
M7	52.52%	59.28%	48.44%	218.46	246.61	201.50

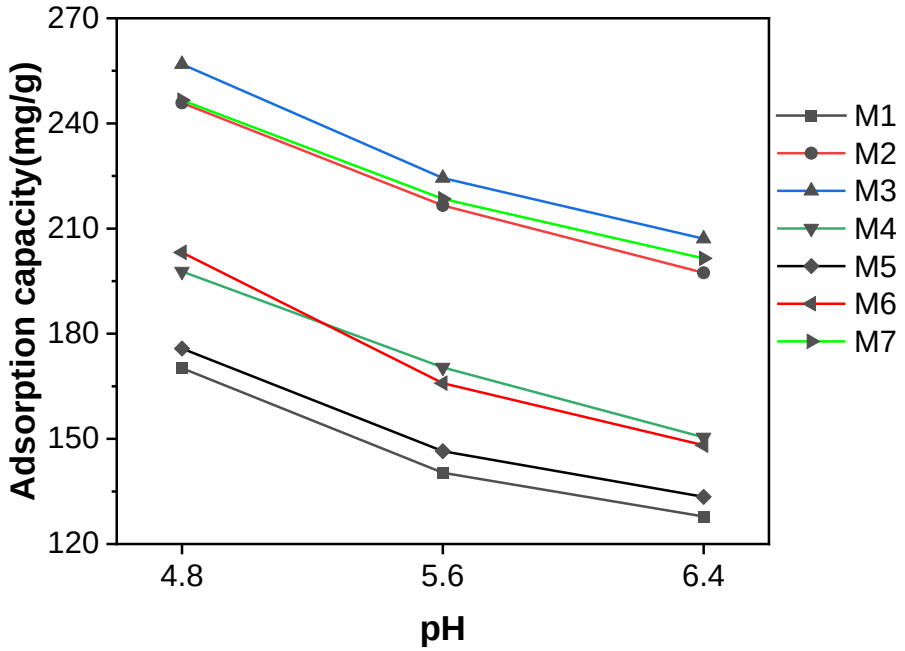

Figure 5-8 pH Affection on Cr (VI) adsorption

To verify the stability of samples, let samples stand in the reaction solution for two months after the Cr (VI) adsorption experiment, and then characterize the Cr (VI) concentration in solution. The results are presented in Table 5-5. The Cr (VI) adsorption percentage and adsorption capacity remain stable after three months. After three months, most samples retain more than 95% of their adsorption capacity. The reason for this is that the Cr (III) hydroxide produced is stable and difficult to disperse back into the solution once it has been absorbed by Fe-Ni/MWCNTs.

Table 5-5 Sample stability for Cr (VI) adsorption

	pH	Adsorption percentage	Adsorption capacity (mg/g)	After 3 Months	Adsorption Capacity left
M1	5.6	32.35%	134.57	131.03	97.37%
M2	5.6	52.07%	216.60	205.97	95.09%
M3	5.6	53.95%	224.43	217.16	96.76%
M4	5.6	40.95%	170.37	164.59	96.61%
M5	5.6	35.22%	146.50	141.84	96.82%
M6	5.6	39.88%	165.89	155.83	93.93%
M7	5.6	52.52%	218.46	212.68	97.35%

A comparison of Cr (VI) adsorption capacity with MWCNTs or CNTs related materials is shown in Table 5-6. In literature, the ratio between Cr (VI) and reductant varies according to the initial concentration of Cr (VI). As discussed previously, higher pH has a negative impact on adsorption capacity, and the best way to evaluate the material is to determine its adsorption capacity (mg/g) under similar pH conditions. Compared to the list literature, this study demonstrated a significantly higher adsorption capacity for Cr (VI) even at negative pH levels. Under similar conditions, Fe-Ni/MWCNTs had a 20% higher Cr (VI) adsorption capacity than Fe-Ni/RGO.

Table 5-6 Cr (VI) adsorption capacity reported by literature

Raw material	pH	Adsorption capacity(mg/g)	References
CNTs supported by activated carbon	2.0	9.0	[93]
ionic liquid functionalized oxidised MWCNTs	2.8	85.83	[94]
MWCNTs-COOH-immobilized HSO4	2.0	31.29	[95]
Magnetic iron oxide MWCNTs	3.0	12.61	[96]
$FeMnO_x$ decorated MWCNTs	2.0	47.25	[97]
α- Fe2O3/MWCNTs	6.0	Around 75	[98]
ZnO-Functionalized MWCNTs	2.0	Up to 140	[99]
Fe-Ni/RGO	6.0	176.74	This work
Fe-Ni/RGO	5.0	197.43	This work
Fe-Ni/MWCNTs	4.8	256.87	This work
Fe-Ni/MWCNTs	5.6	224.43	This work
Fe-Ni/MWCNTs	6.4	207.09	This work

The adsorption kinetics of Cr (VI) are determined by determining the adsorption capacity of samples at different times, as shown in Figure 5-7 (c). Initially, adsorption is rapid due to the enormous number of available sites, but

it slows down with the passage of time and reaches equilibrium after 20 minutes.

The results are analysed using pseudo-first-order kinetic models and pseudo-second-order kinetic models.

This pseudo-first-order kinetic model can be expressed linearly as follows:

$$\log(q_e - q_t) = \log q_e - K_1 t$$

The pseudo-second-order kinetic model can be expressed in linear form as follows:

$$\frac{t}{q_t} = \frac{1}{K_2 q_e^2} + \frac{t}{q_e}$$

where q_e and q_t (mg/g) represent Cr (VI) adsorption capacity at equilibrium and t time (hour). K_1 (g/mg/min) and K_2 (g/mg/min) represent pseudo-first-order kinetic model and pseudo-second-order kinetic model rate constant respectively.

Table 5-7 Pseudo-first-order kinetic model and pseudo-second-order kinetic model results

	M1	M3	M3R
Pseudo-first-order kinetic model			
q_e (mg/g)	149.9628	221.5793	203.0504
K_1 (g/mg/min)	0.1252	0.1755	0.1719
R^2-adjusted	0.9860	0.9904	0.9855
Pseudo-second-order kinetic model			
q_e (mg/g)	169.6151	249.879	229.4719
K_2 (g/mg/min)	0.0020	0.0023	0.0024
R^2-adjusted	0.9316	0.9766	0.9801

Table 5-7 displays the results of the analysis for the pseudo-first-order kinetic model and the pseudo-second-order kinetic model. As compared to the pseudo-first-order kinetic model, the pseudo-second-order kinetic model obtained an adjusted R^2 that is closer to 1, which indicates that the pseudo-second-order kinetic model is more appropriate for the samples. In this study, it was confirmed that the adsorption process is not physical, but chemical in nature.

5.2.4 Cr (VI) Reduce Reaction Mechanism and kinetic model

The mechanism for Fe-Ni/MWCNTs can be summarized as follows:

First, Cr (VI) is absorbed by MWCNTs due to their large surface area, increasing the concentration of Cr (VI) in the vicinity of Fe-Ni/MWCNTs. The

purpose of this step is to test whether MWCNTs and Cr (VI) are physically attracted to each other.

Additionally, in this area, decorated Fe (0) reduced Cr (VI) into Cr (III) under the catalysation of Ni (0). In the meantime, Fe (0) is oxidised into Fe (III) and $Fe(OH)_3$. The results of XPS and XRD support this conclusion. Under experimental conditions, $Cr(OH)_3$ and $Fe(OH)_3$ are insoluble [138]. The reaction equations for this step are as follows:

iron nanoparticles' primary mechanism for reducing Cr (VI) is the electron transfer from Fe^0($E^0_{Fe^{2+}/Fe^0} = -0.44\,V$) to Cr (VI)($E^0_{HCrO_4^-/Cr^{3+}} = 1.36\,V$) [122]:

$$2HCrO_4^- + 14H^+ + 3Fe^0(s) \rightarrow 2Cr^{3+} + 8H_2O + 3Fe^{2+}$$

As $E^0_{Fe^{3+}/Fe^{2+}} = 0.77\,V < E^0_{HCrO_4^-/Cr^{3+}}$, the generated Fe^{2+} will also react with Cr (VI) [123]:

$$HCrO_4^- + 7H^+ + 3Fe^{2+} \rightarrow Cr(III) + 4H_2O + 3Fe^{3+}$$

The electrons also transfer from Fe^0 to Fe^{3+}:

$$Fe^0 + 2Fe^{3+} \rightarrow 3Fe^{2+}$$

By adding Ni, the reaction activity of Fe(0) will be much higher than without Ni as a result of the catalytic action [139]. Below is a diagram of the reaction mechanism:

$$Fe^0 + 2H_2O \rightarrow Fe^{2+} + H_2 + 2OH^-$$

$$2Ni^0 + H_2 \rightarrow 2Ni^0 - H\cdot$$

$$HCrO_4^- + 3Ni^0 - H\cdot + 4H^+ \rightarrow Cr(III) + 4H_2O + 3Ni^0$$

Lastly, $Cr(OH)_3$ and $Fe(OH)_3$ sediment are absorbed by MWCNTs and residual Fe (0). As a result of the layer, the rate of Fe (0) reduction and the

absorption of MWCNTs will be decreased. Based on the proportion of the layer covered area, the degree of decrease varies.

In conclusion, after all Fe (0) has been absorbed or consumed, residual MWCNTs continue to absorb Cr (VI) until they reach their maximum absorption capacity. Neither $Cr(OH)_3$ nor $Fe(OH)_3$ will dissolve back into solution for an extended period of time.

The major Cr (VI) status at low pH is $HCrO_4^-$ and $Cr_2O_7^{2-}$ [38].The higher removal efficiency at low pH is due to the highly protonated and positively charged surface of the adsorbent. Electrostatic force can attract $HCrO_4^-$ and $Cr_2O_7^{2-}$ to the adsorbent. As pH increases, the reaction rate and equilibrium are hugely affected by less H^+ and more OH^-. In addition, the surface of the adsorbent will be negatively charged, which drastically reduces its adsorption capacity.

As Cr (VI) adsorption is not a pure chemical or physical reaction, traditional pseudo-first-order kinetic models and pseudo-second-order kinetics cannot adequately describe it, so we use the equation discussed in 2.3.4 above.

This equation can be expressed as follows:

$$[Cr(VI)]_t = \frac{[Cr(VI)]_0 \text{错误!未定义书签。}}{C_{SC}^*[S]exp\{k(C_{SC}^*[S] - [Cr(VI)]_0 t)\} - [Cr(VI)]_0} \quad (5\text{-}1)$$

Where [Cr (VI)] represents the hexavalent chromium concentration (mmol/L) at time *t*. *k* represents rate coefficient (L $mmol^{-1}$ min^{-1}). $C_{SC}^*[S]$, represents the initial concentration of [SC]. [*S*] represents the sample concentration (g/L). C_{SC}^* represents the removal compacity of Cr (VI) per unit gram of sample (mmol/g). where *k* and C_{SC}^* represent the model constant parameters

and *t* represents the reaction time (s). Below is the fit result of the kinetic model:

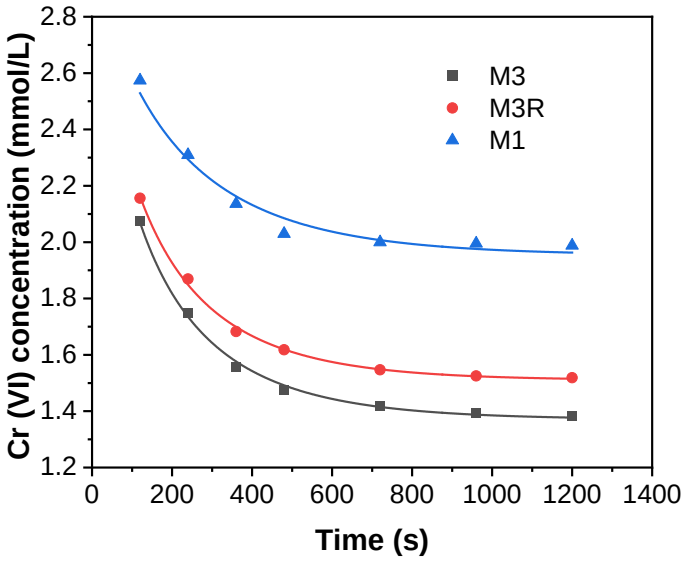

Figure 5-9 The kinetic model curve for M1, M3 and M3R

Table 5-8 The kinetic model results

	M1	M3	M3R
K (L mmol^{-1} min^{-1})	0.0178	0.1734	0.1650
C_{SC}^{*} (mmol/g)	2.8162	4.3445	3.9733
R2-adjusted	0.9981	0.9974	0.9972

As a result of the results, the kinetic model exhibits a high adjusted R^2, which confirms that the reaction mechanism and model are reasonable for the reduction reaction. By comparing the rate coefficient k between M1 and M3, it was determined that Ni (0) added to M3 increased the reaction coefficient by a considerable amount, which is the

result of Ni's catalyst effect. In the meantime, Comparing M3 and M3R, the decrease in K and C_{SC}^{*} is due to aggregation of Fe (0) and Ni (0) during the second reduction of Fe-Ni/MWCNTs.

5.3 Chapter summary

In this Chapter, a new Fe-Ni/MWCNTs composite for the efficient removal of Cr (VI) in aqueous solution was fabricated, in which MWCNTs serve as an adsorbent, Ni (0) as a catalyst, and Fe (0) as a reducing agent. They are brought together by co-precipitation and physical adsorption.

Compared to the sample without the addition of nickel, the added Ni tripled the BET surface of Fe-Ni/MWCNTs and the Cr (VI) removal capacity increased by 50 percent.

Fe-Ni/MWCNTs composites exhibit the maximum Cr (VI) adsorption at pH = 4.8 and pH = 5.6 with 256.87 mg/g and 224.43 mg/g, respectively.

In the Fe-Ni/MWCNTs, The added nickel has a higher reduction potential than Fe, which promotes the electron transfer of Fe(0) as the anode through electrochemical coupling, which not only enhances the reduction activity of nZVI; the nickel nanopowder is also able to catalyse the hydrogenolysis reaction and improve the hydrogenation reaction of nZVI; at the same time, it also reduces the loss of nZVI due to oxidation by the surrounding environmental medium.

MWCNTs reduce the agglomeration effect of Fe-Ni bimetal nanoparticles through spatial site resistance. It functions as an adsorbent to enrich Cr (VI) surrounding the material, which increases the directionality of the chemical reduction capacity of the material, and also provides part of the Cr (VI)

adsorption capacity based on its own physical adsorption. Fe (0) reacts with Cr (VI) to form Cr(OH)3 and Fe(OH)3 precipitates. These hydroxide precipitates and encapsulates Fe (0), preventing all iron from participating in the reaction, which is slowed down by the physical adsorption ability of the MWCNTs to adsorb some of the hydroxide precipitates onto its surface.

Additionally, under comparable circumstances, the results of Fe-Ni/MWCNTs are about 25 percent superior to those of Fe-Ni/RGO samples. Meanwhile Fe-Ni/MWCNTs exhibit some reusability, with 91 percent of adsorption capacity remaining for reused sample.

The following factors contribute to these outcomes:

1. According to DLS measurements, the dissociative Fe-Ni bimetal particle diameter for Fe-Ni/MWCNTs is about half that of Fe-Ni/RGO. The spatial site resistance of MWCNTs has a better effect on reducing the agglomeration of iron nanoparticles. As a result, the BET surface area and reaction points for bimetallic Fe-Ni on MWCNTs are fourfold increased. Surface area and reaction sites have a positive impact on adsorption capacity and reaction rate.

2. Both MWCNTs and RGO exhibit unordered stacking in SEM images; however, because the RGO sheet is significantly larger than the Fe-Ni bimetal particle diameter, it may be possible to completely encapsulate some Fe-Ni bimetal particles and prevent them from reacting with Cr (VI), resulting in a reduction in Cr (VI) adsorption capacity. Fe-Ni enters the system prior to the dispersion of RGO, which results in a greater amount of Fe-Ni bimetal being wrapped in RGO and a loss of reusability. In comparison, the diameter of MWCNTs is substantially smaller than that of Fe-Ni bimetal particles. It is difficult to encapsulate Fe-Ni bimetallic particles with MWCNTs.

Chapter 6

Fe/MWCNTs ratio and modelling for Fe/MWCNTS adsorption prediction

In recent years, a large number of iron-decorated materials have been investigated for their ability to remove heavy metal particles [140, 141]. The majority of these materials have a similar mechanism: iron acts as a reductant, while the base material acts as an adsorbent for Cr (VI). A huge amount of effort is necessary to analyse the adsorption capacity of various combinations, particularly to determine the optimal ratio for each component. A model that predicts the adsorption of a combined substance based on the data for two separate components would save a great deal of time and effort.

In this chapter, a model to predict the Cr adsorption capability of different ratios of Fe/MWCNTS composites is made. Prior to modelling, experiments were conducted with pure Fe and pure MWCNTs to gather the essential data for modelling, and the Cr adsorption capability of Fe/MWCNTS composites with varying ratios was examined to validate the model.

6.1 Preparation of iron nanoparticles and Fe/MWCNTs Composites

Different amount of 30 wt% $FeCl_3 \cdot 6H_2O$ solution is added into 50 mL of deionized water under magnetic stirring, forming $FeCl_3$ solution. 0.32 g MWCNTs and 2.0 g PVP are added into the obtained $FeCl_3$ solution and stirred for 30 mins. The ratio of Fe-MWCNTs is adjusted in different samples.

After that, 40 mL of 50 mg/mL $NaBH_4$ is added dropwise into the system and stirred overnight. $NaBH_4$ worked as a reducing agent and is expected to reduce Fe (III) to zero valent iron. In this period, magnetic stirring is replaced by mechanical oscillation to avoid Fe NPs affected by magnetic field. The MWCNTs is served as the base material to support iron nanoparticles. As H_2 is produced during this step, careful control is needed. The reaction equations are listed below:

$$Fe(H_2O)_6{}^{3+} + 3BH_4{}^{-} + 3H_2O = Fe^0 \downarrow + 3B(OH)_3 + 10.5H_2 \uparrow \quad (6\text{-}1)$$

The final product is collected by vacuum filtration, washed with ethanol three times, dried in a vacuum oven overnight, then collected and stored with nitrogen protection. A total of eight samples are prepared for the purpose of comparison, as given in Table 6-1.

Table 6-1 Detailed reaction conditions of different samples

Sample	60 wt% FeCl3 solution	MWCNTs	PVP	NaBH4	MWCNTs-Fe mass ratio
M1	1.033 ml	0.32 g	2 g	2 g	1.5
M11	1.936 ml	0.32 g	2 g	2 g	0.8
M12	1.549 ml	0.32 g	2 g	2 g	1
M13	0.775 ml	0.32 g	2 g	2 g	2
M14	0.516 ml	0.32 g	2 g	2 g	3
M15	0.310 ml	0.32 g	2 g	2 g	5
M16	0.194 ml	0.32 g	2 g	2 g	8

Pure Fe (0)	3.000 ml	/	2 g	2 g	/

6.2 Cr (VI) Adsorption Capacity Analyses

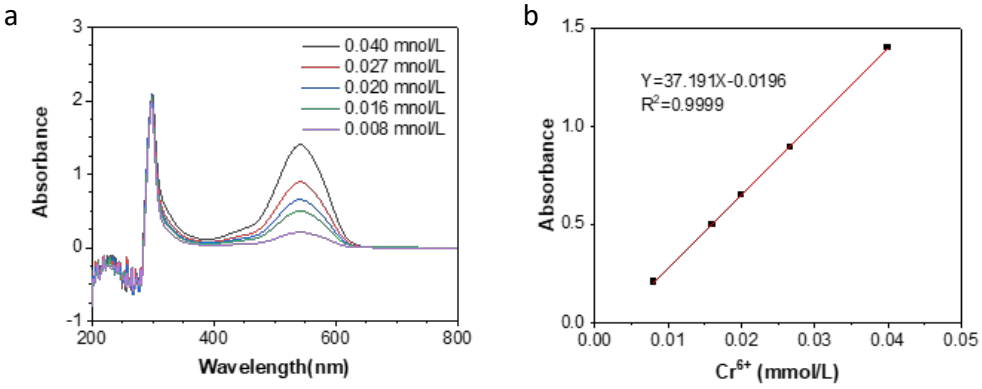

Figure 6-1 (a) UV-vis spectra of solutions of Cr (VI) reaction with DPC; (b) calibration curve line of Cr (VI) concentration (λ=545 nm)

UV-vis spectroscopy is used to determine the Cr (VI) concentration in a solution based on a validated calibration curve. UV-vis spectroscopy is a common analytical method, it analyses the amount of discrete wavelengths of ultraviolet or visible light that a sample absorbs to a standard or blank sample. This attribute is impacted by the sample's composition, and by evaluating the amount of light absorbed at different wavelengths, it is possible to determine the composition and concentration of the sample's constituents [142].

1,5-Diphenylcarbazide (DPC) method is used to measure the Cr (VI) concentration. DPC reacts in an acid medium with Cr (VI) ions to give a violet solution, at λ_{max} =545 nm, the violet solution obtains a characteristic peak. DPC solution is prepared in advance: 0.2 g DPC is dissolved in 100ml acetone which contains 1ml 95% H_2SO_4 (1+1).

The calibration curve is obtained by measuring a series of concentrations of Cr (VI) solutions react with DPC solution. In detail, 23ml 0.008 mmol/L, 0.016 mmol/L, 0.020 mmol/L, 0.027 mmol/L and 0.040 mmol/L Cr (VI) solutions are prepared and respectively react with 2ml DPC solution. Then the UV-vis absorption is examined after 5 minutes at λ_{max} =545 nm. A linear relationship is shown in Figure 6-1 (b) for Cr (VI) concentration. i.e., y = 37.191x - 0.0916 with R^2 = 0.9999, where y stands for absorption and x is Cr (VI) concentration. Based on the R-value particularly close to 1, this linear equation can be used to calculate the concentration of Cr (VI) at different UV sorption values in the concentration range of 0.01-0.04 mmol/L

15 mg of each sample is added into 34 mL PH buffer (Ph=5.6), ultrasonic dispersion to make sure the sample fully dispersed. Then, 6 mL of 20 mmol/L Cr (VI) solution added into the solution to make the whole solution to be 3 mmol/L Cr (VI) initially. Put the solution under mechanical oscillation. 0.5ml solution is drawn every time at the scheduled time and added into a bottle which includes 2 ml DPC solution and adds water to 25 ml. After 5 minutes, The UV absorption spectra of the solution are measured to determine the remaining Cr (VI) concentration. In most of the cases, the absorption became stable after 60 minutes (Figure 6-2). In the beginning, all Cr species are in hexavalent form, the adsorption capacity can be calculated by analysing the remaining Cr (VI) concentration.

Table 6-2 The Cr (VI) concentration of samples deduced

	pH	Adsorption percentage	Adsorption capacity (mg/g)	MWCNTs-Fe mass ratio
Iron nanoparticles	5.6	5.42%	22.56	\
MWCNTs	5.6	4.80%	19.95	\
M1	5.6	32.35%	134.57	1.5
M11	5.6	28.07%	116.77	0.8
M12	5.6	29.38%	122.24	1
M13	5.6	33.74%	140.35	2
M14	5.6	33.78%	140.54	3
M15	5.6	30.16%	125.47	5
M16	5.6	24.30%	101.07	8

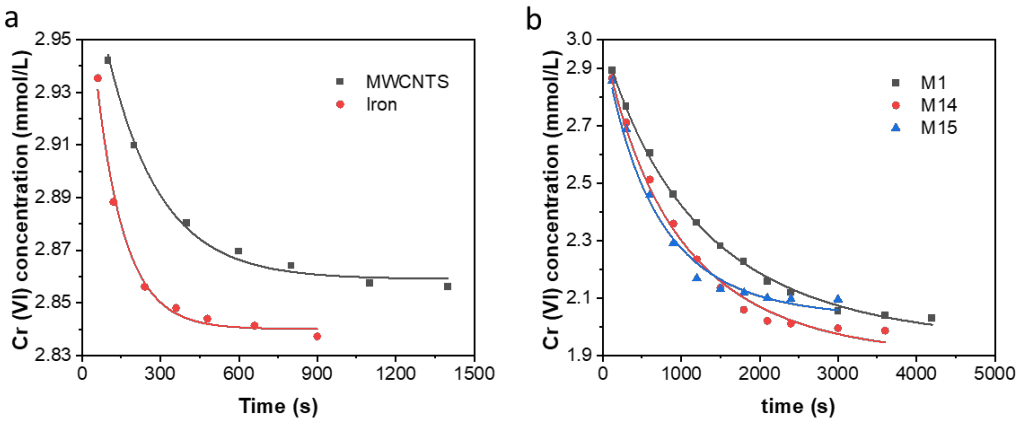

Figure 6-2 (a) Cr (VI) adsorption capacity with time for MWCNTs and iron (b) Cr (VI) adsorption capacity with time for M1, M14 and M15.

It is evident that Fe decorated on MWCNTs has a much higher adsorption capacity than pure MWCNTs and iron. That is due to the combined action between MWCNTs and iron. Due to the high specific surface area of MWCNTs. Cr (VI) is adsorbed to the area close to the MWCNTs surface, where Cr (VI) can be more efficiently reduced locally by the decorated nano iron.

At low pH, the major Cr(VI) status is $HCrO_4^-$ and $Cr_2O_7^{2-}$.[38] The higher removal efficiency at low pH is attributed to that the surface of the adsorbent becomes highly protonated and positively charged. The adsorbent can attract $HCrO_4^-$ and $Cr_2O_7^{2-}$ via electrostatic force. With the increase of pH, less H^+ and more OH^- hugely effected the reaction rate and equilibrium. Also, the adsorbent's surface will be negatively charged, which then highly decreases the adsorption capacity.

The following results are confirmed:

- All electrons are moved initially from Fe species and finally obtained by Cr species; it can be considered as Fe is the only element capable of reducing Cr (VI)

- The equation rate for the Cr (VI) reduction is first-order.
- The conversion ratio between Cr (VI) and Cr (III) is 1:1.

Considering the reaction mechanism mentioned above, a kinetic model is proposed to describe the Cr (VI) removal, When the pH and temperature are constant, as the rate equation common form is a power law [143] , the rate of Cr (VI) reduction by samples can be found as:

$$\frac{d[Cr(VI)]}{dt} = -k[SC][Cr(VI)] \tag{6-2}$$

Where [Cr (VI)] is the hexavalent chromium concentration (mmol/L) at time *t* and *k* its rate coefficient (L mmol^{-1} min^{-1}), [SC] represents the equivalent sample concentration at time t capable of reducing Cr (VI) (mmol L^{-1}). This parameter is fitted using experimental results as follows.

Considering that Fe^0 is oxidised during Cr (VI) reduction, the equivalent sample concentration on the surface of the samples decreases during the reaction and can be calculated as:

$$[SC]_t = C_{SC}^*[S](1 - \frac{[Cr(VI)]_0 - [Cr(VI)]_t}{C_{SC}^*[S]}) \tag{6-3}$$

where C_{SC}^* is the removal compacity of Cr (VI) per unit gram of sample (mmol/g), which is obtained by the adsorption capacity analysis experiment. [*S*] is the sample concentration (g/L), $C_{SC}^*[S]$, represents the initial concentration of [SC]. $[Cr(VI)]_0$ is the initial hexavalent chromium concentration (mmol/L). $\frac{[Cr(VI)]_0 - [Cr(VI)]_t}{C_{SC}^*[S]}$ represents the fraction of [SC] oxidised.

Integrating the above equations results in:

$$[Cr(VI)]_t = \frac{[Cr(VI)]_0 \text{错误! 未定义书签。}}{C_{SC}^*[S]exp\{k(C_{SC}^*[S] - [Cr(VI)]_0 t)\} - [Cr(VI)]_0} \quad (6\text{-}4)$$

where *k* and C_{SC}^* are the model constant parameters and *t* is the reaction time (min). The fitting result of the kinetic model is shown below:

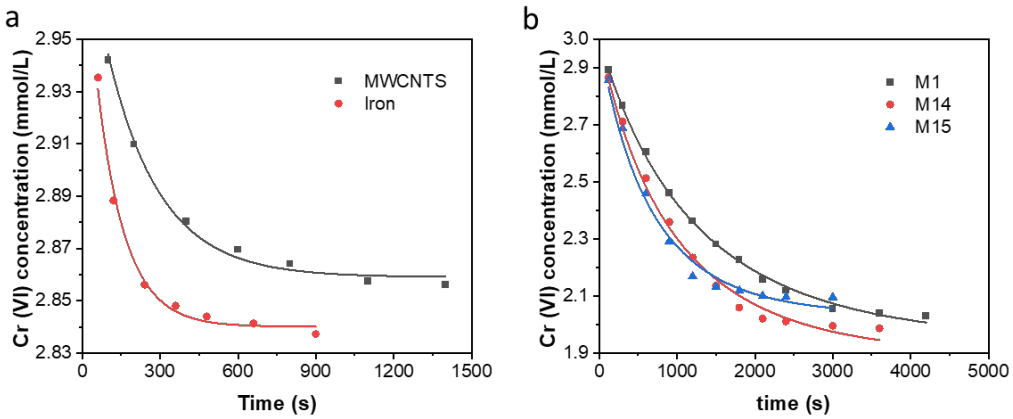

Figure 6-3 (a) Cr (VI) adsorption capacity with time for MWCNTs and iron (b) Cr (VI) adsorption capacity with time for M1, M14 and M15. The not obvious points are independent experiment data points, lines are equation (4-4)

Table 6-3 The kinetic model results

	MWCNTs	Iron	M1	M14	M15
k (L mmol^{-1} min^{-1})	0.1014	0.1902	0.0178	0.0232	0.0330
C_{SC}^* (mmol/g)	0.3760	0.42658	2.8162	2.9484	2.5737
R^2-adjusted	0.9937	0.9929	0.9981	0.9911	0.9867

The results show the kinetic model has high adjusted R^2, which confirmed the reaction mechanism and model are reasonable for the reduction reaction. By comparing the rate coefficient k between sample MWCNTs, iron and M1, M14,

M15 it indicated the mixture of MWCNTs and iron significantly enhance the rate coefficient.

6.3 Modelling for Fe/MWCNTS adsorption prediction

6.3.1 Mechanism analysis

The effect of $Cr(OH)_3$ and $Fe(OH)_3$ precipitation covering Fe(0) on the reaction was introduced based on the relevant fixed parameters of Fe(0) and MWCNTs. A model was developed for predicting the predicted adsorption capacity of different ratios of Fe/MWCNTs.

With the Cr (VI) reduction reaction mechanism analysis above, we can build a model to predict the adsorption capacity of Fe/MWCNTs at different ratio. The following mechanism are confirmed:

Firstly, Cr (VI) is absorbed by MWCNTs to its surface area, this increased the Cr (VI) concentration in the area close to Fe/MWCNTs.

Secondly, in this area, decorated Fe (0) reduced Cr (VI) to Cr (III) in the form of $Cr(OH)_3$ which is insoluble in the pH range experimented [144]. Meanwhile, Fe (0) is oxidised to Fe (III) as $Fe(OH)_3$. Which is also insoluble in experiment condition [145] . The reaction equations as below:

$$2HCrO_4^- + 14H^+ + 3Fe^0(s) \rightarrow 2Cr^{3+} + 8H_2O + 3Fe^{2+} \quad (6\text{-}5)$$

$$HCrO_4^- + 7H^+ + 3Fe^{2+} \rightarrow Cr(III) + 4H_2O + 3Fe\ (III) \quad (6\text{-}6)$$

$$Fe^0 + 2Fe\ (III) \rightarrow 3Fe^{2+} \quad (6\text{-}7)$$

Thirdly, Cr $(OH)_3$ and Fe $(OH)_3$ sediment are absorbed by MWCNTs and residual Fe (0). The layer will decrease the rate for Fe (0) reduction and MWCNTs absorption. The decreased degree is depending on the layer covered area proportion.

Finally, after all Fe (0) is covered or consumed, residual MWCNTs continue to absorb Cr (VI) to its surface area until the maximum absorption capacity is reached.

The above mechanisms or processes are modelled using reaction kinetics as described earlier in Section 4.2.

6.3.2 Key parameters identification and estimation

In order to simulate the experiment, we need to confirm some important parameters first.

Definition and estimation of A_s

A_s is defined as the covered area of Cr $(OH)_3$ and Fe $(OH)_3$ sediment for per gram of Cr (VI) reduced to Cr (III).

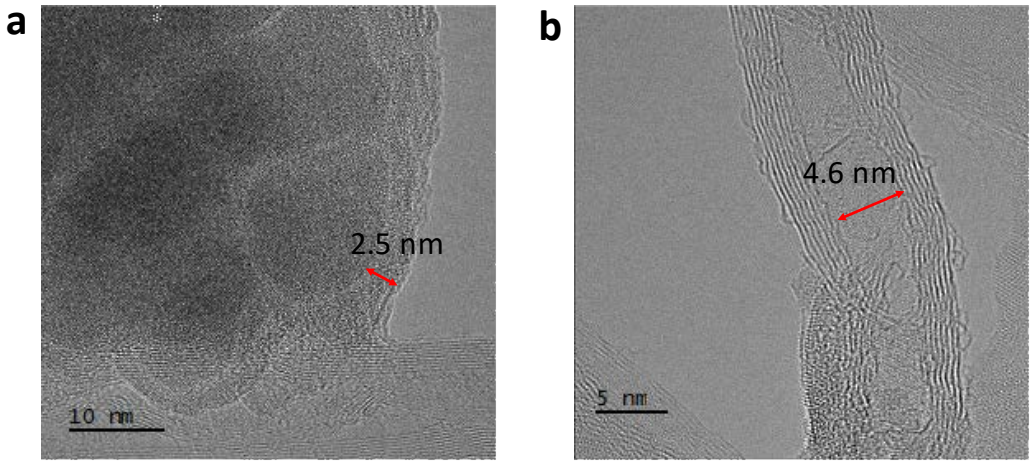

Figure 6-4 (a) Thickness of Cr $(OH)_3$ and Fe $(OH)_3$ sediment layer; (b) MWCNTs inner diameter.

From Figure 6-4 (a) the thickness of Cr $(OH)_3$ and Fe $(OH)_3$ sediment is about 2.5 nm. This is useful for defining parameter A_s

The molar mass of Cr, Cr $(OH)_3$ and Fe $(OH)_3$ are 52.00 g/mol, 103.02 g/mol and 106.87 g/mol respectively.

From the equation 6-2, 6-3 and 6-4, the molar ration of reduced Cr (VI), Cr $(OH)_3$ and Fe $(OH)_3$ are 1:1:1.

Density of Cr $(OH)_3$ and Fe $(OH)_3$ respectively: 3110000 g/m^3 and 3400000 g/m^3.

For per gram of Cr (VI) reduced to Cr (III), the volume of generated Cr $(OH)_3$ and Fe $(OH)_3$ sediment is A_g:

$$\mathrm{Ag} = \frac{1\ g * 103.02 \frac{\mathrm{g}}{\mathrm{mol}}}{52.00 \frac{\mathrm{g}}{\mathrm{mol}} * 3110000 \frac{\mathrm{g}}{\mathrm{m3}}} + \frac{1\ \mathrm{g} * 106.87 \frac{\mathrm{g}}{\mathrm{mol}}}{52.00 \frac{\mathrm{g}}{\mathrm{mol}} * 3400000 \frac{\mathrm{g}}{\mathrm{m3}}}$$

As the absorption layer thickness is 2.5 nm, for per gram of Cr (VI) reduced to Cr (III), the covered area of Cr $(OH)_3$ and Fe $(OH)_3$ sediment A_s is

$$A_s = \frac{\frac{1\ g * 103.02 \frac{\mathrm{g}}{\mathrm{mol}}}{52.00 \frac{\mathrm{g}}{\mathrm{mol}} * 3110000 \frac{\mathrm{g}}{\mathrm{m3}}} + \frac{1\ \mathrm{g} * 106.87 \frac{\mathrm{g}}{\mathrm{mol}}}{52.00 \frac{\mathrm{g}}{\mathrm{mol}} * 3400000 \frac{\mathrm{g}}{\mathrm{m3}}}}{2.5\ nm} = 496.63\ m^2$$

Specific area for MWCNTs and iron

Due to the extremely high length to diameter ratio, the inner area of MWCNTs is hard to competitive adsorb Cr $(OH)_3$ and Fe $(OH)_3$ sediment with iron. Only the outer surface area for MWCNTs is active area. From Figure 6-4 (b), the

inner diameter of MWCNTs is about 4.6 nm. By checking the diameter range with Table 6-4, the outer surface area for MWCNTs is about 118.494 m^2/g.

Table 6-4 Adsorption pore distribution report for MWCNTs

Pore Diameter Range (nm)	Cumulative Pore Area (m^2/g)
231.8 - 39.7	16.000
39.7 - 16.3	48.889
16.3 - 5.9	99.711
5.9 - 4.6	118.494
4.6 - 3.6	149.244
3.6 - 2.9	195.706
2.9 - 2.6	218.081
2.6 - 2.3	245.568
2.3 - 1.8	269.389

From the zeta sizer results in Table 6-4, iron particle average diameter is about 55 nm.

With a density of 7874000 g/m^3 and in sphere, the specific surface area for iron particle is about 13.85 m^2/g

Initial concentration of Cr (VI) is 156 g/m^3

6.3.3 Simulation equation derivation

Based on previous mechanistic analysis of the reaction of Fe/MWCNTs with Cr (VI) in section 6.3.1. The reaction between Fe and Cr (VI) produced $Cr(OH)_3$ and $Fe(OH)_3$ precipitates, which prevented further reaction of Fe with Cr (VI).

Section 6.2 demonstrated that the reaction curves of pure Fe (0) and pure MWCNTs with Cr (VI) fit the deformation equations of function 6-2 to a high degree and collects relevant fixed parameters based on Fe (0) and MWCNTs.

$$\frac{d[Cr(VI)]}{dt} = -k[SC]_t[Cr(VI)] \quad (6\text{-}2)$$

Section 6.3.2 quantified the distribution and thickness of the Cr(OH)3 and Fe(OH)3 precipitate adsorption layers on the surface of MWCNTs and iron particles.

This led to the introduction of relevant immobilisation parameters based on Fe (0) and MWCNTs and the effect of $Cr(OH)_3$ and $Fe(OH)_3$ precipitates covering Fe (0) on the reaction. A model based on function 6-2 was developed to predict the predicted adsorption capacity of different ratios of Fe/MWCNTs.

The details are given below.

The model is divided into two parts:

Part 1

Part 1 is for Cr (VI) absorbed by MWCNTs; Part 2 is for Cr (VI) reduced to Cr (III) by Fe (0). Both are modelled using the reaction kinetic rate equation (6-2) described earlier and reproduced below, but with different fitting parameter values.:

$$\frac{d[Cr(VI)]}{dt} = -k[SC]_t[Cr(VI)] \quad (6\text{-}2)$$

The R^2-adjusted for MWCNTs and iron are 0.98599 and 0.99162 respectively, so this equation can be used to build a model for Fe/MWCNTS.

Part 1 is for Cr (VI) absorbed by MWCNTs; it is divided into two stages: before and after iron leaves the reaction.

For the first stage:

$$\frac{d[Cr(VI)]_1}{dt} = -K_{MWCNTs}[SC]_t[Cr(VI)]_1$$

K_{MWCNTs} is the rate coefficient (L $mmol^{-1}$ min^{-1}) for MWCNTs, obtained from Table 6-3.

$$K_{MWCNTs} = 0.1014\ L/(mmol * \min)$$

$[Cr(VI)]_1$ is the average Cr (VI) concentration for the whole bulk, except for absorbed by MWCNTs.

$[SC]_t$ represents the equivalent sample concentration at time t.

From equation 4-3:

$$[SC]_t = C_{SC}^*[S]_{MWCNTS}(1 - \frac{[Cr(VI)]_0 - [Cr(VI)]_t}{C_{SC}^*[S]})$$

C_{SC}^* is the removal compacity of Cr (VI) per unit gram of sample (mmol/g), got from Table 6-3

$$C_{SC}^* = 0.37598\ \mathrm{mmol/g}$$

B is defined as the mass ratio of MWCNTs: iron. It is a constant parameter for each sample.

$[S]_{MWCNTS}$ is the sample concentration (g/L)

$$[S]_{MWCNTS} = \frac{15\ mg}{40\ ml} * \frac{B}{1+B}$$

As $\frac{[Cr(VI)]_0 - [Cr(VI)]_t}{C^*_{SC}[S]}$ represents the fraction of [SC] oxidised.

In this model, it can be defined as the covered area fraction of MWCNTs and iron, so:

$$[SC]_t = C^*_{SC}[S]_{MWCNTS}(1 - \frac{[Cr(VI)]_0 - [Cr(VI)]_t}{C^*_{SC}[S]}) = C^*_{SC}[S]_{MWCNTS}\frac{A_{Mt}}{A_{M0}}$$

A_{M0} and A_{Mt} are the uncovered surface area of MWCNTs at the initial time and t time, respectively.

As MWCNTs specific outer surface area: 118.49 m^2/g

$$A_{\mathrm{M0}} = 15\ mg * \frac{B}{1+B} * 118.49\ m^2/\mathrm{g}$$

At t time, the ratio of uncovered MWCNTs surface area and iron area is:

$$\frac{M_{MWCNTS} * 118.49\ m^2/\mathrm{g}}{M_{Fe} * 13.85\ m^2/g}$$

The total ratio of molar rate in equations 6-5, 6-6 and 6-7 for Fe (0) and Cr (VI) is 1:1.

The molar mass of Cr and Fe are 52.00 g/mol and 55.85 g/mol, respectively.

A_{Fe0} and A_{Fet} are the uncovered surface area of iron at initial time and t time, respectively.

At time t, the mass of residual iron

$$M_{Fet} = M_{Fe} - (156\frac{g}{m^3} - [Cr(VI)]_t) * \frac{55.85\ \mathrm{g/mol}}{52.00\ \mathrm{g/mol}} * 40\ ml$$

$$A_{\mathrm{Fe0}} = 15\ mg * \frac{1}{1+B} * 13.85\ m^2/\mathrm{g}$$

Expected for covered by sediments, the total surface area of iron also decreased with the consumption of iron, at t time the area is

$$A_{\mathrm{Fe0}} * (\frac{M_{Fet}}{M_{Fe}})^{\frac{2}{3}}$$

The iron particle can be treated as always being a sphere; mass and surface area are the cubic and quadratic of diameter, respectively. $\frac{2}{3}$ is the power of mass to the surface area.

At t time, the generated sediments are absorbed by MWCNTs and iron with the ratio of their total surface area.

$$A_{Mt} = A_{\mathrm{M0}} - \int_{156}^{[Cr(VI)]_t} \left\{ \frac{A_{\mathrm{M0}}}{A_{\mathrm{M0}} + A_{\mathrm{Fe0}} * \left(\frac{M_{Fet}}{M_{Fe}}\right)^{\frac{2}{3}}} * A_s * 40ml \right\} d[Cr(VI)]_t$$

$$A_{Fet} = A_{\mathrm{Fe0}} * (\frac{M_{Fet}}{M_{Fe}})^{\frac{2}{3}} - \int_{156}^{[Cr(VI)]_t} \left\{ \frac{A_{\mathrm{Fe0}} * \left(\frac{M_{Fet}}{M_{Fe}}\right)^{\frac{2}{3}}}{A_{\mathrm{M0}} + A_{\mathrm{Fe0}} * \left(\frac{M_{Fet}}{M_{Fe}}\right)^{\frac{2}{3}}} * A_s * 40ml \right\} d[Cr(VI)]_t$$

So, for part 1:

$$\frac{d[Cr(VI)]_1}{dt} = -K_{MWCNTs} C_{SC}^* [S]_{MWCNTS} \frac{A_{Mt}}{A_{M0}} [Cr(VI)]_1$$

Especially, after A_{Fet} decreased to 0, iron will no longer join the reaction, only MWCNTs absorb Cr (VI) to its surface area, it is the start of stage 2:

Define when $A_{Fet} = 0$, $[Cr(VI)]_1 = [Cr(VI)]_s$

$$\frac{d[Cr(VI)]_1}{dt} = -K_{MWCNTs} C_{SC}^* [S]_{MWCNTS} \frac{A_{Mt}}{A_{M0}} [Cr(VI)]_1$$

K_{MWCNTs}, C_{SC}^{*}, $[S]_{MWCNTS}$, A_{M0} and $[Cr(VI)]_1$ is the same as before.

From Table 6-2, the adsorption capacity for MWCNTs is $19.95\ \mathrm{mg/g}$, for per m^2 of MWCNTs surface area, the adsorption amount is

$$\frac{19.95\frac{\mathrm{mg}}{\mathrm{g}} * 15\mathrm{mg} * \frac{B}{B+1}}{A_{\mathrm{M0}}}$$

$([Cr(VI)]_s - [Cr(VI)]_1) * 40\mathrm{ml}$ is the absorbed Cr (VI) mass after t_s

So:

$$A_{Mt} = A_{\mathrm{M0}} - \int_{156}^{[Cr(VI)]_s} \left\{ \frac{A_{\mathrm{M0}}}{A_{\mathrm{M0}} + A_{\mathrm{Fe0}} * \left(\frac{M_{Fet}}{M_{Fe}}\right)^{\frac{2}{3}}} * A_s * 40ml \right\} d[Cr(VI)]_t$$

$$- - \frac{([Cr(VI)]_s - [Cr(VI)]_1) * 40\mathrm{ml}}{\frac{19.95\frac{\mathrm{mg}}{\mathrm{g}} * 15\mathrm{mg} * \frac{B}{B+1}}{A_{\mathrm{M0}}}}$$

Part 2

For part 2:

$$\frac{d[Cr(VI)]_2}{dt} = \frac{d[Cr(VI)]_1}{dt} * R - K_{Fe}[SC]_t[Cr(VI)]_2$$

From Table 6-3:

$$K_{Fe} = 0.1902L/(mmol * \mathrm{min})$$

$$[SC]_t = C_{SC}^{*}[S]_{Fe}(1 - \frac{[Cr(VI)]_0 - [Cr(VI)]_t}{C_{SC}^{*}[S]}) = C_{SC}^{*}[S]_{Fe}\frac{A_{Fet}}{A_{Fe0}}$$

$$C_{SC}^{*} = 0.42658\mathrm{mmol/g}$$

$$[S]_{Fe} = \frac{15\ mg}{40\ ml} * \frac{1}{1+B}$$

$$A_{\mathrm{Fe0}} = 15\ mg * \frac{1}{1+B} * 13.85\ m^2/\mathrm{g}$$

$$A_{Fet} = A_{\mathrm{Fe0}} * (\frac{M_{Fet}}{M_{Fe}})^{\frac{2}{3}}$$

$$-\int_{156}^{[Cr(VI)]_1} \left\{ \frac{A_{\mathrm{Fe0}} * \left(\frac{M_{Fet}}{M_{Fe}}\right)^{\frac{2}{3}}}{A_{\mathrm{M0}} + A_{\mathrm{Fe0}} * \left(\frac{M_{Fet}}{M_{Fe}}\right)^{\frac{2}{3}}} * A_s * 40ml \right\} d[Cr(VI)]_t$$

$[Cr(VI)]_2$ is the concentration of Cr (VI) close to the area close to Fe/MWCNTs.

R is the volume rate for whole bulk to the area close to Fe/MWCNTs

From Figure 6-2 (a), under the same condition, the time for MWCNTs and Iron to arrive Cr (VI) adsorption equilibrium point is similar. However, in the Fe/MWCNTs system, there is a much higher Cr (VI) concentration near iron due to the absorption of MWCNTs. It indicates iron will always arrive equilibrium point before MWCNTs; the time is the t_s mentioned before.

So, the equation for part 2 will not affect the Cr (VI) concentration curve for the whole bulk; we do not need to find the exact value for R.

Simplification

For part 1, stage 1

$$\frac{d[Cr(VI)]_t}{dt}$$

$$= 2.382 * 10^{-4} * \frac{B}{1+B} * [Cr(VI)]_t * (1$$

$$- \frac{\int_{156}^{[Cr(VI)]_t} \left\{ \frac{0.01987}{B * 118.49 + 13.85 * \left(1 - \frac{(156 - [Cr(VI)]_t) * 2.864}{\frac{1000}{1+B}}\right)^{\frac{2}{3}}} \right\} * d[Cr(VI)]_t}{0.015 * \frac{1}{1+B}})$$

At the particular time, when $A_{Fet} \leq 0$

$$\int_{156}^{x} \frac{(1 - \frac{(156 - [Cr(VI)]_s) * 2.864}{\frac{1000}{1+B}})^{\frac{2}{3}}}{\frac{B}{1+B} * 118.49 + \frac{1}{1+B} * 13.85 * (1 - \frac{(156 - [Cr(VI)]_s) * 2.864}{\frac{1000}{1+B}})^{\frac{2}{3}}}$$

$$* ((156 - x) * 0.01987 dx \geq (1 - \frac{(156 - [Cr(VI)]_s) * 2.864}{\frac{1000}{1+B}})^{\frac{2}{3}}$$

For part 1, stage 2

$$\frac{d[Cr(VI)]_t}{dt}$$

$$= 2.382 * 10^{-4} * \frac{B}{1+B} * [Cr(VI)]_t * (1$$

$$- \frac{\int_{156}^{[Cr(VI)]_s} \left\{ \frac{0.01987}{B * 118.49 + 13.85 * \left(1 - \frac{(156 - [Cr(VI)]_s) * 2.864}{\frac{1000}{1+B}} \right)^{\frac{2}{3}}} \right\} * d[Cr(VI)]_t}{0.015 * \frac{1}{1+B} *}$$

$$- \frac{([Cr(VI)]_s - [Cr(VI)]_t) * 0.134}{\frac{B}{B+1}})$$

6.4 Modelling results analysis

This model is based on the software “DigiDiss”, a dynamic digital simulation of dissolution software developed by Jia [146]. Some researchers obtained great high consistency between DigiDiss modelling and experiment data and proved it can be applied for predicting bulk particle dissolution [147, 148].

Based on the reaction mechanism discussed above, the reaction for Cr (VI) adsorption capacity experiment on the solid liquid interface, it is possible to simulate the experiment by DigiDiss.

A 5*5*1 liquid phase and a 5*5*4 solid phase are imported into a 5*5*5 bulk. Pixel width is set to 0.0342m to make the volume for one pixel is 40ml. The Time step is set to 0.1s to obtain an accepted time for running the whole progress. The comparison between experimental data and simulation data is shown below:

Table 6-5 Comparison between experiment and simulation data

	MWCNTs:Fe (weight)	Adsorption capacity (mg/g)		Relative error
		Experiment data	Simulation data	
Pure iron	0	22.56	21.6	4.26%
MWCNTs	∞	19.95	19.95	0.00%
M1	1.5	134.57	132.26	1.72%
M11	0.8	116.77	111.35	4.64%
M12	1	122.24	119.87	1.94%
M13	2	140.35	137.37	2.12%
M14	3	140.54	136.66	2.76%
M15	5	125.47	121.57	3.11%
M16	8	101.07	95.62	5.39%

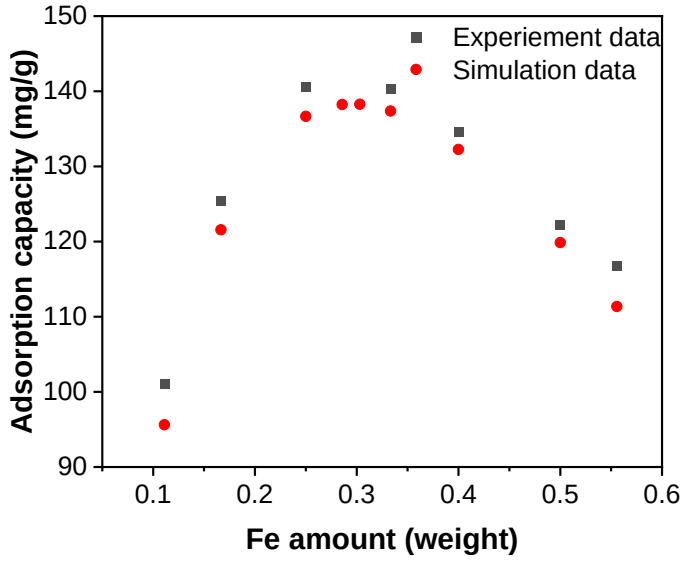

Figure 6-5 Comparison between experiment and simulation data

From Table 6-5 and Figure 6-5, it can be shown that for all samples with iron addition, the experimental and simulated data patterns for various MWCNTs and iron ratios are quite comparable. In most cases, the relative error is less than 5%. Due to the fact that not all Cr $(OH)_3$ and Fe $(OH)_3$ sediments were absorbed by MWCNTs and iron throughout the experiment, more iron was engaged in the process and the adsorption capacity was enhanced. The experiment data are always slightly above the simulation data.

According to modelling results, the model is in high agreement with experimental results at different Fe-MWCNTS ratios and can be used to predict the Cr (VI) adsorption capacity at different Fe-MWCNTS ratios. Cr (VI) adsorption capacity correlates favourably with iron mass. At a weight ratio of around 2.3 for MWCNTs to iron, samples exhibit the maximum Cr (VI) adsorption capability. When the ratio was less than 2,3, the Cr (VI) adsorption capacity increased as iron weight rose. When the ratio exceeded 2.3, the Cr (VI) adsorption capability declined as iron weight increased.

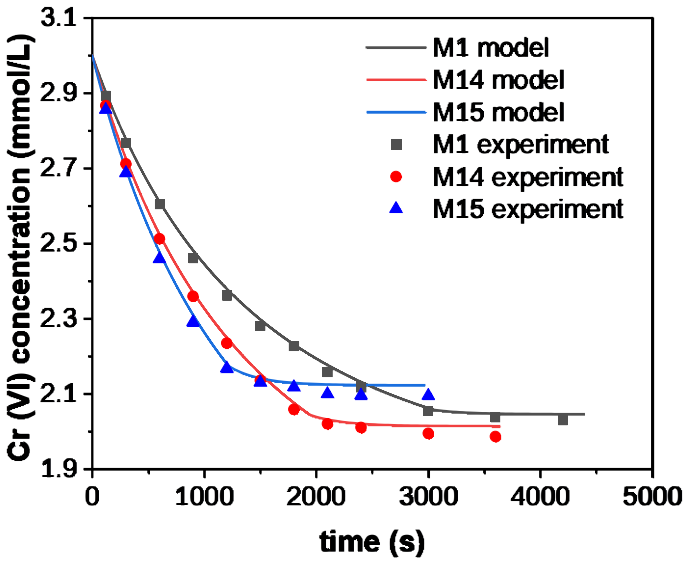

Figure 6-6 Comparison of adsorption curve by simulation (lines) and concentration collected by experiments (points)

In Figure 6-6, the line is for simulation adsorption curve; the points are data collected from experiments. The simulation results demonstrated an excellent agreement with the experimental results in terms of final adsorption capacity and adsorption curves, and could be used to forecast the adsorption capacity and curves for various ratios of Fe/MWCNTs.

As can be seen from Figure 6-5, the trend in Cr (VI) adsorption capacity with the ratio of Fe to MWCNTs is in high agreement between the experimental and simulated data. Meanwhile, in Figure 6-5, Cr (VI) adsorption curve by simulation shows excellent agreement with experiment data.

6.5 Chapter summary

Most of the Cr (VI) removal materials currently being investigated are multi-phase materials. Determining the optimal material ratios for Cr (VI) absorption capability requires substantial amount of effort.

In this Chapter, Fe/MWCNTs was chosen for modelling. A comparison of the experimental results with the simulated data shows that the model and experimental results show the same trend in Cr (VI) removal capacity as the proportion of Fe and MWCNTs in the material changes. The variation of Cr (VI) concentration with time at different times in the model is also highly consistent with the experimental results.

This model provides a convenient method for predicting the Cr (VI) adsorption capacity for Fe-MWCNTs two-phase material at different ratios. Moreover, in recent years, a large number of iron-decorated materials has been researched to deduct heavy metal particles [140, 141], and most of them have a similar mechanism to this experiment. This model can provide a convenient method for researchers to optimise the materials design with minimized experiments.

Chapter 7 Conclusions and Future work

7.1 Conclusions

To develop novel nano-composites that can efficiently reduce hexavalent chromium for environmental remediation, this work designed and synthesized two novel materials, i.e., reduced graphene oxide (RGO)-based and multi-walled carbon nanotube (MWCNT) based bimetallic nanocomposites, and one predictive model for further optimisation. The results show that Fe-Ni/MWCNTs nanocomposite can achieve 50% improvement in Cr (VI) removal capacity compared to the reported materials under similar conditions, while achieving reusability.

For RGO based nanocomposites, Fe-Ni bimetallic particles are loaded onto reduced graphene oxide through co-precipitation and physisorption method.

In this nanocomposite, combination with the dispersant, the spatial barrier effect of RGO reduces the agglomeration of Fe-Ni bimetallic particles. It functions as an adsorbent to enrich Cr (VI) surrounding the material, which increases the directionality of the chemical reduction capacity of the material, and also provides part of the Cr (VI) adsorption capacity based on its own physical adsorption. Fe functions as a reducing agent to convert Cr (VI) to Cr (III), which is less susceptible to re-oxidation in nature, preventing secondary contamination.

The added nickel has a higher reduction potential than Fe, which promotes the electron transfer of Fe (0) as the anode through electrochemical coupling, which not only enhances the reduction activity of iron nanoparticles; the nickel nanopowder is also able to catalyse the hydrogenolysis reaction and improve

the hydrogenation reaction of nZVI; at the same time, it also reduces the loss of nZVI due to oxidation by the surrounding environmental medium.

In the reduction process, Cr (VI) reacts with Fe (0) to form $Cr(OH)_3$ and $Fe(OH)_3$ precipitates. These hydroxide precipitates and encapsulates Fe (0), preventing all iron from participating in the reaction, which is slowed down by the physical adsorption ability of the RGO to adsorb some of the hydroxide precipitates onto its surface.

The experiments show that the capacity of Cr (VI) adsorption is more than 50 percent greater compared to reported literatures under similar conditions. At the same time, a micromixer chip was used for some of the samples instead of the traditional mechanical stirring to disperse the multisystem components during the synthesis. The results show a more homogeneous distribution of FeNi bimetallic particles on the RGO in the samples made after micromixer chip dispersion. The Cr (VI) removal capacity of the samples was increased by 50% compared to the conventional mechanical stirring. However, because FeNi bimetals are easily encased by RGO during secondary reduction, FeNi/RGO is not reusable.

For MWCNT based nanocomposites, multi-walled carbon nanotubes were utilised, instead of RGO, together with Fe-Ni bimetallic particles, to achieve reusability. Due to the unique tubular structure of MWCNTs and their extraordinarily high specific surface area, it is difficult to encapsulate FeNi bimetallic particles by MWCNTs. Also, for the agglomeration of iron nanoparticles, MWCNTs have better spatial resistance than RGO, and the particle size of the metal particles in Fe-Ni/MWCNTs is only half that of Fe-Ni/RGO.

The results demonstrate that the FeNi/MWCNTs material achieves about 25% greater adsorption capacity and faster equilibration time than FeNi/RGO, while retaining excellent recyclability.

Throughout the synthesis of FeNi/MWCNTs, no special experimental environment is required (e.g. inert gas protection) and the synthesis method can be scaled up. The most expensive of the raw materials, MWCNTs, are already industrially available at an acceptable price and will soon decrease in price due to the application of several new synthesis methods. Therefore, FeNi/MWCNTs have the potential to be used industrially.

To optimize the nanocomposite design, the effect of $Cr(OH)_3$ and $Fe(OH)_3$ precipitation covering Fe (0) on the reaction is introduced based on the relevant fixed parameters of Fe (0) and MWCNTs. A reduction and adsorption model is developed for predicting the adsorption capacity of different ratios of Fe/MWCNTs. The predicted trend in Cr (VI) adsorption capacity with the ratio of Fe to MWCNTs is in high agreement with the experimental data. This shows that the model could be used to forecast the adsorption capacity and curves for various ratios of Fe/MWCNTs. This model can be extended to other binary materials with similar mechanisms of reducing metals and adsorbents, greatly reducing the experimental effort required to find the optimum ratio of Cr removal materials and components.

7.2 Future work

On the experimental side, there is still potential to increase the adsorption capacity as not all iron involved in the reaction. Future research needs to focus on getting as much Fe involved in the reaction as possible rather than being

encapsulated by hydroxide precipitation and thus isolated from the reaction. Based on FeNi/MWCNTs, modification of MWCNTs to give them greater adsorption to hydroxide precipitates is a possible direction. Alternatively, materials with special adsorption to hydroxide precipitation may be sought for binding to FeNi bimetals.

In terms of simulation, extending the predictive model from the current Fe/MWCNTs to other two-phase materials is a possible direction. The analysis of the reaction mechanism of the bimetallic particles is also focused on, in an attempt to build up a predictive model and to establish a basis for further predictive modelling of three-phase materials.

List of References

1. Miensah, E.D., et al., *Zeolitic imidazolate frameworks and their derived materials for sequestration of radionuclides in the environment: A review.* Critical Reviews in Environmental Science and Technology, 2020. **50**(18): p. 1874-1934.
2. Chaudhry, F.N. and M. Malik, *Factors affecting water pollution: a review.* J Ecosyst Ecography, 2017. **7**(225): p. 1-3.
3. Vareda, J.P., A.J.M. Valente, and L. Durães, *Assessment of heavy metal pollution from anthropogenic activities and remediation strategies: A review.* Journal of Environmental Management, 2019. **246**: p. 101-118.
4. Tang, J., et al., *Diagnosis of soil contamination using microbiological indices: A review on heavy metal pollution.* Journal of Environmental Management, 2019. **242**: p. 121-130.
5. He, J., et al., *Assessment of soil heavy metal pollution using stochastic site indicators.* Geoderma, 2019. **337**: p. 359-367.
6. Otto, M., M. Floyd, and S. Bajpai, *Nanotechnology for site remediation.* Remediation Journal: The Journal of Environmental Cleanup Costs, Technologies & Techniques, 2008. **19**(1): p. 99-108.
7. Shen, H., et al., *New insights into the sorption and detoxification of chromium (VI) by tetraethylenepentamine functionalized nanosized magnetic polymer adsorbents: mechanism and pH effect.* Industrial & Engineering Chemistry Research, 2013. **52**(36): p. 12723-12732.
8. Mortvedt, J., *Heavy metal contaminants in inorganic and organic fertilizers*, in *Fertilizers and environment*. 1996, Springer. p. 5-11.
9. Zhao, Y., et al., *Enhanced photo-reduction and removal of Cr (VI) on reduced graphene oxide decorated with TiO2 nanoparticles.* Journal of colloid and interface science, 2013. **405**: p. 211-217.
10. Verma, R. and P. Dwivedi, *Heavy metal water pollution-A case study.* Recent Research in Science and Technology, 2013. **5**(5).
11. Tumolo, M., et al., *Chromium Pollution in European Water, Sources, Health Risk, and Remediation Strategies: An Overview.* International Journal of Environmental Research and Public Health, 2020. **17**(15): p. 5438.
12. Ku, Y. and I.L. Jung, *Photocatalytic reduction of Cr(VI) in aqueous solutions by UV irradiation with the presence of titanium dioxide.* Water Research, 2001. **35**(1): p. 135-142.
13. Kang, S.-Y., et al., *Competitive adsorption characteristics of Co2+, Ni2+, and Cr3+ by IRN-77 cation exchange resin in synthesized wastewater.* Chemosphere, 2004. **56**(2): p. 141-147.
14. Ölmez, T., *The optimization of Cr(VI) reduction and removal by electrocoagulation using response surface methodology.* Journal of Hazardous Materials, 2009. **162**(2): p. 1371-1378.
15. Ku, Y. and I.-L. Jung, *Photocatalytic reduction of Cr (VI) in aqueous solutions by UV irradiation with the presence of titanium dioxide.* Water Research, 2001. **35**(1): p. 135-142.
16. Fu, F. and Q. Wang, *Removal of heavy metal ions from wastewaters: A review.* Journal of Environmental Management, 2011. **92**(3): p. 407-418.

17. Huisman, J.L., G. Schouten, and C. Schultz, *Biologically produced sulphide for purification of process streams, effluent treatment and recovery of metals in the metal and mining industry.* Hydrometallurgy, 2006. **83**(1-4): p. 106-113.
18. Mirbagheri, S. and S. Hosseini, *Pilot plant investigation on petrochemical wastewater treatmentfor the removal of copper and chromium with the objective of reuse.* Desalination, 2005. **171**(1): p. 85-93.
19. Oura, K., et al., *Surface science: an introduction*. 2013: Springer Science & Business Media.
20. Largitte, L., et al., *Comparison of the adsorption of lead by activated carbons from three lignocellulosic precursors.* Microporous and Mesoporous Materials, 2016. **219**: p. 265-275.
21. Huang, Z.-n., X.-l. Wang, and D.-s. Yang, *Adsorption of Cr (VI) in wastewater using magnetic multi-wall carbon nanotubes.* Water Science and Engineering, 2015. **8**(3): p. 226-232.
22. Mthombeni, N.H., M.S. Onyango, and O. Aoyi, *Adsorption of hexavalent chromium onto magnetic natural zeolite-polymer composite.* Journal of the Taiwan Institute of Chemical Engineers, 2015. **50**: p. 242-251.
23. Cui, L., et al., *Removal of Hg (II) from aqueous solution by resin loaded magnetic β-cyclodextrin bead and graphene oxide sheet: synthesis, adsorption mechanism and separation properties.* Journal of colloid and interface science, 2015. **456**: p. 42-49.
24. Gode, F. and E. Pehlivan, *Removal of chromium (III) from aqueous solutions using Lewatit S 100: the effect of pH, time, metal concentration and temperature.* Journal of Hazardous Materials, 2006. **136**(2): p. 330-337.
25. Kumar, A., A. Thakur, and P.S. Panesar, *Extraction of hexavalent chromium by environmentally benign green emulsion liquid membrane using tridodecyamine as an extractant.* Journal of Industrial and Engineering Chemistry, 2019. **70**: p. 394-401.
26. Yao, Y., et al., *Nitrogen-doped carbon encapsulating molybdenum carbide and nickel nanostructures loaded with PVDF membrane for hexavalent chromium reduction.* Chemical Engineering Journal, 2018. **344**: p. 535-544.
27. Kurniawan, T.A., et al., *Physico–chemical treatment techniques for wastewater laden with heavy metals.* Chemical Engineering Journal, 2006. **118**(1): p. 83-98.
28. Faust, B.C., *A review of the photochemical redox reactions of iron (III) species in atmospheric, oceanic, and surface waters: influences on geochemical cycles and oxidant formation.* Aquatic and surface photochemistry, 2018: p. 3-38.
29. Sun, Y.-P., et al., *Characterization of zero-valent iron nanoparticles.* Advances in colloid and interface science, 2006. **120**(1-3): p. 47-56.
30. Nurmi, J.T., et al., *Characterization and properties of metallic iron nanoparticles: spectroscopy, electrochemistry, and kinetics.* Environmental Science & Technology, 2005. **39**(5): p. 1221-1230.
31. Gould, J.P., *The kinetics of hexavalent chromium reduction by metallic iron.* Water Research, 1982. **16**(6): p. 871-877.

32. Blowes, D. and C. Ptacek. *Geochemical remediation of groundwater by permeable reactive walls: removal of chromate by reaction with iron-bearing solids*. in *Subsurface Restoration Conference, 3rd International Conference on Ground Water Quality Research, June*. 1992.
33. Chang, L.-Y., *Alternative chromium reduction and heavy metal precipitation methods for industrial wastewater.* Environmental Progress, 2003. **22**(3): p. 174-182.
34. Blowes, D.W., C.J. Ptacek, and J.L. Jambor, *In-Situ Remediation of Cr(VI)-Contaminated Groundwater Using Permeable Reactive Walls: Laboratory Studies.* Environmental Science & Technology, 1997. **31**(12): p. 3348-3357.
35. Ramos, M.A., et al., *Simultaneous oxidation and reduction of arsenic by zero-valent iron nanoparticles: Understanding the significance of the core− shell structure.* The Journal of Physical Chemistry C, 2009. **113**(33): p. 14591-14594.
36. Boparai, H.K., M. Joseph, and D.M. O'Carroll, *Kinetics and thermodynamics of cadmium ion removal by adsorption onto nano zerovalent iron particles.* Journal of hazardous materials, 2011. **186**(1): p. 458-465.
37. Hwang, Y.-H., D.-G. Kim, and H.-S. Shin, *Mechanism study of nitrate reduction by nano zero valent iron.* Journal of Hazardous Materials, 2011. **185**(2): p. 1513-1521.
38. García-Sosa, I. and M.T. Olguín, *Comparison Between the Cr(VI) Adsorption by Hydrotalcite and Hydrotalcite-Gibbsite Compounds.* Separation Science and Technology, 2015. **50**(17): p. 2631-2638.
39. Jung, C., et al., *Hexavalent chromium removal by various adsorbents: Powdered activated carbon, chitosan, and single/multi-walled carbon nanotubes.* Separation and Purification Technology, 2013. **106**: p. 63-71.
40. Cao, J. and W.-X. Zhang, *Stabilization of chromium ore processing residue (COPR) with nanoscale iron particles.* Journal of Hazardous Materials, 2006. **132**(2-3): p. 213-219.
41. Wang, C.-B. and W.-X. Zhang, *Synthesizing nanoscale iron particles for rapid and complete dechlorination of TCE and PCBs.* Environmental science & technology, 1997. **31**(7): p. 2154-2156.
42. Křížek, M., et al. *Iron oxide nanoparticle powders with high surface area*. in *AIP Conference Proceedings*. 2012. AIP.
43. Nahuel Montesinos, V., et al., *Highly efficient removal of Cr(VI) from water with nanoparticulated zerovalent iron: Understanding the Fe(III)–Cr(III) passive outer layer structure.* Chemical Engineering Journal, 2014. **244**: p. 569-575.
44. Chen, Z., et al., *Macroscopic and microscopic investigation of Cr(VI) immobilization by nanoscaled zero-valent iron supported zeolite MCM-41 via batch, visual, XPS and EXAFS techniques.* Journal of Cleaner Production, 2018. **181**: p. 745-752.
45. Ai, Z., et al., *Efficient Removal of Cr(VI) from Aqueous Solution with Fe@Fe2O3 Core−Shell Nanowires.* Environmental Science & Technology, 2008. **42**(18): p. 6955-6960.

46. Lv, Z., et al., *Nanoscale zero-valent iron/magnetite carbon composites for highly efficient immobilization of U(VI).* Journal of Environmental Sciences, 2019. **76**: p. 377-387.
47. Li, S., et al., *Heavy metal removal using nanoscale zero-valent iron (nZVI): Theory and application.* Journal of Hazardous Materials, 2017. **322**: p. 163-171.
48. O'Carroll, D., et al., *Nanoscale zero valent iron and bimetallic particles for contaminated site remediation.* Advances in Water Resources, 2013. **51**: p. 104-122.
49. Yu, S., et al., *Recent advances in metal-organic framework membranes for water treatment: A review.* Science of The Total Environment, 2021. **800**: p. 149662.
50. Kocur, C.M., B.E. Sleep, and D.M. O'Carroll, *Moving Into the Third Decade of Nanoscale zero-valent Iron (nZVI) Development: Best Practices for Field Implementation*, in *Nanoscale Zerovalent Iron Particles for Environmental Restoration*. 2019, Springer. p. 293-333.
51. Quiton, K.G.N., M.-C. Lu, and Y.-H. Huang, *Synthesis and catalytic utilization of bimetallic systems for wastewater remediation: A review.* Chemosphere, 2021. **262**: p. 128371.
52. Chen, L., et al., *Multivariate optimization of ciprofloxacin removal by polyvinylpyrrolidone stabilized NZVI/Cu bimetallic particles.* Chemical Engineering Journal, 2019. **365**: p. 183-192.
53. Wang, S., et al., *Biochar-supported nZVI (nZVI/BC) for contaminant removal from soil and water: a critical review.* Journal of Hazardous Materials, 2019. **373**: p. 820-834.
54. Grittini, C., et al., *Rapid dechlorination of polychlorinated biphenyls on the surface of a Pd/Fe bimetallic system.* Environmental science & technology, 1995. **29**(11): p. 2898-2900.
55. Huang, Q., et al., *Reductive dechlorination of tetrachlorobisphenol A by Pd/Fe bimetallic catalysts.* Journal of Hazardous Materials, 2013. **262**: p. 634-641.
56. Lai, B., et al., *Removal of p-nitrophenol (PNP) in aqueous solution by the micron-scale iron–copper (Fe/Cu) bimetallic particles.* Applied Catalysis B: Environmental, 2014. **144**: p. 816-830.
57. Angaru, G.K.R., et al., *Facile synthesis of economical feasible fly ash–based zeolite–supported nano zerovalent iron and nickel bimetallic composite for the potential removal of heavy metals from industrial effluents.* Chemosphere, 2021. **267**: p. 128889.
58. Wen, Z., et al., *Facile inverse micelle fabrication of magnetic ordered mesoporous iron cerium bimetal oxides with excellent performance for arsenic removal from water.* Journal of Hazardous Materials, 2020. **383**: p. 121172.
59. Wen, Z., et al., *Facile template-free fabrication of iron manganese bimetal oxides nanospheres with excellent capability for heavy metals removal.* Journal of Colloid and Interface Science, 2017. **486**: p. 211-218.
60. Zhou, Y., et al., *A combination of bentonite-supported bimetallic Fe/Pd nanoparticles and biodegradation for the remediation of p-chlorophenol in wastewater.* Chemical engineering journal, 2013. **223**: p. 68-75.

61. Liu, W.-J., T.-T. Qian, and H. Jiang, *Bimetallic Fe nanoparticles: recent advances in synthesis and application in catalytic elimination of environmental pollutants.* Chemical Engineering Journal, 2014. **236**: p. 448-463.
62. Tee, Y.-H., E. Grulke, and D. Bhattacharyya, *Role of Ni/Fe Nanoparticle Composition on the Degradation of Trichloroethylene from Water.* Industrial & Engineering Chemistry Research, 2005. **44**(18): p. 7062-7070.
63. Schrick, B., et al., *Hydrodechlorination of trichloroethylene to hydrocarbons using bimetallic nickel− iron nanoparticles.* Chemistry of Materials, 2002. **14**(12): p. 5140-5147.
64. Chen, B., et al., *Nanocasted synthesis of ordered mesoporous cerium iron mixed oxide and its excellent performances for As(v) and Cr(vi) removal from aqueous solutions.* Dalton Transactions, 2014. **43**(28): p. 10767-10777.
65. Wen, Z., et al., *Simultaneous removal of As(V)/Cr(VI) and acid orange 7 (AO7) by nanosized ordered magnetic mesoporous Fe-Ce bimetal oxides: Behavior and mechanism.* Chemosphere, 2019. **218**: p. 1002-1013.
66. Zhou, X., et al., *Highly efficient removal of chromium(VI) by Fe/Ni bimetallic nanoparticles in an ultrasound-assisted system.* Chemosphere, 2016. **160**: p. 332-341.
67. O'Carroll, D., et al., *Nanoscale zero valent iron and bimetallic particles for contaminated site remediation.* Advances in Water Resources, 2013. **51**: p. 104-122.
68. Mokete, R., O. Eljamal, and Y. Sugihara, *Exploration of the reactivity of nanoscale zero-valent iron (NZVI) associated nanoparticles in diverse experimental conditions.* Chemical Engineering and Processing-Process Intensification, 2020. **150**: p. 107879.
69. Guggenheim, S. and R. Martin, *Definition of clay and clay mineral: joint report of the AIPEA nomenclature and CMS nomenclature committees.* Clays and clay minerals, 1995. **43**(2): p. 255-256.
70. Uddin, M.K., *A review on the adsorption of heavy metals by clay minerals, with special focus on the past decade.* Chemical Engineering Journal, 2017. **308**: p. 438-462.
71. Zhao, Y., et al., *Effective adsorption of Cr (VI) from aqueous solution using natural Akadama clay.* Journal of Colloid and Interface Science, 2013. **395**: p. 198-204.
72. Castro-Castro, J.D., et al., *Adsorption of Cr(VI) in Aqueous Solution Using a Surfactant-Modified Bentonite.* The Scientific World Journal, 2020. **2020**: p. 3628163.
73. Jinhua, W., et al., *Rapid adsorption of Cr (VI) on modified halloysite nanotubes.* Desalination, 2010. **259**(1): p. 22-28.
74. Shi, L.-n., X. Zhang, and Z.-l. Chen, *Removal of Chromium (VI) from wastewater using bentonite-supported nanoscale zero-valent iron.* Water Research, 2011. **45**(2): p. 886-892.
75. Fu, R., et al., *The removal of chromium (VI) and lead (II) from groundwater using sepiolite-supported nanoscale zero-valent iron (S-NZVI).* Chemosphere, 2015. **138**: p. 726-734.

76. Lu, H., et al., *Montmorillonite-Supported Fe/Ni Bimetallic Nanoparticles for Removal of Cr (VI) from Wastewater.* Chemical Engineering Transactions, 2017. **60**: p. 169-174.
77. Shaheen, S.M., et al., *Wood-based biochar for the removal of potentially toxic elements in water and wastewater: a critical review.* International Materials Reviews, 2019. **64**(4): p. 216-247.
78. Uysal, M. and I. Ar, *Removal of Cr(VI) from industrial wastewaters by adsorption: Part I: Determination of optimum conditions.* Journal of Hazardous Materials, 2007. **149**(2): p. 482-491.
79. Altun, T., Ş. Parlayıcı, and E. Pehlivan, *Hexavalent chromium removal using agricultural waste "rye husk".* Desalination and Water Treatment, 2016. **57**(38): p. 17748-17756.
80. Gao, H., et al., *Characterization of Cr(VI) removal from aqueous solutions by a surplus agricultural waste—Rice straw.* Journal of Hazardous Materials, 2008. **150**(2): p. 446-452.
81. Gonzalez, M.H., et al., *Coconut coir as biosorbent for Cr(VI) removal from laboratory wastewater.* Journal of Hazardous Materials, 2008. **159**(2): p. 252-256.
82. Khezami, L. and R. Capart, *Removal of chromium(VI) from aqueous solution by activated carbons: Kinetic and equilibrium studies.* Journal of Hazardous Materials, 2005. **123**(1): p. 223-231.
83. Wang, Y., et al., *Cr(VI) adsorption on activated carbon: Mechanisms, modeling and limitations in water treatment.* Journal of Environmental Chemical Engineering, 2020. **8**(4): p. 104031.
84. Wang, Q., et al., *Reduction of hexavalent chromium by carboxymethyl cellulose-stabilized zero-valent iron nanoparticles.* Journal of Contaminant Hydrology, 2010. **114**(1): p. 35-42.
85. Sharma, A.K., et al., *In situ reductive regeneration of zerovalent iron nanoparticles immobilized on cellulose for atom efficient Cr(vi) adsorption.* RSC Advances, 2015. **5**(109): p. 89441-89446.
86. Tkachev, S.V., et al., *Reduced graphene oxide.* Inorganic Materials, 2012. **48**(8): p. 796-802.
87. Jabeen, H., et al., *Enhanced Cr(vi) removal using iron nanoparticle decorated graphene.* Nanoscale, 2011. **3**(9): p. 3583-3585.
88. Li, J., et al., *Nanoscale Zero-Valent Iron Particles Supported on Reduced Graphene Oxides by Using a Plasma Technique and Their Application for Removal of Heavy-Metal Ions.* Chemistry – An Asian Journal, 2015. **10**(6): p. 1410-1417.
89. Li, X., L. Ai, and J. Jiang, *Nanoscale zerovalent iron decorated on graphene nanosheets for Cr(VI) removal from aqueous solution: Surface corrosion retard induced the enhanced performance.* Chemical Engineering Journal, 2016. **288**(Supplement C): p. 789-797.
90. Lv, X., et al., *Nanoscale Zero-Valent Iron (nZVI) assembled on magnetic Fe3O4/graphene for Chromium (VI) removal from aqueous solution.* Journal of Colloid and Interface Science, 2014. **417**: p. 51-59.
91. Wang, D., et al., *Synthesis of a Multifunctional Graphene Oxide-Based Magnetic Nanocomposite for Efficient Removal of Cr(VI).* Langmuir, 2017. **33**(28): p. 7007-7014.

92. Arunkumar, T., et al., *Synthesis and characterisation of multi-walled carbon nanotubes (MWCNTs).* International Journal of Ambient Energy, 2020. **41**(4): p. 452-456.
93. Atieh, M.A., *Removal of Chromium (VI) from polluted water using carbon nanotubes supported with activated carbon.* Procedia Environmental Sciences, 2011. **4**: p. 281-293.
94. Krishna Kumar, A.S., S.-J. Jiang, and W.-L. Tseng, *Effective adsorption of chromium(vi)/Cr(iii) from aqueous solution using ionic liquid functionalized multiwalled carbon nanotubes as a super sorbent.* Journal of Materials Chemistry A, 2015. **3**(13): p. 7044-7057.
95. Sun, L., et al., *Adsorption Separation of Cr(VI) from a Water Phase Using Multiwalled Carbon Nanotube-Immobilized Ionic Liquids.* ACS Omega, 2020. **5**(36): p. 22827-22839.
96. Lee, C.-G. and S.-B. Kim, *Cr(VI) Adsorption to Magnetic Iron Oxide Nanoparticle-Multi-Walled Carbon Nanotube Adsorbents.* Water Environment Research, 2016. **88**(11): p. 2111-2120.
97. Ma, T., et al., *Adsorption behavior of Cr(VI) and As(III) on multiwall carbon nanotubes modified by iron–manganese binary oxide (FeMnOx/MWCNTs) from aqueous solution.* Separation Science and Technology, 2022. **57**(2): p. 192-208.
98. Verdugo, E.M., et al., *Hematite decorated multi-walled carbon nanotubes (α-Fe2O3/MWCNTs) as sorbents for Cu(ii) and Cr(vi): comparison of hybrid sorbent performance to its nanomaterial building blocks.* RSC Advances, 2016. **6**(102): p. 99997-100007.
99. Murali, A., P.K. Sarswat, and M.L. Free, *Adsorption-coupled reduction mechanism in ZnO-Functionalized MWCNTs nanocomposite for Cr (VI) removal and improved anti-photocorrosion for photocatalytic reduction.* Journal of Alloys and Compounds, 2020. **843**: p. 155835.
100. Mosai, A.K., B.C. Tokwana, and H. Tutu, *Computer simulation modelling of the simultaneous adsorption of Cd, Cu and Cr from aqueous solutions by agricultural clay soil: A PHREEQC geochemical modelling code coupled to parameter estimation (PEST) study.* Ecological Modelling, 2022. **465**: p. 109872.
101. Karimifard, S. and M.R. Alavi Moghaddam, *Application of response surface methodology in physicochemical removal of dyes from wastewater: A critical review.* Science of The Total Environment, 2018. **640-641**: p. 772-797.
102. Witek-Krowiak, A., et al., *Application of response surface methodology and artificial neural network methods in modelling and optimization of biosorption process.* Bioresource technology, 2014. **160**: p. 150-160.
103. Li, D., et al., *Processable aqueous dispersions of graphene nanosheets.* Nature nanotechnology, 2008. **3**(2): p. 101-105.
104. Stetefeld, J., S.A. McKenna, and T.R. Patel, *Dynamic light scattering: a practical guide and applications in biomedical sciences.* Biophysical Reviews, 2016. **8**(4): p. 409-427.
105. Giusti, L. and S. Barakat, *The monitoring of Cr (III) and Cr (VI) in natural water and synthetic solutions: an assessment of the performance of the DGT and DPC methods.* Water, Air, and Soil Pollution, 2005. **161**(1): p. 313-334.

106. Saleem, H., M. Haneef, and H.Y. Abbasi, *Synthesis route of reduced graphene oxide via thermal reduction of chemically exfoliated graphene oxide.* Materials Chemistry and Physics, 2018. **204**: p. 1-7.
107. Yang, C., et al., *Magnetoviscous Property and Hyperthermia Effect of Amorphous Nanoparticle Aqueous Ferrofluids.* Nanoscale Research Letters, 2018. **13**(1): p. 378.
108. Cheban, Y.V., S.-F. Lau, and B. Wunderlich, *Analysis of the contribution of skeletal vibrations to the heat capacity of linear macromolecules in the solid state.* Colloid and Polymer Science, 1982. **260**(1): p. 9-19.
109. Dong, L., et al., *Improved solvothermal method for cutting graphene oxide into graphene quantum dots.* Digest J. Nanomater. Biostruct, 2015. **10**: p. 855-864.
110. Guan, X.-h., G.-h. Chen, and C. Shang, *ATR-FTIR and XPS study on the structure of complexes formed upon the adsorption of simple organic acids on aluminum hydroxide.* Journal of Environmental Sciences, 2007. **19**(4): p. 438-443.
111. Sun, Q., *The Raman OH stretching bands of liquid water.* Vibrational Spectroscopy, 2009. **51**(2): p. 213-217.
112. Thakur, R., et al., *CHROMIUM: AS A POLLUANT.* J Ind Pollut Control, 2007. **23**: p. 197-203.
113. Biesinger, M.C., et al., *Resolving surface chemical states in XPS analysis of first row transition metals, oxides and hydroxides: Cr, Mn, Fe, Co and Ni.* Applied Surface Science, 2011. **257**(7): p. 2717-2730.
114. Pan, F., et al., *Nanoscale zero-valent iron/persulfate enhanced upflow anaerobic sludge blanket reactor for dye removal: Insight into microbial metabolism and microbial community.* Scientific Reports, 2017. **7**: p. 44626.
115. Chagas, P., et al., *??-FeOOH: A superparamagnetic material for controlled heat release under AC magnetic field.* Journal of Nanoparticle Research, 2013. **15**: p. 1.
116. Mishra, A.K. and S. Ramaprabhu, *Carbon dioxide adsorption in graphene sheets.* AIP Advances, 2011. **1**(3): p. 032152.
117. Yang, Z., et al., *Self-Assembly 3D Porous Crumpled MXene Spheres as Efficient Gas and Pressure Sensing Material for Transient All-MXene Sensors.* Nano-micro letters, 2022. **14**(1): p. 1-14.
118. Wang, Q., et al., *Effects and mechanism of humic acid on chromium(VI) removal by zero-valent iron (Fe0) nanoparticles.* Physics and Chemistry of the Earth, Parts A/B/C, 2011. **36**(9): p. 442-446.
119. Zhou, X., et al., *Evaluation of highly active nanoscale zero-valent iron coupled with ultrasound for chromium(VI) removal.* Chemical Engineering Journal, 2015. **281**: p. 155-163.
120. Lin, J. and L. Wang, *Comparison between linear and non-linear forms of pseudo-first-order and pseudo-second-order adsorption kinetic models for the removal of methylene blue by activated carbon.* Frontiers of Environmental Science & Engineering in China, 2009. **3**(3): p. 320-324.
121. Jasuja, K. and V. Berry, *Implantation and Growth of Dendritic Gold Nanostructures on Graphene Derivatives: Electrical Property Tailoring and Raman Enhancement.* ACS Nano, 2009. **3**(8): p. 2358-2366.

122. Gheju, M., *Hexavalent Chromium Reduction with Zero-Valent Iron (ZVI) in Aquatic Systems.* Water, Air, & Soil Pollution, 2011. **222**(1): p. 103-148.
123. dos Santos Coelho, F., et al., *Potential application of highly reactive Fe(0)/Fe3O4 composites for the reduction of Cr(VI) environmental contaminants.* Chemosphere, 2008. **71**(1): p. 90-96.
124. Schrick, B., et al., *Hydrodechlorination of Trichloroethylene to Hydrocarbons Using Bimetallic Nickel−Iron Nanoparticles.* Chemistry of Materials, 2002. **14**(12): p. 5140-5147.
125. Nie, P., et al., *Preparation and Tribological Properties of Polyimide/Carboxyl-Functionalized Multi-walled Carbon Nanotube Nanocomposite Films Under Seawater Lubrication.* Tribology Letters, 2015. **58**.
126. Li, J., et al., *The role of iron oxide in the highly effective Fe-modified Co3O4 catalyst for low-temperature CO oxidation.* RSC Adv., 2013. **3**.
127. Mikhaylov, V.I., *Optical and thermal properties of sol–gel Al(OH)3–Fe(OH)3–PVA composite films.* Journal of Sol-Gel Science and Technology, 2019. **92**(2): p. 282-292.
128. Pan, C., et al., *Understanding the Roles of Dissolution and Diffusion in Cr(OH)3 Oxidation by δ-MnO2.* ACS Earth and Space Chemistry, 2019. **3**(3): p. 357-365.
129. Amonette, J.E. and D. Rai, *Identification of Noncrystalline (Fe,Cr)(Oh)3 by Infrared Spectroscopy.* Clays and Clay Minerals, 1990. **38**(2): p. 129-136.
130. Kumar, R., et al., *Functionalized Pd-decorated and aligned MWCNTs in polycarbonate as a selective membrane for hydrogen separation.* International Journal of Hydrogen Energy, 2016.
131. Sharifpour, N., et al., *Evaluation of the activated carbon coated with multiwalled carbon nanotubes in removal of ciprofloxacin from aqueous solutions.* Applied Water Science, 2020. **10**(6): p. 140.
132. Choudhary, B., et al., *Removal of hexavalent chromium upon interaction with biochar under acidic conditions: mechanistic insights and application.* Environmental Science and Pollution Research, 2017. **24**: p. 1-12.
133. Li, W., et al., *Zero valent iron as an electron transfer agent in a reaction system based on zero valent iron/magnetite nanocomposites for adsorption and oxidation of Sb(III).* Journal of the Taiwan Institute of Chemical Engineers, 2018. **85**: p. 155-164.
134. Chen, X., et al., *Vertical Fe(OH)3/Ni9S8 nanoarrays electrodeposited on stainless steel as binder-free electrocatalyst for highly efficient and stable oxygen evolution reaction.* Journal of Materials Science, 2021. **56**: p. 1-11.
135. Bahgat, M., et al., *Efficiency, Kinetics and Thermodynamics of Toluidine Blue Dye Removal from Aqueous Solution Using MWCNTs Decorated with NiFe2O4.* Fullerenes, 2014. **22**.
136. Xiao, C., et al., *Improved thermal properties by controlling selective distribution of AlN and MWCNT in immiscible polycarbonate (PC)/Polyamide 66 (PA66) composites.* Composites Part A: Applied Science and Manufacturing, 2018. **110**: p. 133-141.
137. Liu, W., et al., *Insight into pH dependent Cr(VI) removal with magnetic Fe3S4.* Chemical Engineering Journal, 2019. **359**: p. 564-571.

138. Manning, B.A., et al., *Spectroscopic investigation of Cr (III)-and Cr (VI)-treated nanoscale zerovalent iron.* Environmental science & technology, 2007. **41**(2): p. 586-592.
139. Zhu, F., et al., *Effect factors, kinetics and thermodynamics of remediation in the chromium contaminated soils by nanoscale zero valent Fe/Cu bimetallic particles.* Chemical Engineering Journal, 2016. **302**: p. 663-669.
140. Liu, X., et al., *Graphene oxide-based materials for efficient removal of heavy metal ions from aqueous solution: A review.* Environmental Pollution, 2019. **252**: p. 62-73.
141. Latif, A., et al., *Remediation of heavy metals polluted environment using Fe-based nanoparticles: Mechanisms, influencing factors, and environmental implications.* Environmental Pollution, 2020. **264**: p. 114728.
142. Penner, M.H., *Basic principles of spectroscopy*, in *Food analysis*. 2017, Springer. p. 79-88.
143. Atkins, P., P.W. Atkins, and J. de Paula, *Atkins' physical chemistry*. 2014: Oxford university press.
144. Rai, D., B.M. Sass, and D.A. Moore, *Chromium(III) hydrolysis constants and solubility of chromium(III) hydroxide.* Inorganic Chemistry, 1987. **26**(3): p. 345-349.
145. Stefánsson, A., *Iron(III) Hydrolysis and Solubility at 25 °C.* Environmental Science & Technology, 2007. **41**(17): p. 6117-6123.
146. Jia, X. and R.A. Williams, *A Hybrid Mesoscale Modelling Approach to Dissolution of Granules and Tablets.* Chemical Engineering Research and Design, 2007. **85**(7): p. 1027-1038.
147. Cao, H., et al., *CFD-DNS simulation of irregular-shaped particle dissolution.* Particuology, 2020. **50**: p. 144-155.
148. Yuan, Q., X. Jia, and R.A. Williams, *Validation of a multi-component digital dissolution model for irregular particles.* Powder Technology, 2013. **240**: p. 25-30.
149. Dolomite Microfluidics. 2022. Micromixer Chip. [online] Available at: <https://www.dolomite-microfluidics.com/product/micromixer-chip/> [Accessed 1 August 2022].

Appendix A

Micromixer structure and working mechanism

The micromixer chip has two designs bonded onto each wafer. One is a set of mixing stages, and the other provides a fluidic pathway for liquid to pass into and out of the mixing stages [149]. The structure is shown below:

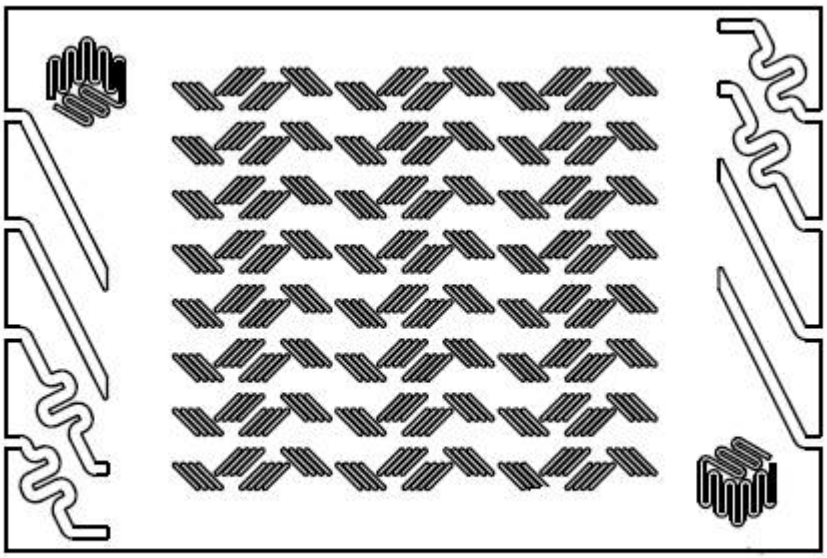

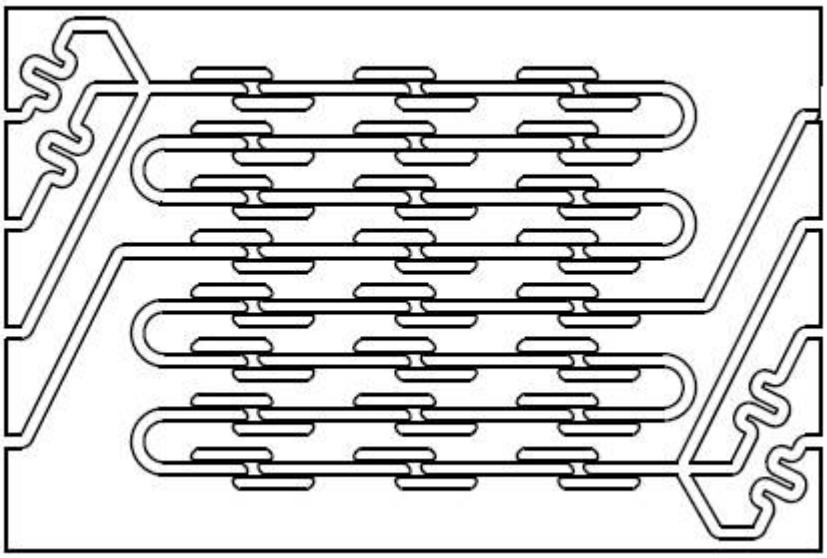

The primary means for mixing in this chip is therefore disrupting the laminar into controlled mixing stages by physically forcing liquids to mix.

During the mixing stage, part of the liquid flows from the main tube 1 to the main tube 2 through the small conduit. The remaining liquid continues to flow in the main tube 1, repeating the previous split when it meets the next small conduit.

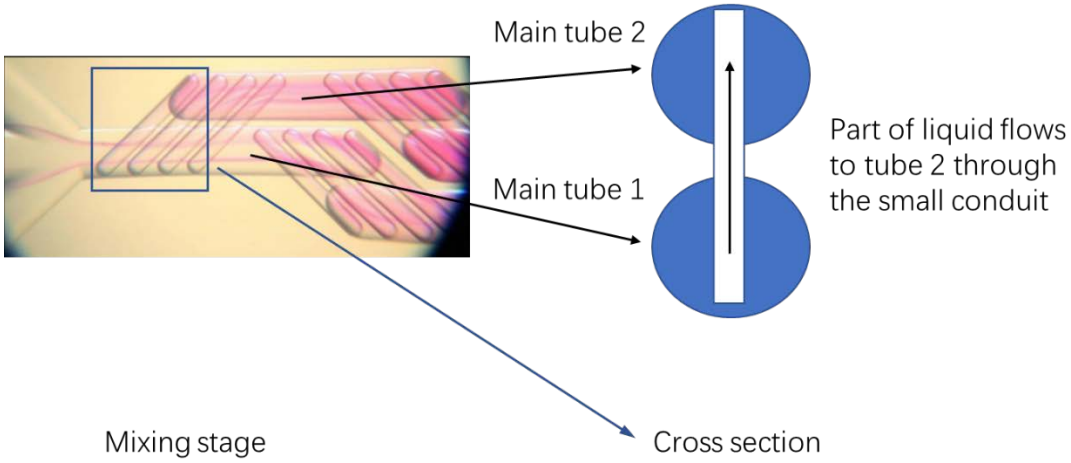

The micromixer chip is a static mixer (no moving parts), which at low flow rates creates lamination of the flow streams as shown in the diagram below:

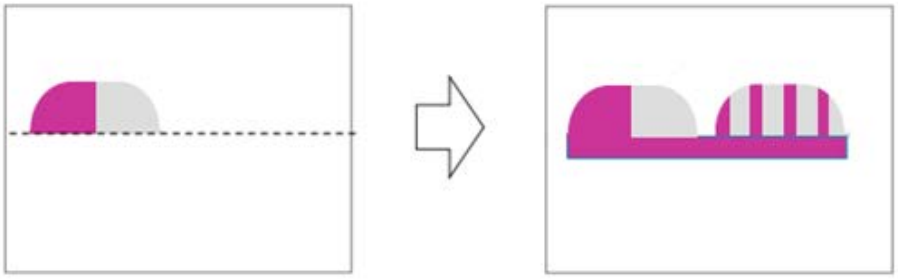

The mixing stage disrupts the streams laminar and reduces diffusion distances and hence improves mixing time. At high flow rates swirling occurs in the flow streams, reducing mixing time further.